Dark Energy Survey Year 3 results: Cosmology from cosmic shear and robustness to modeling uncertainty

L. F. Secco,[1,2,*] S. Samuroff,[3,4,†] E. Krause,[5] B. Jain,[2] J. Blazek,[4,6] M. Raveri,[2] A. Campos,[3] A. Amon,[7] A. Chen,[8] C. Doux,[2] A. Choi,[9,10] D. Gruen,[7,11,12] G. M. Bernstein,[2] C. Chang,[1] J. DeRose,[13] J. Myles,[7,11,12] A. Ferté,[14] P. Lemos,[15] D. Huterer,[8] J. Prat,[1] M. A. Troxel,[16] N. MacCrann,[17] A. R. Liddle,[18,19,20] T. Kacprzak,[21] X. Fang,[5] C. Sánchez,[2] S. Pandey,[2] S. Dodelson,[3] P. Chintalapati,[22] K. Hoffmann,[23] A. Alarcon,[24] O. Alves,[25] F. Andrade-Oliveira,[25,26] E. J. Baxter,[27] K. Bechtol,[28] M. R. Becker,[24] A. Brandao-Souza,[29,30] H. Camacho,[25,26] A. Carnero Rosell,[31,32,33] M. Carrasco Kind,[34,35] R. Cawthon,[28] J. P. Cordero,[36] M. Crocce,[37,38] C. Davis,[7] E. Di Valentino,[36] A. Drlica-Wagner,[39,40,1] K. Eckert,[2] T. F. Eifler,[5,14] M. Elidaiana,[8] F. Elsner,[41] J. Elvin-Poole,[9,10] S. Everett,[42] P. Fosalba,[37,38] O. Friedrich,[43] M. Gatti,[2] G. Giannini,[44] R. A. Gruendl,[34,35] I. Harrison,[45,36] W. G. Hartley,[46] K. Herner,[40] H. Huang,[5] E. M. Huff,[14] M. Jarvis,[2] N. Jeffrey,[47,48] N. Kuropatkin,[40] P.-F. Leget,[49,50,51] J. Muir,[7] J. Mccullough,[7,11,12] A. Navarro Alsina,[52,26] Y. Omori,[39,1,7] Y. Park,[53] A. Porredon,[9,10] R. Rollins,[36] A. Roodman,[7,12] R. Rosenfeld,[54,26] A. J. Ross,[55] E. S. Rykoff,[7,12] J. Sanchez,[40] I. Sevilla-Noarbe,[31] E. S. Sheldon,[56] T. Shin,[2] A. Troja,[54,26] I. Tutusaus,[38] T. N. Varga,[41,57] N. Weaverdyck,[8] R. H. Wechsler,[11,7,12] B. Yanny,[58] B. Yin,[3] Y. Zhang,[40] J. Zuntz,[59] T. M. C. Abbott,[60] M. Aguena,[30] S. Allam,[40] J. Annis,[40] D. Bacon,[61] E. Bertin,[62,63] S. Bhargava,[64] S. L. Bridle,[36] D. Brooks,[47] E. Buckley-Geer,[39,40] D. L. Burke,[7,12] J. Carretero,[65] M. Costanzi,[66,67,68] L. N. da Costa,[30,69] J. De Vicente,[70] H. T. Diehl,[40] J. P. Dietrich,[71] P. Doel,[47] I. Ferrero,[72] B. Flaugher,[40] J. Frieman,[40,1] J. García-Bellido,[73] E. Gaztanaga,[37,38] D. W. Gerdes,[74,8] T. Giannantonio,[43,75] J. Gschwend,[30,69] G. Gutierrez,[40] S. R. Hinton,[76] D. L. Hollowood,[42] K. Honscheid,[9,10] B. Hoyle,[71,77] D. J. James,[78] T. Jeltema,[42] K. Kuehn,[79,80] O. Lahav,[47] M. Lima,[81,30] H. Lin,[40] M. A. G. Maia,[30,69] J. L. Marshall,[82] P. Martini,[9,83,84] P. Melchior,[85] F. Menanteau,[86,34] R. Miquel,[87,65] J. J. Mohr,[71,77] R. Morgan,[28] R. L. C. Ogando,[30,69] A. Palmese,[40,1] F. Paz-Chinchón,[86,43] D. Petravick,[86] A. Pieres,[30,69] A. A. Plazas Malagón,[85] M. Rodriguez-Monroy,[70] A. K. Romer,[64] E. Sanchez,[70] V. Scarpine,[40] M. Schubnell,[8] D. Scolnic,[16] S. Serrano,[37,38] M. Smith,[88] M. Soares-Santos,[8] E. Suchyta,[89] M. E. C. Swanson,[86] G. Tarle,[8] D. Thomas,[61] and C. To[11,7,12]

(DES Collaboration)

[1]*Kavli Institute for Cosmological Physics, University of Chicago, Chicago, Illinois 60637, USA*
[2]*Department of Physics and Astronomy, University of Pennsylvania,*
Philadelphia, Pennsylvania 19104, USA
[3]*McWilliams Center for Cosmology, Department of Physics, Carnegie Mellon University,*
Pittsburgh, Pennsylvania 15213, USA
[4]*Department of Physics, Northeastern University, Boston, Massachusetts 02115, USA*
[5]*Department of Astronomy/Steward Observatory, University of Arizona,*
933 North Cherry Avenue, Tucson, Arizona 85721-0065, USA
[6]*Laboratory of Astrophysics, École Polytechnique Fédérale de Lausanne (EPFL),*
1290 Versoix, Switzerland
[7]*Kavli Institute for Particle Astrophysics and Cosmology, P. O. Box 2450, Stanford University,*
Stanford, California 94305, USA
[8]*Department of Physics, University of Michigan, Ann Arbor, Michigan 48109, USA*
[9]*Center for Cosmology and Astro-Particle Physics, The Ohio State University,*
Columbus, Ohio 43210, USA
[10]*Department of Physics, The Ohio State University, Columbus, Ohio 43210, USA*
[11]*Department of Physics, Stanford University, 382 Via Pueblo Mall, Stanford, California 94305, USA*
[12]*SLAC National Accelerator Laboratory, Menlo Park, California 94025, USA*
[13]*Berkeley Center for Cosmological Physics, University of California, Berkeley, California 94720, USA*
[14]*Jet Propulsion Laboratory, California Institute of Technology,*
4800 Oak Grove Dr., Pasadena, California 91109, USA
[15]*Department of Physics and Astronomy, University College London,*
Gower Street, London WC1E 6BT, United Kingdom
[16]*Department of Physics, Duke University Durham, North Carolina 27708, USA*
[17]*Department of Applied Mathematics and Theoretical Physics, University of Cambridge,*
Cambridge CB3 0WA, United Kingdom
[18]*Instituto de Astrofísica e Ciências do Espaço, Faculdade de Ciências, Universidade de Lisboa,*
1769-016 Lisboa, Portugal

[19]*Institute for Astronomy, University of Edinburgh, Edinburgh EH9 3HJ, United Kingdom*
[20]*Perimeter Institute for Theoretical Physics,*
31 Caroline Street North, Waterloo, Ontario N2L 2Y5, Canada
[21]*Institute for Particle Physics and Astrophysics, ETH Zürich,*
Wolfgang-Pauli-Strasse 27, CH-8093 Zürich, Switzerland
[22]*Department of Physics, Northern Illinois University, DeKalb, Illinois 60115, USA*
[23]*Institute for Computational Science, University of Zürich,*
Winterthurerstr. 190, 8057 Zürich, Switzerland
[24]*Argonne National Laboratory, 9700 South Cass Avenue, Lemont, Illinois 60439, USA*
[25]*Instituto de Física Teórica, Universidade Estadual Paulista, São Paulo 01140-070, Brazil*
[26]*Laboratório Interinstitucional de e-Astronomia—LIneA,*
Rua Gal. José Cristino 77, Rio de Janeiro, RJ—20921-400, Brazil
[27]*Institute for Astronomy, University of Hawai'i, 2680 Woodlawn Drive, Honolulu, Hawaii 96822, USA*
[28]*Physics Department, 2320 Chamberlin Hall, University of Wisconsin-Madison,*
1150 University Avenue Madison, Wisconsin 53706-1390, USA
[29]*Instituto de Física Gleb Wataghin, Universidade Estadual de Campinas,*
Campinas, 13083-859 São Paulo, Brazil
[30]*Laboratório Interinstitucional de e-Astronomia—LIneA,*
Rua Gal. José Cristino 77, Rio de Janeiro RJ—20921-400, Brazil
[31]*Centro de Investigaciones Energéticas, Medioambientales y Tecnológicas (CIEMAT),*
E-28040 Madrid, Spain
[32]*Instituto de Astrofísica de Canarias, E-38205 La Laguna, Tenerife, Spain*
[33]*Universidad de La Laguna, Dpto. Astrofísica, E-38206 La Laguna, Tenerife, Spain*
[34]*Department of Astronomy, University of Illinois at Urbana-Champaign,*
1002 W. Green Street, Urbana, Illinois 61801, USA
[35]*National Center for Supercomputing Applications, 1205 West Clark Street, Urbana, Illinois 61801, USA*
[36]*Jodrell Bank Centre for Astrophysics, School of Physics and Astronomy, University of Manchester,*
Oxford Road, Manchester M13 9PL, United Kingdom
[37]*Institut d'Estudis Espacials de Catalunya (IEEC), 08034 Barcelona, Spain*
[38]*Institute of Space Sciences (ICE, CSIC), Campus UAB, Carrer de Can Magrans,*
s/n, 08193 Barcelona, Spain
[39]*Department of Astronomy and Astrophysics, University of Chicago, Chicago, Illinois 60637, USA*
[40]*Fermi National Accelerator Laboratory, P. O. Box 500, Batavia, Illinois 60510, USA*
[41]*Max Planck Institute für Extraterrestrial Physics, Giessenbachstrasse, 85748 Garching, Germany*
[42]*Santa Cruz Institute for Particle Physics, Santa Cruz, California 95064, USA*
[43]*Institute of Astronomy, University of Cambridge, Madingley Road,*
Cambridge CB3 0HA, United Kingdom
[44]*Institut de Física d'Altes Energies (IFAE), The Barcelona Institute of Science and Technology,*
Campus UAB, 08193 Bellaterra (Barcelona), Spain
[45]*Department of Physics, University of Oxford, Denys Wilkinson Building,*
Keble Road, Oxford OX1 3RH, United Kingdom
[46]*Département de Physique Théorique and Center for Astroparticle Physics, Université de Genève,*
24 quai Ernest Ansermet, CH-1211 Geneva, Switzerland
[47]*Department of Physics and Astronomy, University College London,*
Gower Street, London WC1E 6BT, United Kingdom
[48]*Laboratoire de Physique de l'Ecole Normale Supérieure, ENS, Université PSL,*
CNRS, Sorbonne Université, Université de Paris, Paris 75006, France
[49]*Université Clermont Auvergne, CNRS/IN2P3, Laboratoire de Physique de Clermont,*
F-63000 Clermont-Ferrand, France
[50]*Kavli Institute for Particle Astrophysics and Cosmology, Department of Physics, Stanford University,*
Stanford, California 94305, USA
[51]*LPNHE, CNRS/IN2P3, Sorbonne Université, Paris Diderot,*
Laboratoire de Physique Nucléaire et de Hautes Énergies, F-75005 Paris, France
[52]*Instituto de Física Gleb Wataghin, Universidade Estadual de Campinas,*
Campinas, 13083-859 São Paulo, Brazil
[53]*Kavli Institute for the Physics and Mathematics of the Universe (WPI), UTIAS,*
The University of Tokyo, Kashiwa, Chiba 277-8583, Japan
[54]*ICTP South American Institute for Fundamental Research Instituto de Física Teórica,*
Universidade Estadual Paulista, São Paulo 01140-070, Brazil
[55]*Center for Cosmology and Astro-Particle Physics, Ohio State University, Columbus, Ohio 43210, USA*

[56]*Brookhaven National Laboratory, Bldg 510, Upton, New York 11973, USA*

[57]*Universitäts-Sternwarte, Fakultät für Physik, Ludwig-Maximilians Universität München,*
Scheinerstrasse 1, 81679 München, Germany

[58]*Fermi National Accelerator Laboratory, P. O. Box 500, Batavia, Illinois 60510, USA*

[59]*Institute for Astronomy, University of Edinburgh, Blackford Hill, Edinburgh EH9 3HJ, United Kingdom*

[60]*Cerro Tololo Inter-American Observatory, NSF's National Optical-Infrared Astronomy Research*
Laboratory, Casilla 603, La Serena, Chile

[61]*Institute of Cosmology and Gravitation, University of Portsmouth,*
Portsmouth PO1 3FX, United Kingdom

[62]*CNRS, UMR 7095, Institut d'Astrophysique de Paris, F-75014 Paris, France*

[63]*Sorbonne Universités, UPMC Univ Paris 06, UMR 7095, Institut d'Astrophysique de Paris,*
F-75014 Paris, France

[64]*Department of Physics and Astronomy, Pevensey Building, University of Sussex,*
Brighton BN1 9QH, United Kingdom

[65]*Institut de Física d'Altes Energies (IFAE), The Barcelona Institute of Science and Technology,*
Campus UAB, 08193 Bellaterra (Barcelona), Spain

[66]*Astronomy Unit, Department of Physics, University of Trieste, via Tiepolo 11, I-34131 Trieste, Italy*

[67]*INAF-Osservatorio Astronomico di Trieste, via G. B. Tiepolo 11, I-34143 Trieste, Italy*

[68]*Institute for Fundamental Physics of the Universe, Via Beirut 2, 34014 Trieste, Italy*

[69]*Observatório Nacional, Rua Gal. José Cristino 77, Rio de Janeiro RJ—20921-400, Brazil*

[70]*Centro de Investigaciones Energéticas, Medioambientales y Tecnológicas (CIEMAT),*
Madrid 28040, Spain

[71]*Faculty of Physics, Ludwig-Maximilians-Universität, Scheinerstrasse 1, 81679 Munich, Germany*

[72]*Institute of Theoretical Astrophysics, University of Oslo.*
P.O. Box 1029 Blindern, NO-0315 Oslo, Norway

[73]*Instituto de Fisica Teorica UAM/CSIC, Universidad Autonoma de Madrid, 28049 Madrid, Spain*

[74]*Department of Astronomy, University of Michigan, Ann Arbor, Michigan 48109, USA*

[75]*Kavli Institute for Cosmology, University of Cambridge, Madingley Road,*
Cambridge CB3 0HA, United Kingdom

[76]*School of Mathematics and Physics, University of Queensland, Brisbane, Queensland 4072, Australia*

[77]*Max Planck Institute for Extraterrestrial Physics, Giessenbachstrasse, 85748 Garching, Germany*

[78]*Center for Astrophysics | Harvard & Smithsonian, 60 Garden Street,*
Cambridge, Massachusetts 02138, USA

[79]*Australian Astronomical Optics, Macquarie University, North Ryde NSW 2113, Australia*

[80]*Lowell Observatory, 1400 Mars Hill Rd, Flagstaff, Arizona 86001, USA*

[81]*Departamento de Física Matemática, Instituto de Física, Universidade de São Paulo,*
CP 66318, São Paulo, SP 05314-970, Brazil

[82]*George P. and Cynthia Woods Mitchell Institute for Fundamental Physics and Astronomy, and*
Department of Physics and Astronomy, Texas A&M University, College Station, Texas 77843, USA

[83]*Department of Astronomy, The Ohio State University, Columbus, Ohio 43210, USA*

[84]*Radcliffe Institute for Advanced Study, Harvard University, Cambridge, Massachusetts 02138, USA*

[85]*Department of Astrophysical Sciences, Princeton University, Peyton Hall,*
Princeton, New Jersey 08544, USA

[86]*Center for Astrophysical Surveys, National Center for Supercomputing Applications,*
1205 West Clark Street, Urbana, Illinois 61801, USA

[87]*Institució Catalana de Recerca i Estudis Avançats, E-08010 Barcelona, Spain*

[88]*School of Physics and Astronomy, University of Southampton, Southampton SO17 1BJ, United Kingdom*

[89]*Computer Science and Mathematics Division, Oak Ridge National Laboratory,*
Oak Ridge, Tennessee 37831, USA

This work and its companion paper, Amon *et al.* [Phys. Rev. D **105,** 023514 (2022)], present cosmic shear measurements and cosmological constraints from over 100 million source galaxies in the Dark Energy Survey (DES) Year 3 data. We constrain the lensing amplitude parameter $S_8 \equiv \sigma_8 \sqrt{\Omega_{\rm m}/0.3}$ at the 3% level in ΛCDM: $S_8 = 0.759^{+0.025}_{-0.023}$ (68% CL). Our constraint is at the 2% level when using angular scale cuts that are optimized for the ΛCDM analysis: $S_8 = 0.772^{+0.018}_{-0.017}$ (68% CL). With cosmic shear alone, we

[*]secco@uchicago.edu
[†]s.samuroff@northeastern.edu

find no statistically significant constraint on the dark energy equation-of-state parameter at our present statistical power. We carry out our analysis blind, and compare our measurement with constraints from two other contemporary weak lensing experiments: the Kilo-Degree Survey (KiDS) and Hyper-Suprime Camera Subaru Strategic Program (HSC). We additionally quantify the agreement between our data and external constraints from the Cosmic Microwave Background (CMB). Our DES Y3 result under the assumption of ΛCDM is found to be in statistical agreement with Planck 2018, although favors a lower S_8 than the CMB-inferred value by 2.3σ (a p-value of 0.02). This paper explores the robustness of these cosmic shear results to modeling of intrinsic alignments, the matter power spectrum and baryonic physics. We additionally explore the statistical preference of our data for intrinsic alignment models of different complexity. The fiducial cosmic shear model is tested using synthetic data, and we report no biases greater than 0.3σ in the plane of $S_8 \times \Omega_{\rm m}$ caused by uncertainties in the theoretical models.

I. INTRODUCTION

Discoveries and advances in modern cosmology have resulted in a remarkably simple standard cosmological model, known as ΛCDM. The model is specified by a spatially flat universe, governed by the general theory of relativity, which contains baryonic matter, dark matter, and a dark energy component that causes the expansion of the Universe to accelerate. Although remarkably simple, it appears to be sufficient to describe a great many observations, including the stability of cold disk galaxies, flat galaxy rotation curves, observations of strong gravitational lensing in clusters, the acceleration of the expansion of the Universe as inferred by type Ia supernovae (SNe Ia), and the pattern of temperature fluctuations in the cosmic microwave background (CMB). Yet despite all this, ΛCDM is fundamentally mysterious in the sense that the physical nature of its two main components, dark matter and dark energy, is still completely unknown.

The success of ΛCDM has, however, been shaken in recent years by new experimental results. We have seen tentative hints that the model might fail to simultaneously describe the late- (low redshift) and early-time (high redshift) Universe. To take one prominent example, constraints on the local expansion parameter H_0 obtained from the local distance ladder and SNe Ia appear to be in tension with those inferred by the CMB [1] at a statistically significant level [2], with varying levels of significance being reported by different probes [3,4]. In a separate but analogous tension, the value of the $S_8 \equiv \sigma_8 (\Omega_{\rm m}/0.3)^{1/2}$ parameter—the amplitude of mass fluctuations σ_8 scaled by the square root of matter density $\Omega_{\rm m}$—differs when inferred via cosmological lensing [5–7] from the value obtained using Planck (assuming ΛCDM; [1]) at the level of 2–3σ. Other probes of the late Universe, in particular spectroscopic galaxy clustering [8], redshift-space distortions [3] and the abundance of galaxy clusters [9,10], also all tend to prefer relatively low values of S_8. Although the evidence is by no means definitive, we are perhaps beginning to see hints of new physics, and so

stress-testing ΛCDM with new measurements is extremely important.

Cosmic shear, or cosmological weak lensing (the two-point correlation function of gravitational shear), is one of the most informative of the low redshift probes. It has two main advantages, as a means to infer the properties of the large scale Universe [11–14]. First, the signal is insensitive to galaxy bias, which is a significant source of uncertainty in cosmological analyses based on galaxy clustering and galaxy-galaxy lensing. Second, weak lensing is sensitive both to the *geometry* of the Universe through the lensing kernel (which is a function of H_0 and ratios of angular diameter distances), and also to the *growth of structure* and its evolution in redshift. Since geometry and structure growth are tightly related to the evolution of dark energy and its equation-of-state parameter w, this sensitivity carries over to the cosmic shear signal.

Cosmic shear was first measured over twenty years ago, roughly simultaneously by a number of groups [15–18]. Although too noisy to constrain cosmological parameters, these observations represented the first steps toward fulfilling the potential pointed out by theoretical studies years earlier [19–21]. The intervening two decades have seen steady improvements in signal-to-noise and cosmological constraining power, as new ground- and space-based lensing datasets have become available [5,6,22–47]. As the volume and quality of lensing data have improved, so too have the methods used to study it, with the development of an array of sophisticated statistical and theoretical tools. There has, for example, been a coherent effort to test and improve shape measurement algorithms using increasingly complex image simulations [48–52]. Methods for estimating the distribution of source galaxies along the line of sight have also gradually evolved to become highly sophisticated, incorporating various sources of information [53–58].

Alongside the Dark Energy Survey (DES),[1] the major lensing surveys of the current generation are the

---

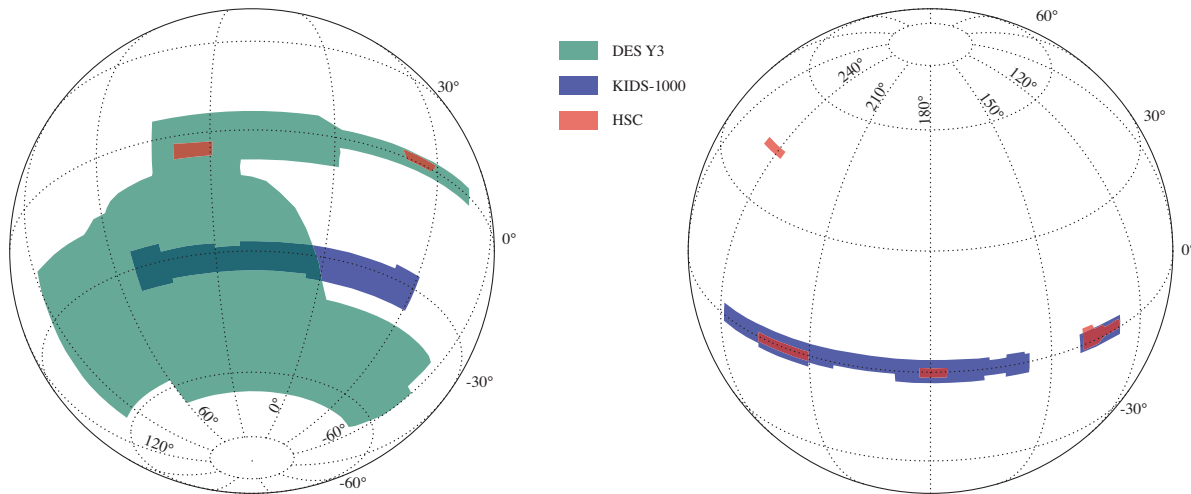[1]https://www.darkenergysurvey.org/.

FIG. 1.   The approximate footprints of Stage-III dark energy experiments: Dark Energy Survey Year 3 (DES Y3; green), Kilo-Degree Survey (KiDS-1000; blue), and first-year Hyper Suprime-Cam Subaru Strategic Program (HSC; red). The left and right panels show orthographic projections of the northern and southern sky respectively. The parallels and meridians show declination and right ascension. The different survey areas not only affect the final analysis choices, but also reflect the individual science strategies and the complementarity of Stage-III surveys.

Kilo-Degree Survey (KiDS; de Jong *et al.* [59])[2] and the Hyper-Suprime Camera Subaru Strategic Program (HSC; Aihara *et al.* [60]).[3] We show the approximate, nominal footprints of these surveys in Fig. 1. Each of these three collaborations have, in recent years, released cosmic shear analyses analogous to the one presented in this paper. Lensing analyses based on HSC data were carried out over a footprint of 136.9 deg^2 split into six fields (red patches in Fig. 1; [61]); they presented consistent cosmology results using two types of statistics: real space correlation functions [28] and harmonic space power spectra [6]. More recently, the KiDS collaboration released results based on approximately 1000 deg^2 of data (blue patches in Fig. 1; [62]), and presented an analysis of band-power spectra, correlation functions and the complete orthogonal sets of E-/B-mode integrals (COSEBIs [5]). They further combined their cosmic shear results with external spectroscopic data from BOSS [63] to obtain a 3×2pt constraint [64], which is internally consistent with their cosmic shear results, but differs from Planck in the full parameter space by $\sim 2\sigma$.

The trend observed in earlier cosmic shear studies is that the amplitude of the cosmic shear signal (tied to the amplitude of matter fluctuations through the S_8 parameter) is lower than that extrapolated from the CMB. In order to demonstrate whether this discrepancy is physical and significant, we must have a high degree of confidence in our modeling of the data and its possible systematic errors. Among the most significant of these sources of systematic error are intrinsic alignments (IAs), or astrophysically sourced correlations of galaxy shapes, which mimic cosmic

shear. Given how difficult it is to disentangle IAs from lensing, the most common approach is to forward-model their effect, assuming a model for the IA power spectrum with a number of free parameters. Depending on the galaxy sample, however, IA model insufficiency can easily translate into a bias in cosmological parameters [65,66]. In addition to IAs, effects such as nonlinear growth and the impact of baryons on the large-scale distribution of dark matter can alter the matter power spectrum in a significant way, and so bias the inferred lensing amplitude if neglected [67–71]. Although it is clear that these effects are scale-dependent, finding the angular scales where our modeling is sufficient is by no means straightforward. This paper describes the choices made in modeling and scale cuts, and validates that the potential biases on cosmological parameters are smaller than the statistical uncertainties.

Our companion paper [72] presents a detailed investigation of observational errors that can similarly bias cosmological inference. Undiagnosed biases in the shear measurement process, for example, can lead one to incorrectly infer the lensing amplitude. Likewise, errors in the estimation of galaxy redshift distributions $n(z)$ can subtly alter the interpretation of the lensing measurement, both in terms of cosmology and of IAs. Amon *et al.* [72] demonstrate that these measurement systematic errors are well controlled in the Y3 cosmic shear analysis. *We note that the main cosmological constraints presented in both papers are identical.*

The cosmic shear analysis presented in this paper, and in Amon *et al.* [72], is part of a series of Year 3 cosmological results from large-scale structure produced by the Dark Energy Survey Collaboration. This work relies on many companion papers that validate the data, catalogs and

---

[2]http://kids.strw.leidenuniv.nl/DR4/index.php.
[3]https://www.naoj.org/Projects/HSC.

theoretical methods; those papers, as well as this one, feed into the main "3 × 2pt" constraints, which combine cosmic shear with galaxy-galaxy lensing and galaxy clustering in ΛCDM and *w*CDM [73], as well as extended cosmological parameter spaces [74]. These include:

(i) The construction and validation of the Gold catalog of objects in DES Y3 is described in Sevilla-Noarbe *et al.* [75].

(ii) The Point-Spread Function (PSF) modeling algorithm and its validation tests are described in Jarvis *et al.* [76].

(iii) A suite of image simulations, used to test the shape measurement pipeline and ultimately determine the shear calibration uncertainties is described in Mac-Crann *et al.* [77].

(iv) The METACALIBRATION shape catalog, and the tests that validate its science-readiness, are described in Gatti *et al.* [78]. This paper also discusses the (first layer) catalog-level blinding implemented in Y3.

(v) The characterization of the source redshift distribution, and the related systematic and statistical uncertainties, are detailed in five papers. Namely, Myles *et al.* [79] and Buchs *et al.* [55] present the baseline methodology for estimating wide-field redshift distributions using Self-Organizing Maps; Gatti *et al.* [80] outline an alternative method using cross correlations with spectroscopic galaxies; Sánchez *et al.* [81] presents a complementary likelihood using small scale galaxy-galaxy lensing, improving constraints on redshifts and IA; finally Cordero *et al.* [82] validates our fiducial error parametrization using a more complete alternative based on distribution realizations. In addition to this, Hartley *et al.* [83] and Everett *et al.* [84] respectively describe the DES deep fields and the Balrog image simulations, both of which are crucial in testing and implementing the Y3 redshift methodology.

(vi) The data covariance matrix is described in Friedrich *et al.* [85]. This paper also presents various validation tests based on DES Y3 simulations, and demonstrates its suitability for likelihood analyses.

(vii) The numerical metrics used to assess tension between our DES results and external datasets are described in Lemos *et al.* [86]. That work considers a number of alternatives, and sets out the methodology used in this paper and Dark Energy Survey Collaboration [73].

(viii) The simultaneous blinding of the multiple DES Y3 probes at the two-point correlation function level is described in Muir *et al.* [87];

(ix) DeRose *et al.* [88] presents a set of cosmological simulations which are used as an end-to-end validation of our analysis framework on mock *N*-body data.

(x) Finally, tests of the theoretical and numerical methods, as well as modeling assumptions for all 3 × 2pt analyses are described in Krause *et al.* [89].

This paper is organized as follows: Sec. II describes the DES Y3 data, and the catalog construction and calibration. Section III describes the two-point measurements upon which our results are based, as well as the covariance estimation and blinding scheme. In Sec. IV, we describe the theoretical modeling of the cosmic shear two-point data vector. We demonstrate our model is robust to various forms of systematic error, using simulated data, in Sec. V. Our baseline results and an exploration of the IA model complexity present in our data are then presented in Sec. VI. In Sec. VII we present a series of reanalyses, using slightly different modeling choices, in order to verify the robustness of our findings. The consistency of DES Y3 cosmic shear data with external probes such as other weak lensing surveys and the CMB is examined in Sec. VIII. Finally, Sec. IX summarizes our findings and discusses their significance in the context of the field.

II. DES Y3 DATA AND SAMPLE SELECTION

This section briefly describes the DES Y3 data, and defines the galaxy samples used in this paper. We also discuss a number of related topics, including calibrating selection biases.

A. Data collection and the Gold selection

DES has now completed its six-year campaign, covering a footprint of around 5000 deg^2 to a depth of $r \sim 24.4$. The DES data were collected using the 570 megapixel Dark Energy Camera (DECam; Flaugher *et al.* [90]), at the Blanco telescope at the Cerro Tololo Inter-American Observatory (CTIO), Chile, using five photometric filters $grizY$, which cover a region of the optical and near infrared spectrum between 0.40 and 1.06 μm. DES SV, Y1 and Y3 cover sequentially larger fractions of the full Y6 footprint, with Y3, the dataset used in this analysis, encompassing 4143 deg^2 after masking, with the "Wide Survey" footprint covered with 4 overlapping images in each band (compared with the final survey depth of ∼8). The images undergo a series of reduction and pre-processing steps, including background subtraction [91–93], and masking out cosmic rays, satellite trails and bright stars. Object detection is performed on the riz coadd images using source extractor [94]. For the detected galaxies, derived photometric measurements are generated using multiobject fitting (MOF; [95]) to mitigate blending. The final Y3 selection with baseline masking is referred to as the Gold catalog, and is described in detail in Sevilla-Noarbe *et al.* [75].

B. Shape catalog and image simulations

The DES Y3 shape catalog is created using the METACALIBRATION algorithm [96,97]. The basic shape

measurement entails fitting a single elliptical Gaussian to each detected galaxy. The fit is repeated on artificially sheared copies of the given galaxy, in order to construct a shear response matrix R_γ via a numerical derivative; a selection response R_S is also computed in a similar way. These multiplicative responses are the essence of METACALIBRATION. After quality cuts, the Y3 METACALIBRATION catalog contains over 100 million galaxies, with a mean redshift of $z = 0.63$ and a weighted number density[4] $n_{\text{eff}} = 5.59$ arcmin^{-2}; for discussion of the cuts and why they are necessary, see Gatti et al. [78].

Although METACALIBRATION greatly reduces the biases inherent to shear estimation, the process is not perfect. We must still rely on image simulations for validation and for deriving priors on the residual biases (predominantly due to blending, and its impact on the redshift distribution). These simulations, and the conclusions we draw from them for Y3, are discussed in MacCrann et al. [77]. In addition to tests using simulations, the catalogs are subject to a number of null tests, applied directly to the data. Using both pseudo-C_ℓs and COSEBIs [100], we find no evidence for nonzero B-modes in Y3.

C. Photometric redshift calibration

We estimate and calibrate the redshift distributions of our source sample with a combination of three different methods. Our base methodology is known as *Self-Organizing Map $p(z)$* (SOMPZ; [79]). The most important aspect of this methodology is that knowledge from precise redshifts (from spectroscopic samples) and higher-quality photometric data (from DES deep fields [83]) informs the bulk of the DES observations (the wide fields), essentially acting as a Bayesian prior. The connection between the deep and wide field data is determined empirically using an image simulation framework known as Balrog [84].

Additionally, clustering redshifts (WZ; [80]) employ cross-correlations of galaxy densities to improve redshift constraints, and shear ratios [81] help to constrain redshifts (and also intrinsic alignment parameters), utilizing galaxy-shear correlation functions at small scales. While SOMPZ and WZ are applied upstream to generate and select $n(z)$ estimates, the shear-ratio information, on the other hand, is incorporated at the point of evaluation of cosmological likelihoods (see Sec. IV F). Details of each of these methods in the context of Y3 can be found in Myles et al. [79], and robustness tests of redshift distributions in the context of cosmic shear are presented in Amon et al. [72].

---

[4]The effective number density here is as defined by Heymans et al. [98]. The equivalent value using Chang et al. [99]'s definition is 5.32 arcmin^{-2} (see [78] for details.)

III. COSMIC SHEAR MEASUREMENT

In this section we present the measured real-space cosmic shear two-point correlations [$\xi_\pm(\theta)$, see Eq. (11)], which form the basis of our results and are shown in Fig. 2. Defining the signal-to-noise of our measurement as

$$\text{S/N} \equiv \frac{\xi_\pm^{\text{data}}(\theta)^T \mathbf{C}^{-1} \xi_\pm^{\text{model}}(\theta)}{\sqrt{\xi_\pm^{\text{model}}(\theta)^T \mathbf{C}^{-1} \xi_\pm^{\text{model}}(\theta)}}, \quad (1)$$

where $\mathbf{C}$ is the data covariance matrix, the S/N of the cosmic shear detection in DES Y3 after scale cuts is 27. For the fiducial ΛCDM model, our chi-square at the maximum posterior is $\chi^2 = 237.7$, with 222 effective degrees-of-freedom (d.o.f.), which gives us a p—value of 0.22 (see Sec. VI A). We define these quantities in more detail in Sec. IV.

A. Tomography

We define a set of four broad redshift bins for our source sample in the nominal range $0 < z < 3$, with actual number densities being fairly small above $z \gtrsim 1.5$. These are constructed by iteratively adjusting the redshift bin edges, such that they each yield approximately the same number of source galaxies. The Y3 SOMPZ methodology (see Sec. II C) makes use of Balrog, which artificially inserts COSMOS galaxies into DES images. The artificial galaxies are assigned to cells in both the wide- and deep-field self-organizing maps (SOMs), which allows one to map between the two, and so assign DES wide-field galaxies to bins (see [79], Sec. IV C).

The redshift distributions computed in this way, which feed into our modeling in the next section, are shown in Fig. 3. The galaxy number densities are 1.476, 1.479, 1.484, and 1.461 per square arcminute respectively in these four redshift bins.

B. Two-point estimator and measurement

The spin-2 shear field can be expressed in terms of a real and an imaginary component, $\gamma = \gamma_1 + i\gamma_2$. There are two possible shear two-point functions that preserve parity invariance, and a "natural" convention for them is $\xi_+ \equiv \langle \gamma\gamma^* \rangle$ and $\xi_- \equiv \langle \gamma\gamma \rangle$ [101], where the angle brackets denote averaging over galaxy pairs. In terms of tangential (t) and cross ($\times$) components defined along the line that connects each pair of galaxies a, b, we have:

$$\xi_\pm = \langle \gamma_{t,a}\gamma_{t,b} \rangle_{ab} \pm \langle \gamma_{\times,a}\gamma_{\times,b} \rangle_{ab}. \quad (2)$$

In practice we do not have direct access to the shear field, but rather estimate it via per-galaxy ellipticities (although see [102] for an alternative approach). Correlating galaxies in a pair of redshift bins (i, j) we define,
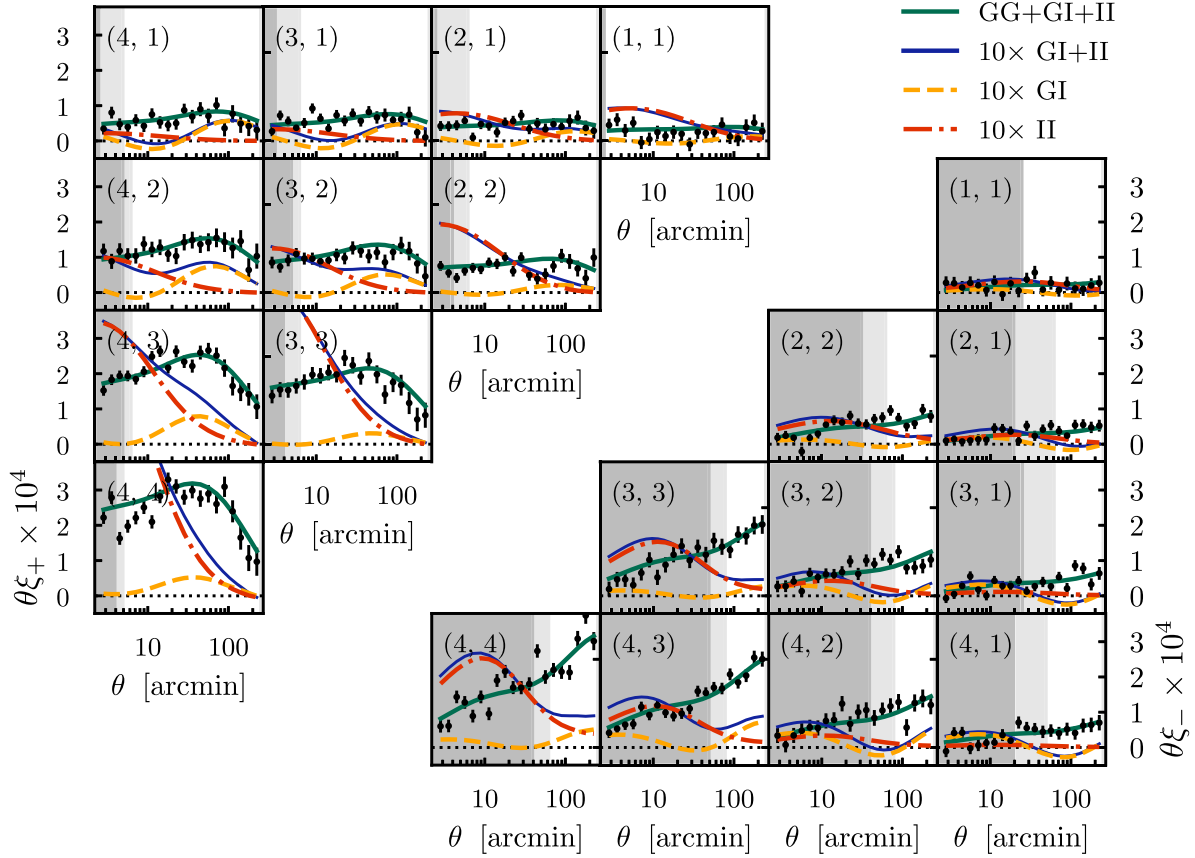
FIG. 2. Cosmic shear two-point correlation measurements from DES Y3. We show here ξ_+ and ξ_- (black data points, upper left and lower right halves respectively), with the different panels showing different combinations of redshift bins; in all cases the error bars come from our fiducial analytic covariance matrix. The lighter grey bands represent scales removed from our fiducial analysis, while the darker are the equivalent for the ΛCDM Optimized analysis. Also shown are the best-fit theory curve in ΛCDM (solid green) and the intrinsic alignment contributions to the signal: GI (dashed yellow), II (dot-dashed red), and GI + II (solid blue). For clarity, we multiply the IA contributions by a factor of 10, and in most bins the total IA signal is $\sim 1\%$ of GG + GI + II. The detection significance of the cosmic shear signal after fiducial scale cuts is 27. The χ^2 per effective d.o.f of the ΛCDM model is $237.7/222 = 1.07$ (a *p*-value of 0.22).

$$\xi_{\pm}^{ij}(\theta) = \frac{\sum_{ab} w_a w_b (\hat{e}_{t,a}^i \hat{e}_{t,b}^j \pm \hat{e}_{\times,a}^i \hat{e}_{\times,b}^j)}{\sum_{ab} w_a w_b R_a R_b}, \qquad (3)$$

with inverse variance weighting w[5] (unlike in Y1, where such weighting was not included) and response factors R that account for shear and selection biases (see [78] for details), and where the sums run over pairs of galaxies a, b, for which the angular separation falls within the range $|\boldsymbol{\theta} - \Delta\boldsymbol{\theta}|$ and $|\boldsymbol{\theta} + \Delta\boldsymbol{\theta}|$. Both ξ_+ and ξ_- are measured using twenty log-spaced θ bins between 2.5 and 250 arcminutes, with $i, j \in (1, 2, 3, 4)$. As discussed later, not all of the twenty angular bins are utilized in our likelihood analysis. We also assume the response matrix is diagonal and that the selection part is scale independent. The ellipticities that enter Eq. (3) are corrected for residual mean shear, such that

---

[5]Although referred to as such, the catalog weights only approximate inverse variance weighting. See Gatti *et al.* [78], Sec. IV C for details.
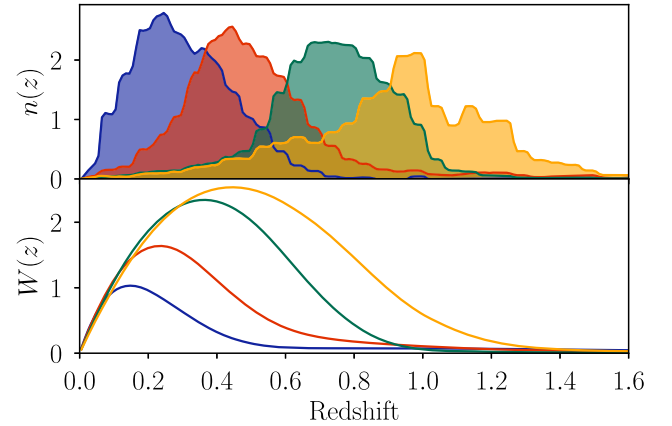
FIG. 3. The estimated redshift distributions and lensing kernels for the fiducial source galaxy sample used in this work. Most of the sensitivity of the DES Y3 cosmic shear signal to large scale structure is in the range between $z = 0.1$ and $z = 0.5$, where individual kernels peak. Each distribution is independently normalized over the redshift range $z = 0-3$. The total effective number density [98] of sources is $n_{\rm eff} = 5.59$ galaxies per square arcminute and is divided almost equally into the 4 redshift bins.

$\hat{e}_k^i \equiv e_k^i - \langle e_k \rangle_i$ for components $k \in (1, 2)$ and redshift bin i, again following the Y1 methodology [7]. We show the resulting two-point functions, which are measured using using TreeCorr[6] [103], in Fig. 2, alongside best fitting theory predictions.

C. Data covariance matrix

We model the statistical uncertainties in our combined measurements of $\xi_\pm$ as a multivariate Gaussian distribution. The disconnected 4-point function part of the covariance matrix of that data vector (the Gaussian covariance part) is described in [85] and includes analytic treatment of bin averaging and sky curvature. We also verify in that paper that expected fluctuations in $\Delta\chi^2$ between the measurement and our maximum posterior model do not significantly impact on our estimates of cosmological parameters. Our modeling of the connected 4-point function part of the covariance matrix and the contribution from super-sample covariance uses the public CosmoCov[7] [104] code, which is based on the CosmoLike framework [105].

We use the RMS per-component shape dispersion σ_e and effective number densities n_{eff} specified in Table 1 of [72] to calculate the shape-noise contribution to the covariance, and additionally account for survey geometry effects. We follow previous cosmic shear analyses in using a covariance matrix that assumes a baseline cosmology (see [6] for a different approach). That is, we assume a fiducial set of input parameters for the initial covariance matrix and run cosmological chains using this first guess. The covariance is then recomputed at the best fit from this first iteration, and the final chains are run. We find this update to have negligible effects on the cosmic shear constraints presented in this paper.

D. Blinding

We implement a three-stage blinding strategy, performing transformations to the catalog, data vector, and parameters in order to obscure the cosmological results of the analysis. By disconnecting the people carrying out the analysis from the impact their various choices are having on the eventual cosmological results, the aim is to avoid unconscious biases, either toward or away from previous results in the literature. Although the approaches differ somewhat, all of the major cosmic shear collaborations have adopted a similar philosophy regarding the necessity of blinding [5–7,106,107].

The first level of blinding follows a similar method to that used in Y1 [108], and is discussed in Gatti *et al.* [78] (their Sec. II C). In short, the process involves a transformation of the shear catalog, where galaxy shapes are scaled by a random multiplicative factor. The second level

is a transformation of the data vector using the method described in Muir *et al.* [87]. We compute model predictions at two sets of input parameters: an arbitrary reference cosmology Θ_{ref} and a shifted cosmology $\Theta_{\mathrm{ref}} + \Delta\Theta$, where $\Delta\Theta$ is drawn randomly in wCDM parameter space. The difference between these model predictions is then applied to the measured $\xi_\pm$ data vector prior to its analysis. The final stage of blinding is at the parameter level, and entails obscuring the axes of contour plots (effectively equivalent to shifting contours randomly in parameter space, preserving constraining power but making external consistency testing impossible). A detailed checklist of the tests that must be fulfilled before each stage of blinding can be removed can be found in Dark Energy Survey Collaboration [73].

From a modeling perspective, passing the tests we describe in Sec. V and the further tests on synthetic data described in DeRose *et al.* [88] and Krause *et al.* [89] fulfills our unblinding requirements. A set of internal consistency tests for cosmic shear must also be passed and are described in Amon *et al.* [72].

IV. FIDUCIAL MODEL AND ANALYSIS CHOICES

A predictive physical model for cosmic shear has a number of requirements; first, any systematic deviations or effects omitted from the model must be comfortably subdominant to uncertainties on the data; and second, the implementation must be numerically stable at all points within the prior volume. We also aim for redundancy, and implement the full pipeline in two independent codes: CosmoSIS[8] [109] and CosmoLike [105], which are verified to be in agreement to within a negligible $\Delta\chi^2$ [89].

In this section, we outline our baseline model for $\xi_\pm^{ij}(\theta)$ and discuss how it meets the above criteria. We subsequently show the cosmological constraints from these analysis choices in Sec. VI. To test the robustness of this baseline model, we later relax its main approximations and assumptions and show variations of analysis choices in Sec. VII.

A. Sampling and parameter inference

For all parameter inference presented in this paper, we assume the likelihood of the data given the model M with parameters $\mathbf{p}$ to be a multivariate Gaussian:

$$\ln \mathcal{L}(\hat{\mathbf{D}}|\mathbf{p}, M) = -\frac{1}{2}\chi^2 + \mathrm{const.,} \qquad (4)$$

$$\chi^2 = (\hat{\mathbf{D}} - \mathbf{T}_M(\mathbf{p}))^T \mathbf{C}^{-1}(\hat{\mathbf{D}} - \mathbf{T}_M(\mathbf{p})), \qquad (5)$$

---

[6]https://github.com/rmjarvis/TreeCorr.
[7]https://github.com/CosmoLike/CosmoCov.

[8]https://bitbucket.org/joezuntz/cosmosis.

where $\mathbf{C}$ is the data covariance matrix and $\mathbf{T}_M(\mathbf{p})$ is the theory prediction vector for a data vector $\hat{\mathbf{D}}$, a concatenated version of all elements of the tomographic cosmic shear data (with length $N_D = N_\theta N_z (N_z + 1)$, where N_θ is the number of angular bins included in each correlation function after scale cuts (N_θ varies depending on the redshift bins, and equals 20 before cuts) and $N_z = 4$ is the number of broad redshift bins). Since we are incorporating shear ratios at the inference level (see Sec. IV F), the final likelihood used in our analyses is the sum of two parts, $\ln \mathcal{L} = \ln \mathcal{L}_{2pt} + \ln \mathcal{L}_{SR}$, which are assumed to be independent [81].

As we aim to perform a Bayesian analysis, the *a posteriori* knowledge of the parameters given the observed data, denoted by $\mathcal{P}(\mathbf{p}|\hat{\mathbf{D}}, M)$, depends not only on the likelihood but also on prior $\Pi(\mathbf{p}|M)$. These pieces are related via Bayes' theorem:

$$\mathcal{P}(\mathbf{p}|\hat{\mathbf{D}}, M) = \frac{\mathcal{L}(\hat{\mathbf{D}}|\mathbf{p}, M)\Pi(\mathbf{p}|M)}{P(\hat{\mathbf{D}}|M)}, \quad (6)$$

where $P(\hat{\mathbf{D}}|M)$ is the so-called evidence of the data. Sampling of the posterior is carried out using Polychord ([110]; with 500 live points and tolerance 0.01). These settings have been tested to demonstrate the accuracy of the posteriors and Bayesian evidence estimates. Although sampling gives a rather noisy estimate of the best-fit point in the full parameter space, the *Maximum a Posteriori* (MAP) quoted in Sec. VI A, we verify that standard Polychord outputs, in practice, offer a reasonable estimate of that point when compared to a MAP optimizer.[9] Throughout this paper, we report parameter constraints using the MAP value and 1D marginalized summary statistics in the form:

$$\text{Parameter} = \text{1D mean}^{+\text{upper 34\% bound}}_{-\text{lower 34\% bound}} \quad (\text{MAP value}).$$

The ratio of evidences is a well-defined quantity for model-testing within a single dataset to indicate a preference for one modeling choice (M_1, with parameters $\mathbf{p}_1$) over another (M_2, $\mathbf{p}_2$):

$$R_{M_1/M_2} = \frac{P(\hat{\mathbf{D}}|M_1)}{P(\hat{\mathbf{D}}|M_2)} = \frac{\int d\mathbf{p}\mathcal{L}(\hat{\mathbf{D}}|\mathbf{p}_1, M_1)P(\mathbf{p}_1|M_1)}{\int d\mathbf{p}\mathcal{L}(\hat{\mathbf{D}}|\mathbf{p}_2, M_2)P(\mathbf{p}_2|M_2)}. \quad (7)$$

The evidence ratio has the advantage of naturally penalizing models of excessive parameter space volume, but needs to be interpreted using e.g. the Jeffreys scale [111], which somewhat arbitrarily differentiates between "strong" and "weak" model preferences. Our main use of evidence

---

[9]We run the MaxLike sampler in Posterior mode for this test (https://bitbucket.org/joezuntz/cosmosis/wiki/samplers/maxlike).

ratios is to help assessing model preference in the context of IA complexity in Sec. VI C 2.

B. Modeling cosmic shear

The two-point cosmic shear correlations $\xi_\pm^{ij}(\theta)$ are related to the nonlinear matter power spectrum (and thus to the growth and evolution of structure). The key quantity that dictates how much a galaxy on a particular line of sight is distorted, is known as the *convergence* κ. That is, the weighted mass overdensity δ, integrated along the line-of-sight to the distance of the source χ_s:

$$\kappa(\theta) = \int_0^{\chi_s} d\chi W(\chi)\delta(\theta, \chi). \quad (8)$$

The weight for a particular lens plane, quantified below in Eq. (10), is sensitive to the relative distances of the source and the lens; it is via this geometrical term that cosmic shear probes the expansion history of the Universe. Fitting all the auto- and cross-redshift bin correlations simultaneously significantly improves the cosmological constraining power [19], both because it helps to untangle the signal at different epochs, and because it (partially) breaks the degeneracy with intrinsic alignments (see also Sec. IV D).

Under the Limber approximation [112,113], the 2D convergence power spectrum in tomographic bins i and j, $C_\kappa^{ij}(\ell)$ is related to the full 3D matter power spectrum as:

$$C_\kappa^{ij}(\ell) = \int_0^{\chi(z_{\max})} d\chi \frac{W^i(\chi)W^j(\chi)}{\chi^2} P_\delta\left(\frac{\ell + 1/2}{\chi}, z(\chi)\right), \quad (9)$$

where P_δ is the nonlinear matter power spectrum and the lensing efficiency kernels are given by

$$W^i(\chi) = \frac{3H_0^2\Omega_m}{2c^2}\frac{\chi}{a(\chi)}\int_\chi^{\chi_H} d\chi' n^i(z(\chi'))\frac{dz}{d\chi'}\frac{\chi' - \chi}{\chi'}. \quad (10)$$

The source galaxy redshift distribution $n^i(z)$ here is normalized to unity. Clearly, the amplitude of C_κ responds directly to σ_8^2, and to Ω_m via the power spectrum, and to $\Omega_m h^2$ via the lensing kernel, which gives rise to a characteristic banana-shaped degeneracy in $\sigma_8 \times \Omega_m$. The combination of parameters most strongly constrained by cosmic shear is a derived parameter, commonly referred to as $S_8 \equiv \sigma_8(\Omega_m/0.3)^{0.5}$.

By decomposing κ into E- and B-mode components [114,115] and in a full-sky formalism, one can express the angular two point shear correlations as:

$$\xi_\pm^{ij}(\theta) = \sum_\ell \frac{2\ell + 1}{2\pi \ell^2 (\ell + 1)^2} \left[G_{\ell,2}^+(\cos\theta) \pm G_{\ell,2}^-(\cos\theta) \right]$$
$$\times \left[C_{EE}^{ij}(\ell) \pm C_{BB}^{ij}(\ell) \right], \tag{11}$$

where the functions $G_\ell^\pm(x)$ are computed from Legendre polynomials $P_\ell(x)$ and averaged over angular bins [see Krause *et al.* [89], Eqs. (19) and (20)]. It is also worth bearing in mind that, in practice, the angular spectra in Eq. (11) are not in fact pure cosmological convergence spectra C_κ, but rather shear spectra C_γ, which include contributions from intrinsic alignments (see Sec. IV D), and additional higher order terms are explored later.

Since the lensing kernel in Eq. (10) acts as a redshift filter, which modulates sensitivity to P_δ in Eq. (9), it is informative to show its redshift dependence; we do so in the lower panel of Fig. 3, for the fiducial Y3 redshift distributions. As shown there, the DES Y3 cosmic shear signal is sensitive to a relatively broad range, with kernels peaking between approximately $z = 0.1$ and $z = 0.5$.

Similarly, the polynomials in Eq. (11) mix together a range of physical distances into any given angular scale. We can elucidate this by writing $\xi_\pm^{ij}$ as an integral over $\ln k$ (e.g. [116]) to obtain:

$$\xi_\pm^{ij}(\theta) = \int_{-\infty}^{+\infty} d\ln k \, \mathcal{P}(k) \tag{12}$$

where

$$\mathcal{P}(k) = \frac{k}{2\pi} \sum_\ell [G_{\ell,2}^+(\cos\theta) \pm G_{\ell,2}^-(\cos\theta)]$$
$$\times W^i(\chi) W^j(\chi) P_\delta(k, z(\chi)), \tag{13}$$

with $\chi = (\ell + 1/2)/k$. We show $d\ln\xi_\pm(\theta)\ln k = \mathcal{P}(k)/\xi_\pm(\theta)$ for representative θ scales in Fig. 4. This shows the sensitivity of our cosmic shear signal at a given angular scale to modes of the matter power spectrum. Our scale cuts, defined in Sec. IV G, eventually remove most of the sensitivity to $k > 1 \, h\,\mathrm{Mpc}^{-1}$.

The remainder of this section motivates the ingredients introduced in Eqs. (9)–(11) such as the nonlinear power spectrum prescription and the set of scales for which the signal is not significantly contaminated by unmodeled physics.

C. Nonlinear power spectrum

On the largest of physical scales, growth is linear and well described by a purely linear matter power spectrum $P_\delta^{\mathrm{lin}}(k)$. To evaluate P_δ^{lin} we use the Boltzmann code CAMB[10] [117], as implemented in CosmoSIS. On smaller
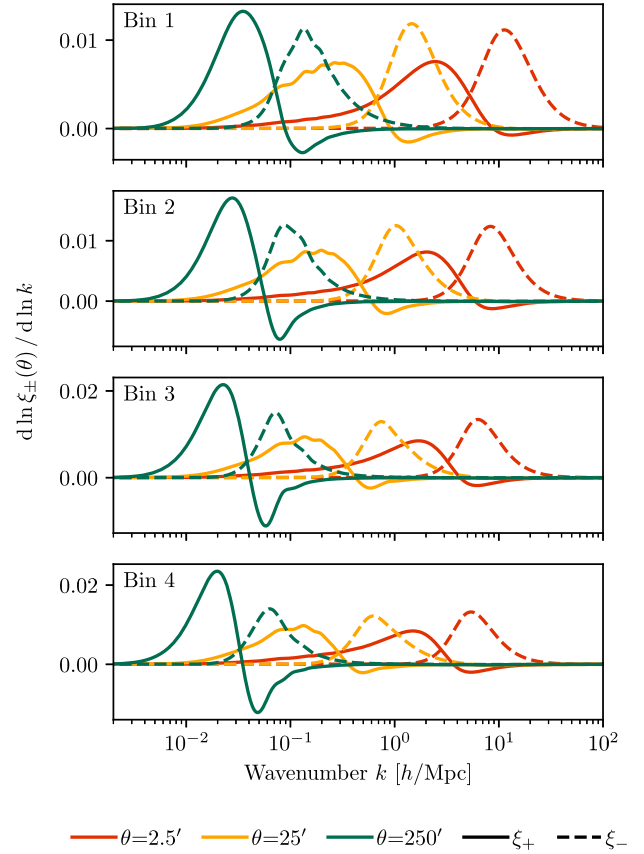

FIG. 4. Window functions of ξ_+ (solid curves) and ξ_- (dashed curves) over k-wave numbers of the matter power spectrum at representative angular separations. Notice that our smallest angular scales (after cuts) in ξ_+ and ξ_- are around 2.5 arcminutes and 30 arcminutes respectively, which means that only a relatively small contribution to the full signal comes from wave numbers above $k \sim 1 \, h/\mathrm{Mpc}$.

scales, however, this is not true, and one also needs a model for nonlinear growth. Our fiducial model for the nonlinear matter power spectrum $P_\delta(k)$ is the HaloFit functional prescription [118,119]. We have made scale cuts to remove the parts of the data vector affected by baryonic effects, as described in Sec. IV G; this largely removes the sensitivity to wavenumbers $k > 1 \, h\,\mathrm{Mpc}^{-1}$. For $k < 1 \, h\,\mathrm{Mpc}^{-1}$, Takahashi *et al.* [119] reports an uncertainty on the HaloFit model of 5%. In Krause *et al.* [89] we demonstrate, by substituting HaloFit for HMcode[11] [120], the Euclid Emulator [121], or the Mira-Titan Emulator [122] that for cosmic shear alone we are insensitive to this choice. In the context of the Y3 3×2pt analysis, the distinction between these three models is more nuanced, and we refer the reader to Krause *et al.* [89] for a full justification of the use of HaloFit.

---

[10]http://camb.info.

[11]https://github.com/alexander-mead/HMcode.

D. Intrinsic alignments

Galaxies are not idealized tracers of the underlying matter field, but rather astrophysical bodies, which are subject to local interactions. To account for this added complexity, the observed shape of a galaxy can be decomposed into two parts, the shear induced by gravitational lensing (G) and the intrinsic shape (I) induced by the local environment: $\gamma = \gamma^{\mathrm{G}} + \gamma^{\mathrm{I}}$. In this section, we consider only the correlated intrinsic component, and not the intrinsic "shape noise," which contributes to the covariance but not the signal.

The term *intrinsic alignments* covers two contributions from environmental interactions: (a) intrinsic shape— intrinsic shape correlations between galaxies that are physically close to each other, and (b) shear-intrinsic correlations between galaxies on neighboring lines of sight. Known as II and GI contributions respectively, and contributing on similar angular scales to the cosmological lensing signal, these terms constitute a significant systematic in weak lensing analyses. Including IA contributions, the observed E-mode angular power spectrum is written

$$C^{ij}_{\gamma,\mathrm{EE}}(\ell) = C^{ij}_{\mathrm{GG}}(\ell) + C^{ij}_{\mathrm{GI}}(\ell) + C^{ij}_{\mathrm{IG}}(\ell) + C^{ij}_{\mathrm{II,EE}}(\ell). \quad (14)$$

Nonlinear models of IA, as discussed below, can also produce a nonzero B-mode power spectrum:

$$C^{ij}_{\gamma,\mathrm{BB}}(\ell) = C^{ij}_{\mathrm{II,BB}}(\ell). \quad (15)$$

Assuming the Limber approximation as before, the two IA $C(\ell)$s are given by:

$$C^{ij}_{\mathrm{GI}}(\ell) = \int_0^{\chi_{\mathrm{H}}} d\chi \frac{W^i(\chi) n^j(\chi)}{\chi^2} P_{\mathrm{GI}}\left(\frac{\ell+1/2}{\chi}, z(\chi)\right), \quad (16)$$

and

$$C^{ij}_{\mathrm{II}}(\ell) = \int_0^{\chi_{\mathrm{H}}} d\chi \frac{n^i(\chi) n^j(\chi)}{\chi^2} P_{\mathrm{II}}\left(\frac{\ell+1/2}{\chi}, z(\chi)\right), \quad (17)$$

These expressions are generic, and are valid regardless of which model is used to predict P_{GI} and P_{II} (see the following subsections).

1. IA and the tidal field

It is typically assumed that the correlated component of galaxy shapes is determined by the large-scale cosmological tidal field. The simplest relationship, which should dominate on large scales and for central galaxies, involves the "tidal alignment" of galaxy shapes, producing a linear dependence [123,124]. In this case, one can relate the intrinsic shape component to the gravitational potential at the assumed time of galaxy formation ϕ_*:

$$(\gamma^{\mathrm{I}}_1, \gamma^{\mathrm{I}}_2) = A_1(z)\left(\frac{\partial^2}{\partial x^2} - \frac{\partial^2}{\partial y^2}, 2\frac{\partial^2}{\partial x \partial y}\right)\phi_*, \quad (18)$$

where the proportionality factor $A_1(z)$ captures the response of intrinsic shape to the tidal field. More complex alignment processes, including "tidal torquing," relevant for determining the angular momentum of spiral galaxies, are captured in a nonlinear perturbative framework, which we refer to as "TATT" (tidal alignment and tidal torquing; [65]). In this more general model, we use nonlinear cosmological perturbation theory to express the intrinsic galaxy shape field, measured at the location of source galaxies [125], as an expansion in the matter density field δ and tidal field s_{ij}:

$$\bar{\gamma}^{\mathrm{IA}}_{ij} = A_1 s_{ij} + A_{1\delta} \delta s_{ij} + A_2 \sum_k s_{ik} s_{kj} + \cdots, \quad (19)$$

where s_{ij} is the gravitational tidal field, which at any given position $\mathbf{x}$ is a 3×3 tensor (see [126] for a formal definition).

Although the terms in the model can be associated with physical mechanisms, they can also be viewed as effective contributions to intrinsic shape correlations from small-scale physics. See also Schmitz *et al.* [127], Tugendhat and Schäfer [128], Vlah *et al.* [129] for further discussion of the perturbative approach and Fortuna *et al.* [130] for a halo model treatment of IA.

2. Model implementation: NLA and TATT

Within the TATT framework, three parameters capture the relevant responses to the large-scale tidal fields (see [65] for more details): A_1, A_2, and $A_{1\delta}$, corresponding respectively to a linear response to the tidal field (tidal alignment), a quadratic response (tidal torquing), and a response to the product of the density and tidal fields. To date, the most frequently used intrinsic alignment model in the literature is known as the nonlinear alignment model (NLA; [131,132]), an empirically-based modification of the linear alignment (LA) model of Catelan *et al.* [123] and Hirata and Seljak [124], in which the fully nonlinear tidal field is used to calculate the tidal alignment term. Within the TATT framework, the NLA model corresponds to only A_1 being nonzero in Eq. (19). The GI and II power spectra then have the same shape as the nonlinear matter power spectrum, but are modulated by $A_1(z)$:

$$P_{\mathrm{GI}}(k, z) = A_1(z) P_\delta(k, z),$$
$$P_{\mathrm{II}}(k, z) = A_1^2(z) P_\delta(k, z). \quad (20)$$

Note that the nonlinear power spectrum and the IA amplitudes are functions of redshift. In the following, the z dependence of the IA amplitudes and various k dependent terms is left implicit. More generally, in the TATT model, the GI and II power spectra are constructed with the relevant correlations of tidal and density fields:

$$P_{\text{GI}}(k) = A_1 P_\delta(k) + A_{1\delta} P_{0|0E}(k) + A_2 P_{0|E2}(k), \quad (21)$$

$$\begin{aligned} P_{\text{II,EE}}(k) = {}& A_1^2 P_\delta(k) + 2A_1 A_{1\delta} P_{0|0E}(k) + A_{1\delta}^2 P_{0E|0E}(k) \\ & + A_2^2 P_{E2|E2}(k) + 2A_1 A_2 P_{0|E2}(k) \\ & + 2A_{1\delta} A_2 P_{0E|E2}(k), \end{aligned} \quad (22)$$

$$\begin{aligned} P_{\text{II,BB}}(k) = {}& A_{1\delta}^2 P_{0B|0B}(k) + A_2^2 P_{B2|B2}(k) \\ & + 2A_{1\delta} A_2 P_{0B|B2}(k). \end{aligned} \quad (23)$$

In this work, these k-dependent terms are evaluated using FAST-PT [133,134], as implemented in CosmoSIS. The model, including the full expressions for these power spectra is set out in some depth in Blazek *et al.* [65] [see their Eqs. (37)–(39) and appendix A], and we refer the reader to that paper for technical details. The k-dependent contributions are modulated by the redshift-dependent amplitudes A_1, A_2, and $A_{1\delta}$. We define the first two with the following convention:

$$A_1(z) = -a_1 \bar{C}_1 \frac{\rho_{\text{crit}} \Omega_{\text{m}}}{D(z)} \left(\frac{1+z}{1+z_0} \right)^{\eta_1}, \quad (24)$$

$$A_2(z) = 5 a_2 \bar{C}_1 \frac{\rho_{\text{crit}} \Omega_{\text{m}}}{D^2(z)} \left(\frac{1+z}{1+z_0} \right)^{\eta_2}, \quad (25)$$

where $D(z)$ is the linear growth factor, ρ_{crit} is the critical density, and $\bar{C}_1$ is a normalization constant, by convention fixed at $\bar{C}_1 = 5 \times 10^{-14} M_\odot h^{-2} \text{Mpc}^2$, obtained from SuperCOSMOS (see [135]). The leading factor of 5 in Eq. (25) is included to account for the difference in the windowed variance produced by the TA and TT power spectra. With this factor included, the TA and TT contributions to P_{II} at $z = 0$, averaged over this window, should be roughly equal if $a_1 = a_2$, aiding in the interpretation of the best fitting values. Note that this is a matter of convention only, and does not affect our final cosmological results. The denominator z_0 is a pivot redshift, which we fix to the value 0.62.[12] The dimensionless amplitudes (a_1, a_2) and power law indices (η_1, η_2) are free parameters in this model.

As mentioned above, the model also includes the $A_{1\delta}$ contribution, corresponding to the product of the density and tidal fields. This term was originally motivated by the modulation of the IA signal due to the galaxy density weighting (i.e. the fact that the shape field is preferentially sampled in overdense regions [125]). In this case, within the TATT model, we have

$$A_{1\delta} = b_{\text{TA}} A_1, \quad (26)$$

---

[12]The value was chosen in DES Y1 to be approximately equal to the mean source redshift. We choose to maintain that value to allow for an easier comparison of the IA amplitudes with those results.

where b_{TA} is the linear bias of source galaxies contributing to the tidal alignment signal. In our baseline analysis, rather than fixing b_{TA} to this bias value, we sample over it with a wide prior, allowing the $A_{1\delta}$ contribution to capture a broader range of nonlinear alignment contributions. We note that this is a departure from previous studies to have used this model [7,65,136], all of which held $b_{\text{TA}} = 1$ fixed. The motivation for this change is set out in Sec. V. As can be seen from Eq. (21)–(23), in the limit $a_2, b_{\text{TA}} \to 0$, the TATT model reduces to the NLA model. It is thus useful to think of NLA as a subspace of the more complete TATT model, rather than a distinct, alternative model. Given the sensitivity of IAs to the details of the galaxy selection, and in the absence of informative priors, we choose to marginalize over all five IA parameters $(a_1, a_2, \eta_1, \eta_2, b_{\text{TA}})$, governing the amplitude and redshift dependence of the IA terms, with wide flat priors (see Sec. IV H). While a redshift evolution in the form of a power law, captured by the index η_i, is a common assumption, the $A_i(z)$ coefficients could, in theory, have a more complicated redshift dependence. We seek to test the impact of this assumption by rerunning our analysis with a more flexible parametrization, whereby the IA amplitude $A_{1,i}$ in each redshift bin is allowed to vary independently. The results of this exercise can be found in Sec. VII B.

It is finally worth remarking that the TATT model predicts a nonzero B-mode power spectrum $P_{\text{II,BB}}$. This extra signal component is incorporated into our modeling, and propagated into $\xi_\pm$ via Eq. (11). $P_{\text{II,BB}}$ is expected to be small since the testing carried out in [78] points to no statistically significant detection of B-modes in the DES Y3 shape catalog.

A visual representation of the II and GI signals, as predicted at the best-fitting point in parameter space from our fiducial analysis, can be found in Fig. 2.

E. Modeling nuisance parameters: Shear bias and photo-z error

In addition to the parameters associated with the cosmological and IA models, there are a number of additional parameters included in our fiducial analysis, which are intended to absorb known sources of uncertainty. First of all, we follow the majority of previous cosmic shear analyses, and parametrize errors in the redshift distributions as uniform shifts in their mean, which transform the assumed distribution in a given bin i as:

$$n^i(z) \to n^i(z - \Delta z^i). \quad (27)$$

This leaves us with four nuisance parameters (Δz^{1-4}), which are marginalized with informative priors (see Sec. IV H). This simple marginalization scheme was validated with a more complete method, known as HyperRank Cordero *et al.* [82], which uses a large ensemble of possible redshift distributions (typically of order 1000)

generated using the SOMPZ pipeline [79]. The basic aim of this method is to capture the range of plausible variations in the full shape of the distributions (not only their mean), and also the correlations between bins. Although in our particular setup the simpler parametrization was found to be sufficient, the tests in Cordero *et al.* [82] and Amon *et al.* [72] show the crucial validation of that choice.

Another important source of uncertainty is the shape calibration process, and particularly its response to blending MacCrann *et al.* [77]. The common way of describing such effects [49,137] is a simple rescaling of the two-point function model prediction

$$\xi_\pm^{ij} \to (1 + m^i)(i + m^j) \times \xi_\pm^{ij}, \qquad (28)$$

where again the indices i, j indicate redshift bins, and m is assumed to be redshift and scale independent within each bin. This is our fiducial parametrization. As explained in Sec. II C, this approach is an approximation to the more complete methodology set out in MacCrann *et al.* [77] (see in particular their Sec. 6.5), which incorporates the redshift-dependent impact of blending on the source redshift distributions. Nevertheless, an extensive series of tests indicate that Eq. (28) is sufficient for the statistical power of DES Y3 (see [72,77]).

F. Incorporating shear ratios

In the DES Y3 analysis, we also incorporate small-scale shear ratios (SR) at the likelihood evaluation level. *This likelihood is included in all our present constraints unless explicitly noted otherwise.* This concept and its DES application is outlined in more detail by Sánchez *et al.* [81]. Essentially, SR is an additional lensing-based data vector with 9 data points made up of measured galaxy-galaxy lensing ratios. It is nearly independent of cosmology and galaxy bias, but responds to (and thus constrains) redshift distributions and intrinsic alignments. Note that this particular analysis feature is different from Y1 and most current cosmic shear results, a detail that should be kept in mind in any comparison of our findings with previous results.

We use SR on small scales that are not used in the 3×2pt likelihood (< 6 Mpc/h), where uncertainties are dominated by galaxy shape noise, such that the likelihood can be treated as independent of that from the $\xi_\pm$ (and indeed the full 3×2pt) data. On these scales the SR measurement is only very weakly dependent on the matter power spectrum, and so immune to uncertainties in modeling P_δ on small scales [81]. In this work, we only employ SR as obtained from the fiducial MagLim lens sample Porredon *et al.* [138], and marginalize over its required nuisance parameters. These are a free (linear) galaxy bias coefficient per lens bin (which are unconstrained by cosmic shear and have no impact on the final posteriors), as well as lens redshift parameters (three shift Δz_l and three width parameters δ_z; see [139]), on which we have relatively tight priors. The main impact of including

SR is an improvement in constraints on IAs and redshift nuisance parameters. Through internal degeneracies, this translates into significantly improved constraints on S_8, of around 30% in our fiducial analysis setting. Further discussion can be found in Sánchez *et al.* [81] (Sec. 6 and Fig. 10) and Amon *et al.* [72] (Sec. X and Fig. 11). In particular, those papers also assess the impact of utilizing redMaGiC, an alternative DES Y3 lens sample [140–142], in order to obtain the shear ratios.

G. Angular scale cuts

1. Baryons

The impact of baryons on the matter power spectrum on cosmological scales is a source of considerable uncertainty [143–145]. While feedback processes from active galactic nuclei (AGN) and supernovae heat up the halo environment and tend to suppress matter clustering, metal enrichment can offer cooling channels that in fact increase power on small scales. These effects also depend on redshift and galaxy evolution [146].

As a fiducial strategy for mitigating the uncertainties coming from baryonic physics, we employ a gravity-only matter power spectrum (CAMB+HaloFit) as described in Sec. IV C, and remove angular scales from the data vector which are significantly affected by feedback processes. We have additionally verified with synthetic data that marginalizing over baryonic halo model parameters with conservative priors does not lead to an actual gain in the $S_8 \times \Omega_m$ subspace. Specifically, we use HMcode [120] and free both the halo concentration amplitude A with a flat prior [1.0, 7.5] and the bloating parameter η_0 with a flat prior [0.4, 1.0]. These priors were chosen such that all baryonic scenarios tested in Mead *et al.* [120] would be encapsulated by the allowed halo model modification. We find, with these fairly conservative priors, that attempting to model progressively smaller scales in synthetic data vectors results in tighter constraints on the baryon nuisance parameters A and η_0, while leaving the constraining power on $S_8 \times \Omega_m$ approximately unchanged.

2. Determining scale cuts

We define scale cuts based on the $\Delta\chi^2$ between noiseless synthetic cosmic shear data vectors, generated with and without a baryonic "contamination," according to Eq. (5). For the baryonic data vector, we use the OWLS [147,148] matter power spectrum. The AGN-feedback implementation in this suite of simulations represents one of the most extreme scenarios in the literature, and thus characterizes the most conservative case for the baryonic contamination we expect our analysis to be safe against.

To determine scale cuts for the cosmic shear two-point functions $\xi_\pm^{ij}$, we evenly distribute the $\Delta\chi^2$ threshold among tomographic bins, and limit each of the shear two-point angular functions:

$$(\xi^{ij}_{\pm,\text{baryon}} - \xi^{ij}_{\pm,\text{base}})^{\text{t}} \mathbf{C}^{-1}_{\text{sub}} (\xi^{ij}_{\pm,\text{baryon}} - \xi^{ij}_{\pm,\text{base}}) < \frac{\Delta\chi^2_{\text{threshold}}}{N},$$

$$(29)$$

where $N = 20$ is the number of cross-correlations between four tomographic redshift bins in the two shear correlations $\xi_\pm$. The $\mathbf{C}^{-1}_{\text{sub}}$ submatrix of the inverse covariance matrix corresponds to the specific tomographic bin. For each element of $\xi^{ij}_\pm$, we find the minimum angular separation that satisfies Eq. (29) and exclude data points at smaller separations.

For a given threshold, we run two chains using the fiducial pipeline: one on a baseline (systematics-free) synthetic data vector and one on a contaminated synthetic data vector which includes the modification of the OWLS-AGN matter power spectrum. Our most important criterion for selecting a threshold is that the peaks of the baseline and contaminated posteriors in the 2-D parameter subspace of $S_8 \times \Omega_{\text{m}}$ must be separated by less than 0.3σ. We make this analysis additionally conservative by fixing redshift and shear uncertainties and the neutrino mass. It is also worth noting that scale cuts for the cosmic shear correlations $\xi^{ij}_\pm$ are determined in tandem with the $2 \times 2\text{pt}$ and $3 \times 2\text{pt}$ analyses. That means a candidate cut passing the $< 0.3\sigma$ threshold for cosmic shear is then combined with cuts from the analogous $2 \times 2\text{pt}$ analysis, and the finally selected scale cuts for cosmic shear and $2 \times 2\text{pt}$ are those which also satisfy $3 \times 2\text{pt} < 0.3\sigma$. In practice, this procedure ensures that the full DES Y3 analysis is optimized, as opposed to each probe alone being optimally constraining (although see the discussion in Sec. IV G 3).

After an iterative procedure, we finally select the scale cuts that lead to a threshold of $\Delta\chi^2 < 0.5$ for cosmic shear systematics. These cuts are shown in grey bands in Figs. 2 and 5, and roughly correspond to bounds that are, at the smallest, $\theta_{\text{min},+} = 2.4$ and $\theta_{\text{min},-} = 30$ arcmin in ξ_+ and ξ_- respectively, but differ significantly between redshift bin pairs. The large-scale limit of the data vector is 250 arcmin, chosen to match the DES Y1 analysis [7]. After cuts, we are left with 166 and 61 angular bins in ξ_+ and ξ_-, or a total of 227 data points.

Figure 5 demonstrates that, by making our data immune to the feedback impact of OWLS-AGN, we are also safely excluding parts of the data vector that are affected by systematic uncertainty due to the matter power spectrum modeling (Euclid Emulator; [121]), baryonic feedback (MassiveBlack-II, Horizon-AGN, and Eagle; respectively [149–151]) and higher order shear corrections including reduced shear and source magnification (Sec. V A 2 and [89]). See Sec. V for more details. It is important to note that error bars on ξ_+ and ξ_- are, at their smallest, around 15% and 20% of the signal, so the deviations seen in Fig. 5 are well below the sensitivity of our data. We refer the reader to Krause *et al.* [89] for an exploration of different

baryonic power spectra, and in particular other extreme feedback cases such as Illustris [152].

3. ΛCDM *Optimized scale cuts*

As discussed above, our fiducial choice of scale cuts, by construction, optimizes the joint $3 \times 2\text{pt}$ analysis of Dark Energy Survey Collaboration [73], which includes not just cosmic shear, but also galaxy clustering and galaxy-lensing. Those scale cut tests were also required to pass the same tolerance threshold in both ΛCDM and wCDM, making the exercise even more stringent. The end result is that the fiducial scale cuts used for Y3 cosmic shear (both in this work and in [72]) are more conservative than strictly necessary for the baseline cosmic shear-only ΛCDM analysis. For this reason we repeat a subset of our analyses with an alternative set of relaxed scale cuts, designed to maximize the constraining power in cosmic shear and $3 \times 2\text{pt}$ ΛCDM alone (referred to as the "ΛCDM optimized" analysis, disregarding $2 \times 2\text{pt}$-alone and wCDM). These optimized cuts increase the total number of data points from 227 to 273 (184 ξ_+ and 89 ξ_-). We discuss the improvement in constraining power that comes from this choice in Sec. VI. While the gain in angular scales is not uniform across redshift bins, the minimum scale is reduced by a factor of 20–70% for different bin pairs. We show the ΛCDM optimized scale cuts as darker grey bands on Fig. 5 (compared to the lighter grey bands which correspond to the fiducial scale cuts and eliminate more data points on small scales).

H. Choice of priors

The priors on cosmological and nuisance parameters are summarized in Table I. Our choice of cosmological priors is relatively conservative, in order to ensure that the posterior distributions can span any point in parameter space we believe to be reasonable. Although the argument can be made for imposing more informative priors on our less well constrained parameters (primarily Ω_{b} and h) based on external data (e.g. Planck), we choose not to do so here. The main reasoning here is that we want to maintain the statistical independence of the DES Y3 cosmic shear data, to avoid double-counting information when combining our results with external datasets.

In contrast, we *do* impose informative priors on the measurement systematics (i.e. shear bias and photo-z error), which are derived from image simulations [77,78] and tests using BUZZARD [55,79]. More details on how these priors were chosen, and the dominant uncertainties can be found in those papers. It is worth bearing in mind that, while cosmic shear has only limited potential to self-calibrate photo-z errors [153], the combination with galaxy clustering and galaxy-galaxy lensing breaks parameter degeneracies; in the current study we are prior dominated in these systematics parameters, but in the $3 \times 2\text{pt}$ case this is significantly less true [73].
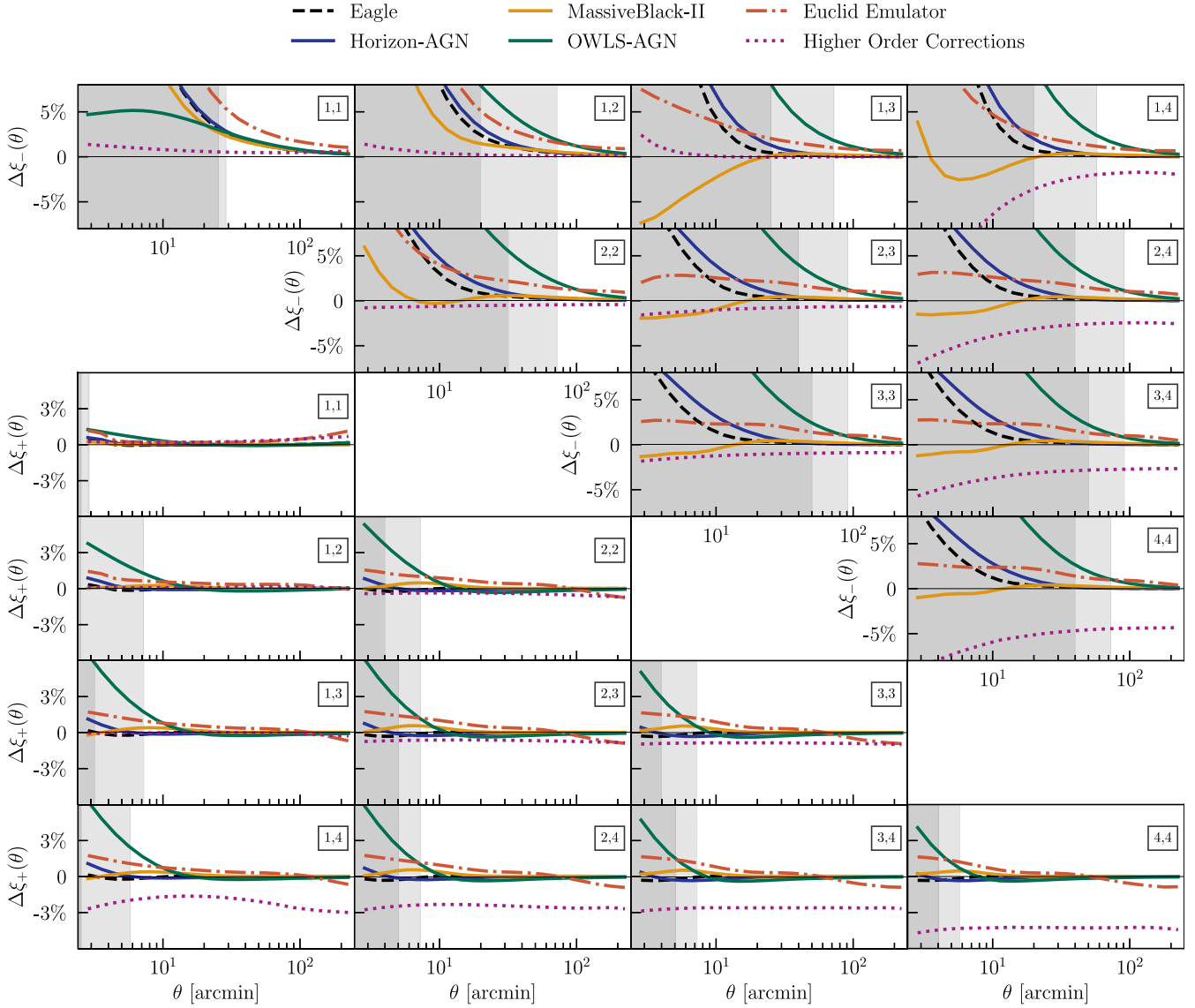
FIG. 5.   The theoretical contribution of different modeling systematics to $\xi_\pm$; for each systematic we show the fractional impact, relative to the fiducial case $\Delta\xi_\pm \equiv (\xi_\pm - \xi_\pm^{\rm syst})/\xi_\pm$. Fiducial scale cuts are shown as light shaded bands and are derived jointly for cosmic shear, 2×2pt and 3×2pt. Darker bands correspond to (less stringent) scale cuts that are optimized for cosmic shear and 3×2pt in ΛCDM only. Error bars on $\xi_{+(-)}$ are, at their smallest, around 15% (20%) of the signal, so the maximum contamination shown here $\mathcal{O}(1$–$5\%)$ is still significantly below the sensitivity of our data. We also find that none of these forms of contamination project translate into a bias in cosmological parameters at Y3 precision, despite appearing coherent in some redshift bins. Eagle (black dashed), Horizon-AGN (solid blue), MassiveBlack-II (solid yellow), and OWLS-AGN (solid green) represent scenarios for baryonic physics, and obtained from the power spectra of hydrodynamic simulations, while Euclid Emulator (dot-dashed red) modifies the nonlinear gravity-only power spectrum. Higher order corrections (dashed purple) is the theoretical impact of reduced shear and source magnification.

We choose uninformative priors on all of the five IA parameters, motivated by the relative lack of constraints reported in the literature for the TATT model (with the exception of [136]). Since IAs are highly sensitive to the composition of the galaxy population, as well as physical characteristics like redshift and luminosity, deriving appropriate priors is a complicated matter. We consider whether these IA parameters are detected by the data in Sec. VI C.

It is finally worth remarking that marginalizing posterior distributions from a high-dimensional parameter space down to 1D is prone to projection effects that can significantly displace the full-dimensional best-fit from the mean (or peak) of the 1D parameter distributions. The magnitude of these effects can be nontrivially affected by the choice of priors, particularly on the parameters that are not well constrained by cosmic shear data alone. We again refer the reader to Krause *et al.* [89], where tests

TABLE I. A summary of the priors used in the fiducial Y3 analysis. The top seven rows are cosmological parameters, while those in the lower sections are nuisance parameters corresponding to astrophysics and data calibration. We fix $w = -1$ when analyzing ΛCDM. Priors are either uniform (U) or normally distributed, $\mathcal{N}(\mu, \sigma)$.

Parameter	Prior
Cosmological parameters	
Ω_{m}	U[0.1, 0.9]
A_{s}	U[0.5, 5.0] $\times 10^{-9}$
Ω_{b}	U[0.03, 0.07]
n_{s}	U[0.87, 1.07]
h	U[0.55, 0.91]
$\Omega_\nu h^2$	U[0.6, 6.44] $\times 10^{-3}$
w	U[−2, −0.333]
Calibration parameters	
m_1	$\mathcal{N}(-0.0063, 0.0091)$
m_2	$\mathcal{N}(-0.0198, 0.0078)$
m_3	$\mathcal{N}(-0.0241, 0.0076)$
m_4	$\mathcal{N}(-0.0369, 0.0076)$
Δz_1	$\mathcal{N}(0.0, 0.018)$
Δz_2	$\mathcal{N}(0.0, 0.015)$
Δz_3	$\mathcal{N}(0.0, 0.011)$
Δz_4	$\mathcal{N}(0.0, 0.017)$
Intrinsic alignment parameters	
a_1	U[−5, 5]
a_2	U[−5, 5]
η_1	U[−5, 5]
η_2	U[−5, 5]
b_{TA}	U[0, 2]
Shear ratio parameters	
$\Delta z_1^{\mathrm{lens}}$	$\mathcal{N}(-0.009, 0.007)$
$\Delta z_2^{\mathrm{lens}}$	$\mathcal{N}(-0.035, 0.011)$
$\Delta z_3^{\mathrm{lens}}$	$\mathcal{N}(-0.005, 0.006)$
$\delta_{z,1}^{\mathrm{lens}}$	$\mathcal{N}(0.975, 0.062)$
$\delta_{z,2}^{\mathrm{lens}}$	$\mathcal{N}(1.306, 0.093)$
$\delta_{z,3}^{\mathrm{lens}}$	$\mathcal{N}(0.870, 0.054)$
b_g^{1-3}	U[0.8, 3]

of these effects using the priors given in Table I can be found.

V. MODEL ROBUSTNESS TESTS ON SYNTHETIC DATA

We now test the assumptions of the model set out in the previous section using contaminated mock data. The idea is that we generate data with astrophysical effects that are *not contained* in the model, and seek to quantify the level of bias they can cause to parameters of interest. These tests fall into two different categories, both involving synthetically generated $\xi_\pm$: noiseless analytic data (which is produced using the theory pipeline), and simulated data (measured using mock catalogs from N-body simulations).

Chronologically, all of the tests described in this section were performed *before unblinding*.

A. Analytically generated data

We analyze these data with the fiducial model, priors and analysis choices (including scale cuts), to verify that the inferred cosmological constraints are biased by less than 0.3σ in the $S_8 \times \Omega_{\mathrm{m}}$ plane. Figure 5 shows the systematic contributions to the contaminated data vectors for a number of the tests described below.

1. Nonlinear matter power spectrum

By construction, the scale cuts defined in Sec. IV G are conservative and mitigate most of the impact of small-scale modeling uncertainties in the 3-dimensional gravity-only matter power spectrum. To show that these uncertainties are negligible, we generate a synthetic cosmic shear data vector using the gravity-only Euclid Emulator [121]. Though it can be used at a relatively restricted range of cosmologies, the emulator is the most accurate method for estimating the nonlinear $P_\delta(k)$ currently available to the community. The deviation between this data vector and the fiducial prediction is shown in Fig. 5 (dot-dashed red), and is at most ~1 percent on the scales included in our analysis. We verify that the bias in cosmological parameters when analyzing these mock data with the fiducial ΛCDM model is below 0.3σ [89].

In addition to the test of the nonlinear growth model, we also generate synthetic data vectors using matter power spectra derived from the Horizon-AGN, Eagle, and MassiveBlack-II hydrodynamic simulations (Fig. 5, [150,154,155]). The P_δ obtained from these simulations contain the imprint of baryonic feedback processes. Although these effects are notoriously difficult to model, the simulations are useful as a measure of the range of uncertainty in the baryonic contributions. That is, if we can demonstrate insensitivity to a range of (at least semi-) realistic scenarios, then that offers some reassurance that our cosmological results are unaffected. We confirm that the resulting biases are significantly smaller than 0.3σ [89]. At some level this result is expected, since our fiducial scale cuts are constructed based on the OWLS-AGN model, which is a relatively extreme feedback scenario. It does, however, demonstrate that our scale cut prescription is generally conservative, and is not fine-tuned to the specific redshift or scale dependence of OWLS-AGN.

2. Higher-order shear contributions

We also verify that the effects of reduced shear, source sample magnification and source clustering do not affect the cosmic shear constraints significantly. These generally enter as higher-order corrections. For the case of reduced shear and source magnification, the correction to the convergence angular power spectrum has the form [156–158]:

$$\Delta C_\kappa^{ij}(\ell) = 2(1 + C_s^i) \int \frac{d^2 \ell_1}{(2\pi)^2} \cos 2\phi_{\ell_1} B_\kappa^{ij}(\vec{\ell}_1, \vec{\ell} - \vec{\ell}_1, -\vec{\ell}),$$

$$(30)$$

where B_κ^{ij} is the convergence bispectrum, C_s^i is a magnification coefficient related to the slopes of the flux and size distributions [157] and ϕ_{ℓ_1} is the angle between modes $\vec{\ell}$ and $\vec{\ell}_1$. We show in Fig. 5 this contribution to the shear power spectrum for the source magnification coefficients $C_s^{1...4} = (-1.17, -0.64, -0.55, 0.80)$ as measured by Elvin-Poole *et al.* [159] in each redshift bin. We note that the theoretical modeling of nonlinear scales in the matter bispectrum is a dominant source of uncertainty in the calculated correction (see for instance [160]). In particular, we utilize the nonlinear (HaloFit) power spectrum in the tree-level bispectrum description, but future analyses will possibly benefit from improved approaches, such as BiHaloFit [161]. Still, the largest potential biases as seen in Fig. 5 are $< 5\%$, smaller than our error bars ($\gtrsim 15\%$). We also find, like Prat *et al.* [162] demonstrate for galaxy-galaxy lensing, that the reduced shear contribution to cosmic shear as computed perturbatively overestimates the impact of that correction when compared to measurements of reduced shear on BUZZARD simulations. The leading sources of higher-order corrections and their contribution for DES Y3 are computed in more detail in Krause *et al.* [89]. Their results confirm that these effects are negligible in terms of parameter constraints, and provide a guide for future DES and next generation analyses.

3. Intrinsic alignments

Prior to unblinding of the real data, we carried out a series of tests designed to verify the robustness and sufficiency of our fiducial choice of intrinsic alignment model. Our expectation is to find, using synthetic data, a set of model choices that prevent biases coming from an incorrect characterization of IA. To this end, we generate two simulated data vectors: one including full TATT contributions with input parameters given by the mean posterior IA constraints from the Y1 3×2pt analysis of [136] ($a_1 = 0.7$, $a_2 = -1.36$, $\eta_1 = -1.7$, $\eta_2 = -2.5$, $b_{TA} = 1$), and an another with the NLA subset of those parameters ($a_1 = 0.7$, $\eta_1 = -1.7$, $a_2 = 0$, $b_{TA} = 0$). Our results can be summarized as:

(i) Fitting the NLA data vector with either the NLA or TATT model results in no significant biases. Projection effects in the 1D S_8 posterior are negligible in both cases. The more complex model weakens the constraint by increasing the S_8 error bar by 14%. See Appendix C for a discussion of this on real data, where we find a somewhat similar loss in constraining power.
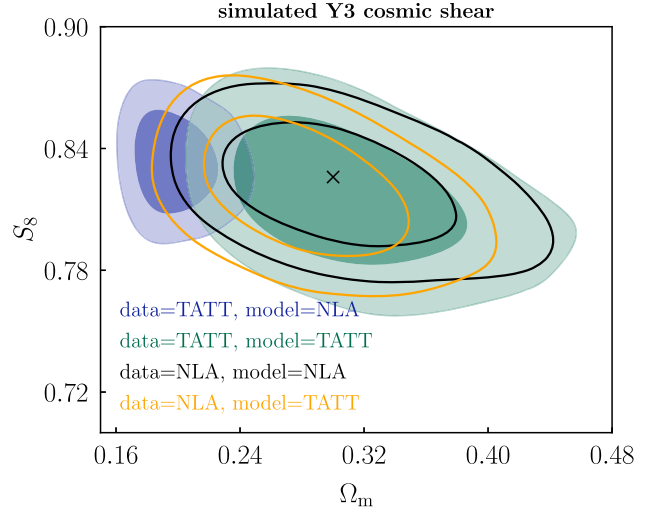

FIG. 6.   Posteriors from the analysis of *synthetic data vectors with differing input IA signals*, with a known input cosmology (black cross). Strikingly, if IAs in DES Y3 are present at the level of those in the synthetic TATT data vector (chosen to match the DES Y1 result of [136]), the NLA model is not sufficient to recover the true cosmology (blue contours). We explore whether this scenario is actually reproduced in real data in Sec. VI C 2. All other model/data combinations recover the input cosmology to within significantly less than 1σ.

(ii) Likewise, and as expected, fitting the TATT data vector using TATT recovers the input cosmology and IA parameters.

(iii) Fitting the TATT data vector with the simpler NLA model results in significant residual bias in σ_8, S_8, and Ω_m. We also see artificially tightened constraints in this case, as the posteriors on some parameters begin to hit the prior edges, and a significantly degraded best-fit χ^2.

The findings above are summarized in Fig. 6, and a more detailed discussion of these tests, and what they reveal about the systematic error budget, can be found in Appendices B and C. The configuration which presented significant biases (NLA modeling of TATT synthetic data) should be considered as a sufficiency test of the simpler IA model, which NLA *fails to meet at the synthetic data level*. This means that, given our expectation from the DES Y1 results of Samuroff *et al.* [136], and given our deliberate choice of relying solely on synthetically generated data to make a model selection at the blinded analysis stage, our findings provide a strong argument for adopting TATT as our fiducial choice. In summary, previous results on DES Y1 data do not allow us to rule out alignments at the level present in the simulated TATT data vector used in these tests, and we thus choose TATT as our fiducial model. We explore in Sec. VI C 2 whether this pre-unblinding expectation of the inadequacy of NLA to fit our data is actually realized and what level of IA complexity our data seems to point to. Foreshadowing that discussion, post-unblinding

we find NLA to be compatible with DES Y3 data, and that our results for S_8 are robust to the choice of the IA model.

Our fiducial setup makes the explicit assumption that the redshift evolution of IAs in DES Y3 can be adequately described by a power law [Eqs. (24) and (25)]. To test this particular analysis choice, we produce synthetic data using the recipe set out in ([66]; see their Sec. IVA). In brief, we assume a particular luminosity scaling for the linear alignment strength β_1, which is combined with a measured luminosity function from the Deep Extragalactic Evolutionary Probe2 (DEEP2; [163]) spectroscopic survey, and the measured red fraction $f_{\rm red}(z)$, to predict an IA signal with a nontrivial redshift dependence. Both the redshift and luminosity evolution of red and red + blue galaxies are thus extrapolated (not measured) down to the limiting magnitude over the redshift range of the DES sample. Our baseline is to use the best fitting β_1 from Joachimi et al. [164] and assume zero alignments in blue galaxies. Note that while constraints on the luminosity dependence of the a_2 component of the TATT model do exist in the literature, they are still relatively weak, and consistent with $\beta_2 = 0$; for this reason, we restrict ourselves to the NLA case. The results are described in more detail in Krause et al. [89], which also includes similar tests in the context of 2 × 2pt and 3 × 2pt analyses. With our fiducial input parameters, we find biases of up to 0.5σ. Although larger than our 0.3σ passing requirement, it is worth bearing in mind that this test relies on a number of assumptions and extrapolations and is quite possibly unrealistically stringent. Given this, and in the absence of a stronger test, we maintain our fiducial model and decide to test for the redshift scaling of the a_1 parameter a posteriori, after unblinding, in Sec. VII.

Finally, we assess whether the interaction between erroneous calibration of photo-zs and their uncertainties and our IA model can lead to biased estimates of cosmology. A rationale for this test is that photo-z mischaracterization can produce amplitude shifts in cosmic shear correlations. These shifts can potentially be degenerate with IA model parameters, and bias their posterior distributions, which in turn can lead to biases in cosmology as discussed, e.g. by Wright et al. [58]. Another example is when $n(z)$ distribution tails are underestimated in the data, leading to an erroneous assumption of small overlap between redshift bins and consequently a suppressed II contribution, which is more sensitive to this overlap than the lensing signal is (see also Appendix C of [130]).

We seek to test our robustness to such redshift-IA interactions by reanalyzing the synthetic TATT data vector described above repeatedly using alternative (incorrect) redshift distributions in the modeling. For this test, we use the fiducial analysis setup including redshift error as parametrized by free Δz shift parameters. Rather than introducing analytic distortions to the fiducial $n(z)$, we draw alternative realizations from the ensemble generated

by the SOMPZ pipeline [79]. This should naturally capture plausible cases of redshift error, beyond what can be captured by a simple shift in the mean z. We select three redshift realizations representative of a range of cases in terms of the change in the predicted data vector ($\Delta\chi^2$). The results are shown in more detail in Appendix B, but in brief we find only small ($< 0.3\sigma$) shifts in S_8 in the different scenarios. Even in the most extreme case, where $\Delta\chi^2 \sim 14$, the input IA parameters and cosmology are accurately constrained. In summary, at the level of synthetically generated data with plausible fluctuations in $n(z)$, we do not see evidence that the relatively flexible IA model is absorbing redshift error to a degree that could bias cosmology or IA parameters.

B. Mock data from N-body simulations

While most model tests are performed using noiseless analytic data vectors, a subset of tests make use of mock catalogs from N-body simulations. We employ two sets of simulations: BUZZARD [165] and the MICE-Grand Challenge Galaxy and Halo Light-cone catalog[13] [166]. With BUZZARD, a thorough testing of the DES Y3 measurement, photo–z and likelihood pipelines is performed not only for cosmic shear but also for the other DES 3 × 2pt probes [88]. With MICE, we focus specifically on testing the IA model.

1. BUZZARD v2.0

The BUZZARD v2.0 simulations (BUZZARD hereafter) are a suite of 18 simulated galaxy catalogs built on N-body lightcone simulations [165,167,168]. The N-body simulations are produced using the L-Gadget2 N-body code, a memory optimized version of Gadget2 [169]. The initial conditions for the simulations are generated at $z = 50$ using 2LPTIC and linear power spectra computed by CAMB at the BUZZARD flat ΛCDM cosmology: $(\sigma_8, n_s, h, \Omega_m, \Omega_b) = (0.82, 0.96, 0.7, 0.286, 0.046)$. Each simulation is run on three different and independent boxes with sizes $(1.0, 2.6$ and $4.0)^3$ $h^{-3}\,{\rm Gpc}^3$ containing $(1400, 2048, $ and $2048)^3$ particles respectively, and a lightcone with footprint area over $10,000\,{\rm deg}^2$ is produced from each of the sets. Galaxies are included in these lightcones with properties such as position, ellipticity and spectral energy distribution using the ADDGALS algorithm, with details specified in [168].

Weak lensing quantities are introduced via ray-tracing [170], and the complete 3 × 2pt cosmology analysis of DES Y3 is reproduced in these simulations [88]. For the validation of cosmic shear, BUZZARD provides a way to verify that several astrophysical effects ignored in our modeling are, as expected, sub-dominant. In addition to higher order corrections from reduced shear and source

---

[13]https://cosmohub.pic.es/home.

sample magnification which are also examined in this paper, BUZZARD mocks contain source galaxy clustering, anisotropic redshift distributions across the survey area and multiple-plane lensing deflections. We point the reader to DeRose *et al.* [88] for more details.

2. Intrinsic alignments testing with MICE

The MICE Grand Challenge run is an N–body gravity-only simulation with 4096^3 collisionless particles with masses $2.927h^{-1} M_\odot$ in a $3072 \, h^{-1}$ Mpc box using a flat ΛCDM cosmology with $(\sigma_8, n_s, h, \Omega_m, \Omega_b) = (0.8, 0.95, 0.7, 0.25, 0.044)$. Dark matter halos are identified as friends-of-friends groups and populated with synthetic galaxies using a hybrid method of halo occupation distribution modeling and abundance matching [166,171–174].

Although MICE does not account for baryonic feedback and other hydrodynamic processes related to galaxy formation and evolution, an intrinsic galaxy alignment signal is implemented in the mock using a semianalytic technique (Appendix A; see [175] for a detailed overview). In brief, shapes and orientations are assigned to galaxies based on a combination of their color and luminosity, and the spin and orientation of the host halos. The model is conceptually similar to those of Okumura *et al.* [176] and Joachimi *et al.* [177,178], and has been tuned to match the distribution of galaxy axis ratios from COSMOS observations [179,180] in bins of redshift, stellar mass and color. Various diagnostic tests have been carried out, and it has been shown to reproduce the projected intrinsic galaxy-shape correlation w_{g+} of luminous red galaxies in the spectroscopic BOSS LOWZ sample [181] as a function of luminosity [175].

The MICE IA mock is particularly valuable for our purposes, since it provides an alternative IA prediction with its own redshift dependence, which does not assume either NLA or TATT. At the time of writing, however, only a single realization of the IA mock is available, and we thus we cannot apply the more stringent criteria of DeRose *et al.* [88] for validating the DES Y3 pipeline on simulations. For this reason, passing the tests presented in this subsection was not an unblinding prerequisite.

We describe in Appendix A how a source sample is created with the MICE mock which reproduces basic DES Y3 specifications. The measurement of cosmic shear correlation functions $\xi_\pm$ is made using TreeCorr in a similar way to on the real Y3 data. Since the MICE catalog contains the gravitational shears $\gamma_{1,2}$ (G) and the intrinsic shapes $\epsilon_{1,2}$ (I), we can estimate the GG, GI, and II components separately if desired. We thus measure two data vectors: a version which contains the GG signal only (the "baseline") and another version in which G + I shears are summed together ([182]; Eq. 3.2). In this second case, the two-point correlations correspond to GG + GI + II (a "contaminated" data vector including the noisy IA signal).

With the shape noise and effective number density of MICE galaxies per redshift bin determined in Appendix A, we construct an analytic covariance using CosmoLike [105], but rescale the shape noise terms so that the figure-of-merit of the fiducial model constraints in the $S_8 \times \Omega_m$ plane is similar to that of the other simulated cosmic shear tests. We employ the fiducial scale cuts and nuisance parameters.

With the same likelihood pipeline used in other tests, we find that the bias (distance between posterior peaks) in the $S_8 \times \Omega_m$ plane between the baseline and contaminated data vectors is 0.6σ for the fiducial (TATT) IA model. A similar run, but using NLA as the model, results in a 0.3σ bias between baseline and contaminated data. Since the more flexible TATT model should, in principle, be able to capture any IA scenario that NLA can, we ascribe this difference to competing shifts due to the statistical fluctuations and the simpler IA model, which partially cancel. Furthermore, the posteriors from a_1 and η_1 coming from the two models are fully consistent.

One important caveat here is that we have only a single noise realization; the size of the biases quoted for NLA and TATT therefore cannot be decoupled from fluctuations due to shape noise and cosmic variance. This point complicates the interpretation of our results. That said, there is a qualitative difference between the MICE + IA simulated data vectors and the other synthetic $\xi_\pm$ vectors: while all other data are analytically generated using either the NLA or TATT model, the MICE data are agnostic with respect to the analytic model and are tuned to fit observed IA signals (albeit at significantly lower redshifts). It is, then, reassuring that we obtain reasonable IA constraints, and the cosmological parameters S_8 and Ω_m are not catastrophically biased. Analysis of a greater number of MICE + IA mocks, in order to disentangle IAs from noise and cosmic variance, is an interesting extension left for future work, but beyond the scope of this paper.

VI. PARAMETER CONSTRAINTS

In this section we present the baseline cosmic shear constraints from DES Y3. Section VI A presents our main results in ΛCDM, Sec. VI B shows we find no detection of the dark energy equation of state parameter w, and Sec. VI C 2 presents a detailed comparison of the evidence for different IA models. A series of extended models, including parametrized deviations from general relativity, and additional neutrino species, will be discussed in [74], which is in preparation. A number of external datasets are introduced in this section, details of which can be found in Sec. VIII A. For a summary of our fiducial results, and of the robustness tests discussed in the next section, see Table II and Fig. 10. To facilitate comparison of constraining power, we also show the 2D S_8–Ω_m figure of merit (FoM), which is defined as FoM $\equiv \det\{\mathbf{C}_{S_8,\Omega_m}\}^{-1/2}$,

TABLE II. A summary of cosmological constraints from DES Y3 cosmic shear. In each case in the top 9 rows, we show the posterior mean and 68% confidence bounds on each S_8 and Ω_m, as well as the maximum posterior S_8 value (denoted $\hat{S}_8$), the 2D S_8–Ω_m figure of merit and the goodness-of-fit. These top rows also include, as a default, the shear ratio likelihood. A visual summary of the S_8 constraints can be seen in Fig. 10. Constraints from KiDS-1000 and HSC are as nominally reported and were not reprocessed under the DES Y3 priors and analysis choices, while Planck 2018 numbers have been obtained under DES Y3 cosmology priors.

	S_8	$\hat{S}_8$	σ_8	Ω_m	$\mathrm{FoM}_{S_8\Omega_\mathrm{m}}$	χ^2/dof
Fiducial ΛCDM	$0.759^{+0.023}_{-0.025}$	0.755	$0.783^{+0.073}_{-0.092}$	$0.290^{+0.039}_{-0.063}$	927	$237.7/222 = 1.07$
ΛCDM -Optimized	$0.772^{+0.018}_{-0.017}$	0.774	$0.795^{+0.072}_{-0.076}$	$0.289^{+0.036}_{-0.056}$	1362	$285.0/268 = 1.06$
No IAs	$0.774^{+0.017}_{-0.018}$	0.760	$0.775^{+0.071}_{-0.077}$	$0.306^{+0.040}_{-0.061}$	1253	$243.3/225 = 1.08$
NLA	$0.773^{+0.020}_{-0.021}$	0.773	$0.791^{+0.070}_{-0.086}$	$0.293^{+0.039}_{-0.056}$	1163	$242.1/224 = 1.08$
NLA, free a_1 per z–bin	$0.790^{+0.022}_{-0.020}$	0.783	$0.834^{+0.075}_{-0.082}$	$0.275^{+0.035}_{-0.051}$	1144	$246.3/221 = 1.11$
$a_1 > 0$ prior	$0.755^{+0.022}_{-0.022}$	0.727	$0.731^{+0.064}_{-0.085}$	$0.327^{+0.046}_{-0.066}$	881	$238.7/222 = 1.07$
Fixed neutrino mass	$0.772^{+0.023}_{-0.023}$	0.748	$0.816^{+0.071}_{-0.094}$	$0.275^{+0.040}_{-0.052}$	1063	$238.3/222 = 1.07$
wCDM cosmology	$0.735^{+0.023}_{-0.041}$	0.699	$0.723^{+0.071}_{-0.100}$	$0.319^{+0.050}_{-0.071}$	497	$237.5/222 = 1.07$
HMcode power spectrum	$0.772^{+0.026}_{-0.027}$	0.791	$0.793^{+0.088}_{-0.102}$	$0.294^{+0.038}_{-0.070}$	827	$236.8/222 = 1.06$
NLA, ΛCDM -Optimized, fixed neutrino mass	$0.788^{+0.017}_{-0.016}$	0.775	$0.825^{+0.078}_{-0.79}$	$0.279^{+0.036}_{-0.053}$	1501	$288.1/270 = 1.07$
DES Y1	$0.780^{+0.027}_{-0.021}$	$\cdots$	$0.764^{+0.069}_{-0.072}$	$0.319^{+0.044}_{-0.062}$	625	$227/211 = 1.08$
KiDS-1000 COSEBIs	$0.759^{+0.024}_{-0.021}$	$\cdots$	$0.838^{+0.140}_{-0.141}$	$0.246^{+0.101}_{-0.060}$	650	$85.5/70.5 = 1.21$
HSC Y1 C_ℓ	$0.780^{+0.030}_{-0.033}$	$\cdots$	$\cdots$	$0.162^{+0.086}_{-0.044}$	461	$45.4/53 = 0.86$
HSC Y1 $\xi_\pm$	$0.804^{+0.032}_{-0.029}$	$\cdots$	$0.766^{+0.110}_{-0.093}$	$0.346^{+0.052}_{-0.100}$	402	$162.3/167 = 0.97$
Planck 2018 TT + TE + EE + lowE	$0.827^{+0.019}_{-0.017}$	$\cdots$	$0.793^{+0.024}_{-0.009}$	$0.327^{+0.008}_{-0.017}$	3938	$\cdots$

where $\mathbf{C}_{S_8,\Omega_\mathrm{m}}$ is a subblock of the parameter covariance matrix.

A. ΛCDM

The posteriors from our fiducial analysis are shown in Fig. 7, along with our ΛCDM optimized result (with scale cuts that maximize the constraining power in ΛCDM, see Sec. IV G; black dashed), alongside Planck 2018 TT + TE + EE + lowE (no lensing, [183]; yellow). As with almost all previous lensing analyses to date, DES Y3 favors a somewhat lower S_8, a pattern we discuss further in Sec. VIII B 2. The marginalized mean S_8 and Ω_m values in ΛCDM are
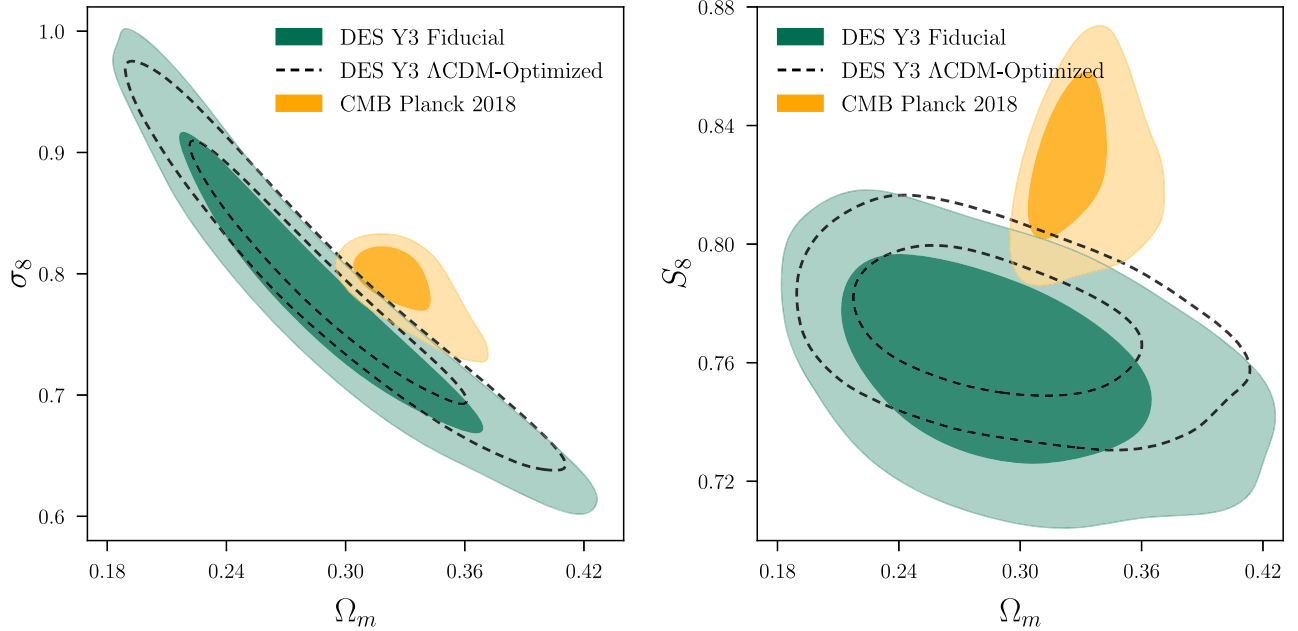

FIG. 7. The posteriors of DES Y3 cosmic shear (green) and Planck 2018 (TT + TE + EE + lowE no lensing; yellow). The shaded green contours are the results from our fiducial analysis, as described in Sec. IV, and constraints using scale cuts that are optimized for a ΛCDM -only analysis are shown in dashed lines. In each case we show both 68% and 95% confidence levels.

$$S_8 = 0.759^{+0.023}_{-0.025} \quad (0.755) \quad (\Lambda\text{CDM})$$

$$\Omega_m = 0.290^{+0.039}_{-0.063} \quad (0.293) \quad (\Lambda\text{CDM}),$$

where uncertainties are 68% confidence intervals. These 1D constraints represent our best estimate for the uncertainties within our analysis framework. It is worth bearing in mind, however, that comparison of constraining power between different lensing surveys is complicated by differences in the analysis choices and priors [184]. Our fiducial ΛCDM analysis has 222 effective degrees of freedom.[14] At the maximum posterior (MAP) point we obtain $\chi^2/\text{dof} = 237.7/222 = 1.07$, and a corresponding p–value of 0.22.

One important question arising from Fig. 7 is the extent to which the DES and Planck results are consistent with each other. Given that we are considering a complex 28 dimensional parameter space, assessing agreement purely using projected contours can be misleading (see [86] for discussion). We present a more rigorous quantitative discussion of possible tensions with external datasets in Sec. VIII B.

Different angular scales of the cosmic shear correlation function have slightly different sensitivities to cosmological parameters [20]. The degeneracy between σ_8 and Ω_m is such that the best constrained combination is $S_8 = \sigma_8(\Omega_m/0.3)^\alpha$ with $\alpha \approx 0.5$, but we can also determine the exponent α directly from the data. We carry out a principal component analysis of the projected ΛCDM posteriors to obtain the exponent value that most effectively decorrelates σ_8 and Ω_m. We find in our fiducial ΛCDM TATT analysis that $\alpha = 0.586$. To avoid confusion, we call the corresponding lensing amplitude Σ_8 and find:

$$\Sigma_8 \equiv \sigma_8(\Omega_m/0.3)^{0.586} = 0.756^{+0.021}_{-0.021} \quad (0.729) \quad (\Lambda\text{CDM}).$$

Also shown in Fig. 7 (black dashed) are the results of our optimized cosmic shear analysis. The details of, and justification for, this additional analysis can be found in Sec. IV G 3, but the key idea is to use a set of scale cuts that are tuned to maximise the constraining power of cosmic shear alone in ΛCDM. The result is a tighter constraint in the S_8–Ω_m plane in ΛCDM:

$$S_8 = 0.772^{+0.018}_{-0.017} \quad (0.774) \quad (\Lambda\text{CDM Optimized}).$$

As can be seen in Fig. 7, the gain in constraining power is asymmetric about the posterior peak, which has the effect of shifting the mean S_8 up slightly. We consider the impact

---

[14]We calculate the effective number of d.o.f. following Raveri and Hu [185], as the number of data points for $\xi_\pm$ after scale cuts (227) minus the number of effective parameters ($N_{\text{p,eff}} \approx 5$), given by $N_{\text{p,eff}} \equiv N_{\text{p,nom}} - \text{Tr}\{\mathbf{C}_\Pi^{-1}\mathbf{C}_p\}$, where $N_{\text{p,nom}}$ is the nominal number of free parameters and $\mathbf{C}_\Pi$, $\mathbf{C}_p$ are respectively the covariances of the prior and posterior. As $N_{\text{p,eff}}$ can change with different modeling choices, we recompute it whenever necessary.

of this in terms of statistical consistency in Sec. VIII B. The extra data points increase the number of effective degrees of freedom to 268, giving a goodness-of-fit at the maximum posterior of $\chi^2/\text{dof} = 285.0/268 = 1.06$, with a p-value of 0.22, similar to the fiducial analysis.

B. *w*CDM

A simple extension to ΛCDM is to free the dark energy equation-of-state parameter (previously fixed to $w = -1$). The prior bounds on w in Table I are chosen such that cosmic acceleration is ensured by $w < -1/3$, and "phantom" models with $-2 < w < -1$ are allowed. To assess the statistical preference of our data for this extended model, we evaluate the evidence ratio (see Sec. IV A) between ΛCDM and wCDM and find

$$R_{w/\Lambda} = 0.94 \pm 0.22,$$

which, based on the Jeffreys scale, is inconclusive in terms of preference for the model with free w. We thus find no evidence for (or against) a departure from ΛCDM using DES Y3 cosmic shear data alone.

While w is unconstrained by cosmic shear data within our priors, we can still constrain S_8 in that parameter space, and we show its marginalized value in Fig. 10. We find a shift toward lower lensing amplitude, qualitatively implying that this model extension would not help to provide a solution to the differences with respect to Planck.

C. Intrinsic alignments

In addition to the main cosmological results, it is also interesting to consider what our data can tell us about IAs. Since we see no evidence that redshift error is biasing our IA results (see Appendix B), the IA parameters have a physical interpretation, and are potentially useful for future lensing analyses. For details about how changes in the IA model can affect the inferred cosmology see Sec. VII B.

1. IA model constraints

In Fig. 8 we show the IA posteriors in both TATT and NLA, as well as in the optimized ΛCDM analysis and NLA with a fixed redshift evolution parameter (for the numerical values, see Table III). Note that there are additional parameters in the full model (redshift indices and b_{TA}), which are only weakly constrained and so are not shown here (see Appendix D for the full posterior). In all model scenarios, the data favor a smaller IA signal than DES Y1, although the values are consistent within the uncertainties (see Fig. 12 in [136]), resulting in a total GI + II contribution that is only at the level of a few percent of the cosmological signal (as shown in Fig. 2). In the fiducial TATT case, the data favor mildly negative a_1, combined with $a_2 > 0$:
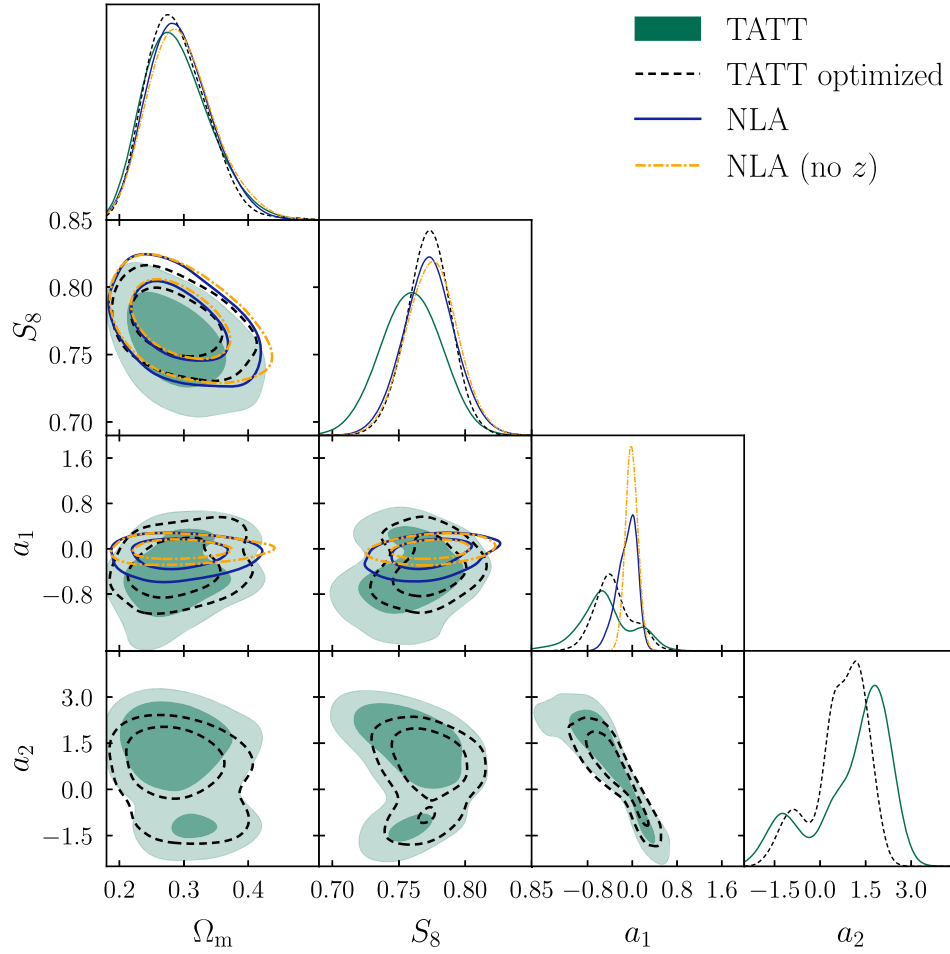
FIG. 8.   Posterior parameter constraints from the fiducial ΛCDM cosmic shear analysis (TATT, green), which includes shear ratios as a fiducial choice. The solid blue (NLA) and dot-dashed yellow (NLA without redshift evolution) contours show the results of the same cosmic shear analysis, but using alternative (simpler) IA models. We also include our ΛCDM optimized TATT result (dashed black). As before, both 68% and 95% confidence levels are shown. We find that different IA models lead to consistent results and similar goodness-of-fit (see Table III), and the main difference between them is the change in constraining power.

$$a_1 = -0.47^{+0.30}_{-0.52} \quad (-0.73) \quad (\text{TATT } \Lambda\text{CDM})$$
$$a_2 = 1.02^{+1.61}_{-0.55} \quad (1.88) \quad (\text{TATT } \Lambda\text{CDM}).$$

We observe asymmetric error bars in the posteriors of a_1 and a_2 and also find slight evidence for a secondary peak with reversed signs of the parameters. This hint of bimodality in the IA subspace can be readily understood within our model: contributions to power spectra in Eqs. (21)–(23) that scale as a_1^2, a_2^2 or $a_1 a_2$ are insensitive to positive/negative sign flips. This degeneracy is further enabled in our present regime, where IA signals are small compared to the measurement errors, and terms proportional to a_1 and a_2 partially cancel each other when they have opposite signs. We also note that the secondary peak is less pronounced in the optimized analysis shown in Fig. 8, and Amon *et al.* [72] shows that the addition of the shear ratios data in our fiducial constraints has already contributed to suppressing the bimodal feature. We thus interpret

this doubly peaked posterior as an internal degeneracy of the model that is broken as statistical power increases. Note that forcing a prior such that $a_1 > 0$, eliminating one of the peaks, also leads to essentially unchanged cosmology results (see below and in Sec. VII B).

It is worth bearing in mind that the $a_1 = a_2 = 0$ point lies within the bounds of the 2D 1σ contour, and it is plausible that the negative best-fit a_1 is simply the result of a small true IA amplitude and noise (see also Appendix A). We also confirm that rerunning our fiducial analysis with a prior that forces $a_1 > 0$ (in line with expectation from observations of red galaxies and the theory of tidal alignment) shifts the IA constraints, and results in a negative a_2, as consistent with our Y1 results, but does not appreciably alter the confidence contours in the S_8–Ω_m plane. If we restrict ourselves to the simpler (two-parameter) NLA model, the data still favor negative a_1, although at lower significance ($a_1 = -0.09^{+0.20}_{-0.13}$). Again, this is lower than the Y1 results, both from cosmic shear alone and in combination

TABLE III. Marginalized constraints on IA parameters, best-fit χ^2 and evidence ratio R metrics for IA models of increasing complexity on $\xi_\pm(\theta)$ without including the shear ratio likelihood. In each row, the evidence ratios assume TATT and the model in the row above are in the denominator (so $R > 1$ implies preference for the model defined in the corresponding row). Marginalized constraints are defined here as the mean of posteriors and their 68% uncertainties. Empty values in the table correspond to parameters that are fixed to zero.

IA model (free parameters)	χ^2/d.o.f.	Log evidence	R (w.r.t. TATT)	R (w.r.t. above)	a_1	η_1	a_2	η_2	b_{TA}
No IAs	240.6/225	3215.79 ± 0.11	9.48 ± 1.66	N/A	$\cdots$	$\cdots$	$\cdots$	$\cdots$	$\cdots$
NLA no z-evo. (a_1)	238.6/224	3213.89 ± 0.12	1.42 ± 0.30	0.15 ± 0.03	$0.34^{+0.25}_{-0.23}$	$\cdots$	$\cdots$	$\cdots$	$\cdots$
NLA (a_1,η_1)	238.3/224	3214.07 ± 0.13	1.70 ± 0.36	1.19 ± 0.24	$0.36^{+0.43}_{-0.36}$	$1.66^{+3.26}_{-1.05}$	$\cdots$	$\cdots$	$\cdots$
TA (a_1,η_1,b_{TA})	238.8/224	3213.87 ± 0.13	1.38 ± 0.25	0.81 ± 0.14	$0.27^{+0.35}_{-0.31}$	$2.10^{+2.89}_{-0.71}$	$\cdots$	$\cdots$	$0.83^{+0.31}_{-0.82}$
No z-evo. (a_1,a_2,b_{TA})	238.6/223	3211.81 ± 0.14	0.17 ± 0.03	0.12 ± 0.02	$0.18^{+0.21}_{-0.30}$	$\cdots$	$0.10^{+0.55}_{-0.57}$	$\cdots$	$0.80^{+0.29}_{-0.78}$
No a_2 z-evo. (a_1,η_1,a_2,b_{TA})	238.2/223	3212.09 ± 0.14	0.23 ± 0.04	1.32 ± 0.26	$-0.02^{+0.71}_{-0.31}$	$2.17^{+2.82}_{-0.70}$	$-0.27^{+0.59}_{-0.50}$	$\cdots$	$0.87^{+0.38}_{-0.83}$
TATT ($a_1,\eta_1,a_2,\eta_2,b_{TA}$)	233.1/222	3213.54 ± 0.13	1	4.28 ± 0.83	$-0.24^{+0.98}_{-0.41}$	$2.38^{+2.62}_{-0.61}$	$0.63^{+1.93}_{-1.89}$	$3.11^{+1.77}_{-0.31}$	$0.87^{+0.38}_{-0.84}$

with galaxy–galaxy lensing and galaxy clustering ($a_1^{3\times2pt} = 0.49^{+0.15}_{-0.15}$, $a_1^{1\times2pt} = 1.03^{+0.45}_{-0.57}$; see [186] and Table 5 in [136]). The impact of the optimized ΛCDM analysis, which includes extra small-scale information, is to tighten the contours in the a_1–a_2 plane (compare the shaded green and black dashed lines in Fig. 8), and it does not qualitatively change our conclusions here.

One detail worth noting is that all of the posteriors presented in this paper include a contribution from shear ratios. The small-scale ($\sim$2–6 Mpc/h) galaxy–galaxy lensing information significantly improves our ability to constrain IAs (see Fig. 10 of [81]). That said, it has been demonstrated that the use of γ_t on large (instead of small) scales for the SR likelihood does not substantially change the favored IA scenario [81]. It has also been shown that removing the SR likelihood altogether results in consistent, though broader, constraints in the a_1–a_2 plane [72].

We illustrate the redshift dependence of the inferred IA signal in Fig. 9, which can be compared to the analogous version from DES Y1 in Fig. 16 of Troxel *et al.* [7], and also to Fig. 7 of Dark Energy Survey Collaboration [73]. In IA models where we use a parametric redshift dependence (TATT and NLA), one can derive effective amplitudes for each redshift bin j as $a_i^j = a_i(1 + \bar{z}_j/1 + z_0)^{\eta_i}$, where $i \in (1, 2)$. The points and error bars in Fig. 9 are the mean and marginalized 68% confidence contours of these derived parameters. In all cases the tidal alignment amplitude a_1 is consistent between models to $\sim$1σ.
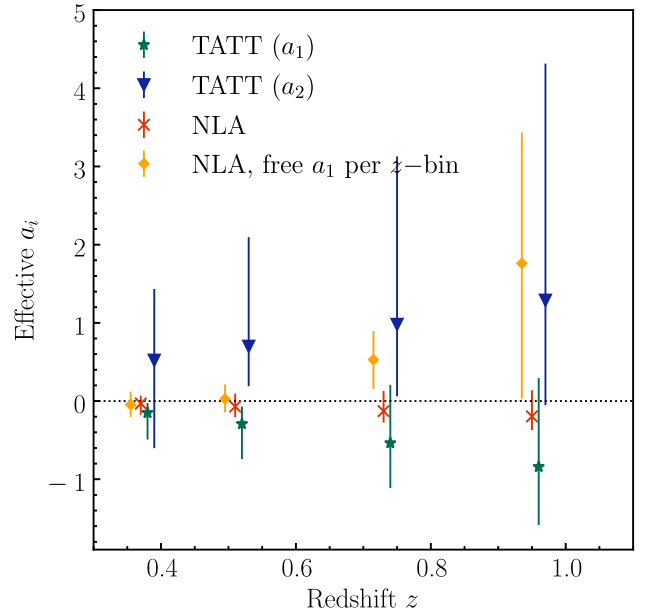

FIG. 9. Effective IA amplitudes $a_{1,2}$ as a function of redshift. Note that the green and blue points (both labelled TATT) are the product of the same analysis, in which a_1 and a_2 were varied simultaneously. We report no clear evidence for redshift evolution in a_1, and relatively good agreement between models.

2. IA model selection

In addition to the basic results using variations of NLA and TATT in the IA implementation, we also perform a more rigorous model comparison in order to determine which IA model preferred by the data in a statistical sense. We explain this concept in more detail below.

First, we rank order models that are subspaces of TATT by their complexity and step up that list one at a time, usually by including a new parameter. At each step i, we rerun a chain to obtain the best-fit χ^2 and evidence of the model. We then compute the evidence ratios (see Sec. IV A) between the models at step i and $i-1$, and between the model at step i and the fiducial TATT model. In doing this, we are in principle able to determine at which point in the complexity "ladder" our data stops justifying the addition of extra IA parameters.

The order of the model complexity we use is not rigorously defined, but it follows the logic of the perturbative modeling approach. The simplest possible case is a model with no IA. We then consider tidal alignment (TA) less complex than models with tidal torquing (TT), and within these categories, models without redshift dependence are less complex. Thus, the simplest IA model under consideration has a_1 free and all else held fixed, followed by a_1 with a free power-law parameter for redshift evolution, η_1, and so on up to the (fiducial) 5-parameter TATT (see Table III).

In order to minimize sampling noise in the estimate of the best-fit χ^2, we set polychord to output $10\times$ more samples than its default. We verify that sampling the parameter space with a maximum posterior finder leads to χ^2 values that are insignificantly different from our best-fit ($\Delta\chi^2 < 1$). We obtain the evidences as a standard output of polychord. At each step, we also report the constraints on the marginalized IA parameters and their 68% confidence intervals.

With this method, we aim to find how many of the TATT parameters meaningfully improve the fit to the data. The evidence ratios are especially suited for this purpose because even though a model with an extra IA parameter might be *constrained*, the Occam factor in the evidence ratios can still penalize that model if the required prior volume is excessive when compared to a simpler model, Eq. (7). We note that according to our analysis choices, this procedure can only be carried out *after* the data and constraints are unblinded, and so we could not have applied the same reasoning before unblinding (e.g. as a strategy to optimize the selection of the fiducial IA model).

We have performed this test with SR data vectors built using both DES Y3 lens samples (redMaGiC and MagLim), as well as without including the SR likelihood at all, in which case all information comes from $\xi_\pm(\theta)$ on relatively large angular scales. For these three cases we find that the "no IA model" has the highest evidence, although it is only "weakly preferred" over the other models, based on the

Jeffreys scale, reflecting the fact that our inferred IA amplitudes are consistent with zero. We find in all cases that, once the tidal torquing term a_2 is free, the evidence ratios seem to suggest a preference for a redshift evolution. Apart from that, we find that the different SR lens samples yield slightly different levels of preference for the intermediate models such as NLA and NLA without z-evolution. Our results are shown in Table III, where stepping down line-by-line corresponds to increasing the IA model complexity, and for ease of interpretation we show only the case *without* the inclusion of the shear ratio likelihood (so note that the IA constraints presented in the table *do not exactly match the constraints reported elsewhere* in this work).

In summary, this test, as well those shown in Fig. 8, suggest that simpler IA models are a sufficient assumption for modeling the DES Y3 data. While this result is different from those in the pre-unblinding robustness tests which led to our choice of fiducial model (see Fig. 6), it is not inconsistent with expectations. Our earlier simulated tests used the best-fit TATT parameter values from the DES Y1 measurements. At these values, the impact of higher order IA contributions was large enough to require the full TATT model. However, the uncertainty in these Y1 measurements was fairly large, and they remain consistent with the overall smaller IA amplitudes found in this Y3 analysis. Smaller amplitudes allow for a less complex IA model, and indeed our current data appear to marginally prefer it.

Our results are consistent with other recent results, including [58,130], which also suggest low IA amplitudes. While the tests presented here provide additional information to the community for planning future analyses, we emphasize that further study is needed on the underlying IA behavior of typical source galaxies and the interaction with other elements on the model, including baryonic feedback and photometric redshifts, as well as the impact of noise. We have physical reasons to believe that higher-order IA contributions exist at some level, and the lack of a significant detection here does not imply that these terms can be safely ignored at increased precision or for different source samples. We encourage careful testing of IA model sufficiency in future analyses to avoid cosmological biases.

VII. MODEL ROBUSTNESS TESTS ON REAL DATA

In this section we present a number of analysis permutations, with the aim of stress testing the results described in the previous section. The tests fall naturally into a number of groups, which are discussed in more detail in the following paragraphs. For an overall summary, see Fig. 10.

This exercise is distinct from the tests in Sec. V; whereas there we were seeking to validate our model implementation *prior to unblinding*, we are now seeking to test the robustness of our unblinded results to reasonable variations to the analysis choices. Our focus here is on various aspects
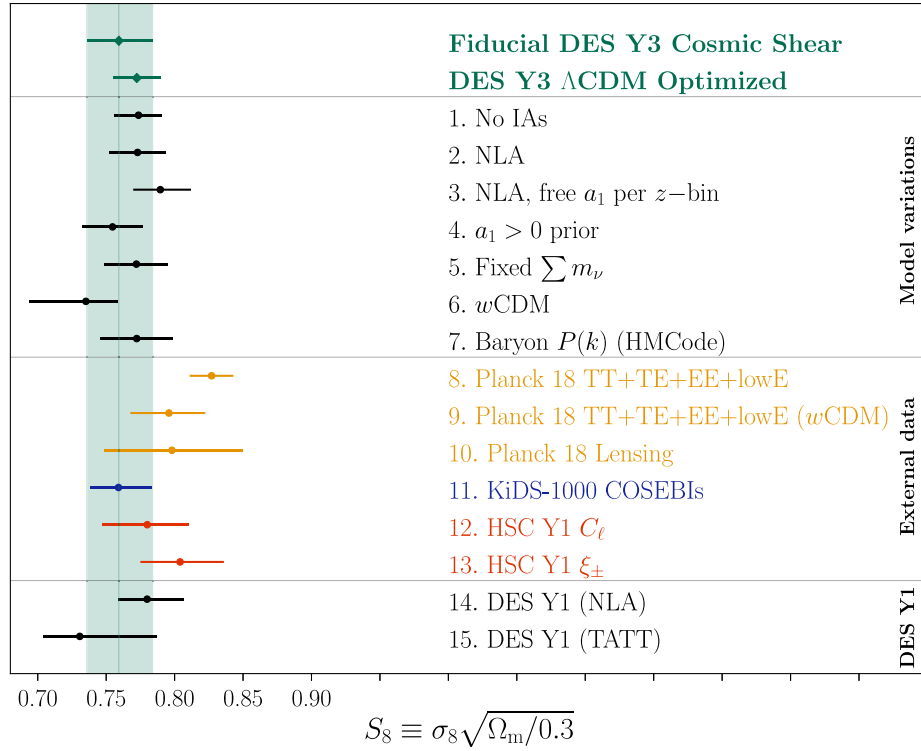
FIG. 10.　A summary of marginalized 1D constraints on S_8 shown in this paper. In the upper-most panel we show the main cosmological results of this paper: the DES Y3 cosmic shear constraints using fiducial and ΛCDM Optimized scale cuts. The panel below (marked "model variations", rows 1–7) shows a range of modified analyses, designed to test the robustness of the fiducial result, which are detailed in Secs. VI and VII). In the lower two panels we show equivalent constraints on S_8, both from external data (rows 8–13), and DES Y1 (rows 14 and 15). Points and error bars correspond to the marginal posterior mean and 68% confidence interval on S_8, with the exception of KiDS and HSC (rows 11–13) for which we report nominal headline results. Rows 1–10 are obtained using the DES Y3 fiducial analysis choices (including cosmology priors), while external lensing and DES Y1 rows 11–15 are *not re-processed* to match exactly the Y3 model, prior and scale cuts.

of the theory modeling. For a complementary raft of internal-consistency and data oriented tests, we refer the reader to our companion paper [72]. One can also find extensive catalog-level tests in Gatti *et al.* [78], which includes a null detection of shear B-modes in the Y3 data using both COSEBIs and pseudo-C_ℓs. Further tests of the PSF model and photo-z catalogs are described in other Y3 papers [55,76,79]. Also note that the details of the Y3 methodology, including the tests described in this section, were chosen prior to unblinding, and are not informed by the results described in Sec. VI A.

A. Baryonic $P(k)$ and neutrinos

One significant source of systematic uncertainty is in the modeling of the small- to intermediate-scale matter power spectrum. Uncertainties at high k arise both as a result of nonlinear clustering, a process that is typically calibrated using N–body simulations, and baryonic physics. Although we have verified our insensitivity to reasonable changes in baryonic and nonlinear growth scenarios in Sec. IV G, the tests there use noiseless synthetic data.

In order to assess the dependence of our results on our particular choice of $P_\delta(k)$ model, we repeat our fiducial ΛCDM analysis, with an alternative power spectrum estimator. That is, instead of HaloFit, which is our baseline choice, we use the halo model of Mead *et al.* [120], which has a nominal accuracy of 5% at $k < 10\,h\,\mathrm{Mpc}^{-1}$, as assessed by comparison with the Coyote Universe simulations. The halo model includes baryonic effects via two additional parameters: an amplitude B which governs the halo concentration-mass relation, and η_0, which is referred to as the halo bloating factor. We marginalize over both with wide flat priors $\eta_0 = [0.4, 1]$, $B = [1, 7.5]$. These priors are wider than those utilized by, e.g. Asgari *et al.* [5] and are intentionally chosen that way so we are agnostic with respect to the baryonic effects tested in Mead *et al.* [120]. Another difference with respect to the analysis of Asgari *et al.* [5] is that we free both parameters independently, as opposed to assuming a linear relation between them.

The results of this exercise are shown in Fig. 10 (labeled "HMcode $P(k)$") and in Fig. 11. As shown there, there is a small 0.5σ shift in S_8 due to this substitution. We do not, however, interpret this as the correction of residual
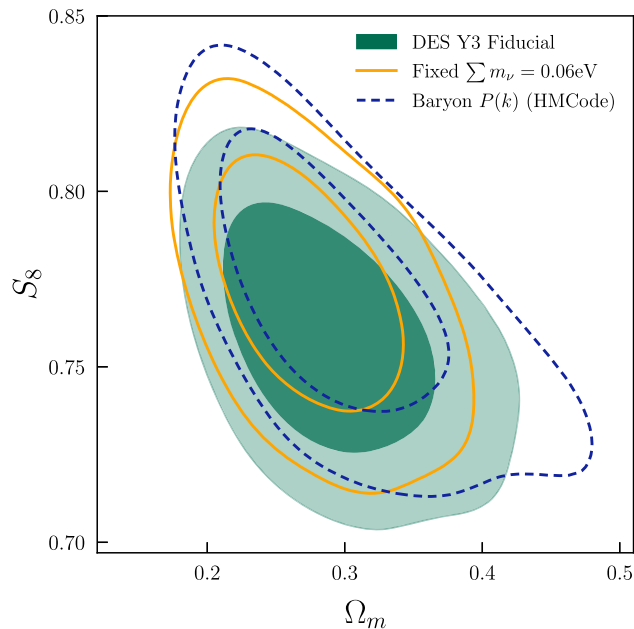
FIG. 11.   The marginal posterior distribution in the $S_8 \times \Omega_m$ plane for the model variations on the baryonic power spectrum (HMcode with 2 free parameters) and neutrino mass density (fixed at minimum mass). The results of our fiducial analysis is also shown (green). We observe consistency between these cases and our fiducial analysis, and do not interpret shifts as pointing to insufficiency in the analysis (see text).

baryonic physics present in the data, but rather a result of projection effects. Indeed, we verify that the halo-model parameters B, η_0 are completely unconstrained by the data within the prior bounds; this is a consequence of our conservative scale cuts, which are designed to remove angular scales on which baryonic feedback processes (and so the halo-model parameters) enter. The small shift is, therefore, simply an artifact of projecting the high-dimensional posteriors onto the 1D plane. To support this point, we verify that shifts in the same direction appear when analysing a gravity-only synthetic data vector with the same wide baryon priors. We see no significant improvement in the goodness-of-fit of our data when employing HMcode (a χ^2 of 236.8 *vs* our fiducial 237.7, with 2 added parameters).

In addition to the tests described above, we also repeat our fiducial analysis with the neutrino mass density parameter $\Omega_\nu h^2$ fixed. For this exercise, we set the sum of the neutrino masses, $\sum m_\nu$, to the lower limit obtained by oscillation experiments, assuming the normal (non-inverted) hierarchy, of 0.06 eV [187,188]. We maintain our fiducial choice of 3 degenerate neutrino species [89]. The neutrino mass parameter is not constrained by cosmic shear alone, so the small upward shift of around $\sim 0.2\sigma$ we observe in the 1D marginal S_8 constraint shown in Fig. 10 is again thought to be an effect of the projection of the high-dimensional parameter space with a different prior volume.

We show the 2D parameter constraints in the S_8–Ω_m plane under the variations of assumptions in the baryonic power spectrum and the neutrino mass density in Fig. 11. We note that despite the small differences in marginalized S_8 constraints, these analysis variations are still fully consistent with our fiducial analysis.

B. Intrinsic alignments

In this section we explore how plausible variations in our IA modeling can propagate to cosmology. In addition to the fiducial TATT model, we consider a number of alternatives, which are detailed below (see also Fig. 10). The variations cover a range of complexity scenarios, from the simplest case of null IAs (i.e. all parameters fixed to zero), through NLA and TATT to a version with added flexibility in redshift.

In Fig. 8 we consider our baseline result (green), alongside the equivalent using the two-parameter NLA model (blue; [6,7]'s fiducial choice), and an even simpler one-parameter version with no redshift dependence (dot-dashed yellow; [5]'s fiducial choice). Although only at the level of $\sim 0.5\sigma$, we see a shift in S_8 when switching between NLA and TATT, which is roughly consistent with the findings of Samuroff *et al.* [136] in DES Y1. This shift is not accompanied by a large improvement in the χ^2 per degree of freedom, but there is some preference for the simpler mode in terms of Bayesian evidence (see Sec. VI C and Table III). It is also notable that the variants of NLA with and without redshift variation give virtually identical cosmology results, primarily because the extra η_1 parameter is poorly constrained, and relatively uncorrelated with S_8. We also to note briefly that the impact of switching IA models also slightly rotates the best constrained direction in parameter space, with $\alpha = 0.576$ for NLA and $\alpha = 0.586$ in the fiducial TATT, when one defines the lensing amplitude as $\Sigma_8 = \sigma_8 (\Omega_m/0.3)^\alpha$.

Given the negative a_1 and hints of bimodality seen in Fig. 8, we run a version of the Y3 cosmic shear analysis with a restrictive prior $a_1 = [0, 5]$.[15] This results in almost no change to the best-fit S_8 (compare lines 1 and 6 in Fig. 10), although it does tighten the error bar slightly by restricting the posterior (row 6 of Fig. 10), which implies that the fact that our fiducial results encompass a region of negative IA space is not driving our cosmological constraints in a particular direction.

We also present a case with a flexible version of the NLA model, shown in Fig. 10 (line 5, labeled "NLA, free a_1 per z-bin"). The basic idea here is to test how limiting our assumption of power law redshift dependence is in this context, since we have no first-principles reason to expect IAs should obey this particular scaling. Interestingly,

---

[15]Our baseline prior bounds $a_1 = [-5, 5]$ were designed to be uninformative and avoid prior edge effects. It is, however, reasonable to expect that $a_1 > 0$, in the absence of systematics.

adding flexibility via extra TATT parameters, and via the ability to deviate from a power law redshift evolution, is seen to push S_8 in opposite directions relative to the basic NLA (cf. lines 1, 4, and 5 in Fig. 10). While we find a shift of around 1σ with respect to TATT (0.5σ with respect to NLA), the per-bin NLA model is significantly disfavored. The Bayesian evidence ratios strongly favor TATT and NLA over the per-bin NLA model (with $R = 237 \pm 60$ and 202 ± 49 respectively), and in the latter model we additionally see a significantly worse χ^2 (increased by about 10 with respect to TATT while the effective number of degrees of freedom is decreased by 1).

Taken as a whole, the tests described above paint a consistent picture. Apart from NLA per-bin, the IA modifications we explored cause shifts no greater than $\sim 0.5\sigma$ in S_8, even in the most extreme scenario where we neglect IAs entirely. In NLA per bin, we find a shift of 1σ with respect to our fiducial constraints, but also find that this model is disfavored by evidence ratios and goodness-of-fit tests. We therefore do not believe we that our IA modeling is *insufficient* to describe the data and, through the IA model selection described in Sec. VI C 2, actually have evidence that it might be simplified in future analyses. We do find a change in constraining power between NLA and TATT, with NLA (at fiducial scale cuts) being comparable to TATT at the ΛCDM -Optimized scale cuts. This suggests that our uncertainty budget is dominated by the lack of knowledge in modeling astrophysics on small cosmological scales. This is verified by our companion Amon *et al.* [72], Sec. XII.

VIII. COMPARISON WITH EXTERNAL DATA

After having verified that DES-only results are robust with respect to changes in astrophysics modeling assumptions, we now seek to place our results in the context of the wider field and to quantify tension with respect to subsets of external data.

A. External datasets

We describe a number of external datasets (see Table IV), to which we will compare our results. Where appropriate, we recompute the cosmological posteriors in order to facilitate a meaningful comparison. The marginalized S_8

constraints from the external datasets that meaningfully constrain this parameter alone are shown in the lower half of Fig. 10. The datasets we consider in this paper are largely common to those described in Dark Energy Survey Collaboration [186], Dark Energy Survey Collaboration [189], and Troxel *et al.* [7], with some more recent updates. Among these, as described in Sec. I, the KiDS and HSC surveys are Stage-III WL surveys like DES. The full set of surveys we consider is

(i) *KiDS-1000*: The KiDS weak lensing data comprise roughly 1000 square degrees and 21M galaxies ($n_{\mathrm{eff}} \sim 6.2/\mathrm{arcmin}^2$), and are described in Giblin *et al.* [62]. In their latest results papers, [5] present cosmic shear analyses using three different statistics; since they clearly designate their COSEBIs-based results as their fiducial analysis, we compare with these here. Note that we do not recompute the posteriors, but rather compare with the published results. In particular, one should be aware that our choice of IA model, nonlinear power spectrum and cosmological priors all differ from the fiducial analysis of Asgari *et al.* [5].

(ii) *HSC Y1*: The first year HSC lensing data are drawn from 137 square degrees, but go significantly deeper than either KiDS or DES, reaching $n_{\mathrm{eff}} \sim 22/\mathrm{arcmin}^2$. The data are described in Mandelbaum *et al.* [61], and are calibrated using image simulations [190]. As in the case of KiDS, we do not reanalyze the two-point data, instead comparing with the published results. Since, at the time of writing, there is no reason to prefer one over the other, we show both the real space analysis of Hamana *et al.* [28] and the power spectrum analysis of Hikage *et al.* [6] in Fig. 10. The differences between the two are thought to be statistical, due to different Fourier mode sensitivities. For the sake of clarity, we choose to show the latter in the visual comparison of Fig. 13.

(iii) *eBOSS*: We include spectroscopic baryon acoustic oscillation (BAO) measurements from eBOSS [3]. The BAO likelihood is assumed to be independent of DES, but we do recompute the posterior in our choice of cosmological parameter space (i.e. sampling A_s and Ω_m, and with the sum of the neutrino masses free).

TABLE IV. A summary of the external datasets used in this paper. More details can be found in Sec. VIII and the references listed.

Dataset	Type	Median Redshift	Area (sq. deg)	Source
DES Y3	WL	0.62	4143	This work
KiDS-1000	WL	0.54	777	Asgari *et al.* [5]
HSC Y1	WL	0.81	137	Hamana *et al.* [28], Hikage *et al.* [6]
eBOSS	BAO	0.7	6813	Alam *et al.* [3]
Pantheon	SNe	1.0	$\cdots$	Scolnic *et al.* [191]
Planck main	CMB $TT + TE + EE +$ lowE	1090	Full-sky	Planck Collaboration [183]
Planck lensing	CMB lensing	2.0	Full-sky	Planck Collaboration [192]

(iv) *Pantheon supernovae*: We also include the luminosity distances from type Ia supernovae from the Pantheon sample [191]; this dataset includes 279 type Ia supernovae from the PanSTARRS Medium Deep Survey $(0.03 < z < 0.68)$ and samples from SDSS, SNLS, and HST. The final Pantheon catalogue includes 1048 SNe, out to $z = 2.26$.

(v) *Planck 2018 Main*: These data are the final release from the Planck CMB experiment [183]. We incorporate the primary TT data on scales $30 < \ell < 2508$, and also the joint temperature and polarization measurements $(TT + TE + EE + BB)$ at $2 < \ell < 30$. As in previous analyses, we recompute the CMB likelihood in our fiducial parameter space, including neutrinos.

(vi) *Planck 2018 lensing*: We also consider CMB lensing from the Planck survey [192] as a separate dataset. These data probe an intermediate redshift $z \sim 2$, which is slightly higher than DES and somewhat lower than CMB temperature and polarization.

B. Quantifying tension

Assuring that the data collected by two different experiments have a quantified degree of agreement is crucial when performing a joint probes analysis. Therefore, for DES Y3, we have presented an thorough study on the ability of different tension metrics to identify inconsistencies among cosmological parameters measured by different experiments. We used simulated data to compute the predictions of different tension metrics belonging to two classes: Evidence-based methods and parameter-space methods. A robust way to quantify possible tensions is by combining those two types of metrics, as they answer somewhat different, but yet complementary, questions [86].

In DES, we utilize priors that are deliberately wide and uninformative such that "DES-only" constraints can be obtained. In this case, assessing tension utilizing the Bayes ratio, a broadly used evidence-based tension metric, can produce misleading results since it is largely dependent on the prior volume as discussed in Handley and Lemos [193]. To avoid this problem, for our choice of an evidence-based metric we compute the Bayesian suspiciousness [194] instead, a method that corrects for the prior dependence.

Consider two independent datasets A and B. The motivation behind suspiciousness is that the Bayes ratio R can be divided into two parts: the first one captures the prior dependence, i.e. the probability of the datasets matching given the prior width, which is quantified by the information ratio I:

$$\log I \equiv \mathcal{D}_A + \mathcal{D}_B - \mathcal{D}_{AB}, \qquad (31)$$

where

$$\mathcal{D}_D \equiv \int \mathcal{P}_D \log\left(\frac{\mathcal{P}_D}{\Pi}\right) d\theta, \qquad (32)$$

is the Kullback–Leibler Divergence [195], that can be understood as the amount of information that has been gained going from the prior Π to the posterior $\mathcal{P}$. The lower index D denotes the dataset from which the posterior is derived (A, B, or the joint data vector AB). The second part is the so-called Bayesian suspiciousness S, which is the part of the Bayes ratio left after subtracting the dependence on the prior, leaving only on the actual differences between the posteriors:

$$\log S = \log R - \log I. \qquad (33)$$

All the quantities required to compute the Suspiciousness metric are provided by a single nested sampling chain, just as the ones required to compute the Bayes ratio are, meaning the computational cost is the same in both cases. The necessary tools are implemented in the python package `anesthetic`[16] [196].

In addition, we calculate a Monte Carlo estimate of the probability of a parameter difference, set out in Raveri *et al.* [197], as our parameter space-based method. It relies on the calculation of the parameter difference probability density $\mathcal{P}(\Delta\theta)$ which, in the case of two uncorrelated datasets, is simply the convolution integral:

$$\mathcal{P}(\Delta\theta) = \int_{V_p} \mathcal{P}_A(\theta)\mathcal{P}_B(\theta - \Delta\theta)d\theta, \qquad (34)$$

where V_p is the prior support and $\mathcal{P}_A$ and $\mathcal{P}_B$ are the two posterior distributions of parameters. The probability of an actual shift in parameter space is obtained from the density of parameter shifts:

$$\Delta = \int_{\mathcal{P}(\Delta\theta) > \mathcal{P}(0)} \mathcal{P}(\Delta\theta)d\Delta\theta, \qquad (35)$$

which is the posterior mass above the contour of constant probability for no shift, $\Delta\theta = 0$.

Usually we only have discrete representations of the posterior samples and, since we are working with high dimensional parameter spaces, the posterior samples cannot be easily interpolated to a obtain a continuous function. Therefore, the integral in Eq. (35) needs to be performed using a Monte Carlo approach.

The idea is to compute the kernel density estimate (KDE) probability that $\Delta\theta = 0$ and the same at each of the samples from the parameter difference posterior. Then, the estimate of the integral in Eq. (35) is given by the number of samples with nonzero KDE probability, divided by the total

---

[16]https://github.com/williamjameshandley/anesthetic.

number of samples. These computations are done using the `tensiometer`[17] code.

1. Compatibility between low-z and high-z data

We now assess the consistency between high- and low-redshift cosmological probes. As in Dark Energy Survey Collaboration [73], we conclude that two datasets are statistically consistent if the *p*-value implied by our tension metrics is greater than 0.01. This same standard value was utilized in our internal consistency tests in Amon *et al.* [72]. In order to quote tension metrics, we first recompute the low-*z* (here defined as the combination BAO + SNe) and Planck 2018 posteriors with priors on cosmological parameters matched to those of DES Y3, as defined in Table I. In addition to assessing tension relative to our fiducial Y3 analysis, we also explore whether switching to the ΛCDM - Optimized scale cuts significantly changes our findings, since the one-dimensional result in Fig. 10 can offer hints, but not quantify the agreement between datasets.

Figure 12 shows the posteriors from DES as well as low-*z* and Planck 2018 in ΛCDM. In the full parameter space, for DES Y3 cosmic shear *vs* BAO + SNe in ΛCDM we find:

Suspiciousness : $0.5\sigma \pm 0.3\sigma$ (DES *vs* Low-*z* ΛCDM)

Parameter shift : 0.4σ (DES *vs* Low-*z* ΛCDM),

which implies $p(0.5\sigma) = 0.62 > 0.01$, and we conclude these datasets are consistent. This confirms more rigorously what is seen qualitatively in Fig. 12.

We similarly quantify the compatibility between DES Y3 cosmic shear and Planck 2018 in ΛCDM:

Suspiciousness : $2.3\sigma \pm 0.3\sigma$ (DES *vs* Planck ΛCDM)

Parameter shift : 2.3σ (DES *vs* Planck ΛCDM),

with a *p*-value $p(2.3\sigma) = 0.02 > 0.01$. We thus find that, according to our tension metrics, these datasets are consistent. We additionally explore the consistency of DES Y3 cosmic shear with Planck 2018 in our ΛCDM -Optimized setup and find:

Suspiciousness : $2.0\sigma \pm 0.4\sigma$

(DES optim. *vs* Planck ΛCDM)

Parameter shift : 2.1σ (DES optim. *vs* Planck ΛCDM),

which yields approximately $p(2.0\sigma) = 0.05 > 0.01$, again implying that these datasets are consistent. That result can be expected, at least qualitatively, by inspecting Figs. 10 and 12: while the constraint on S_8 is improved in the
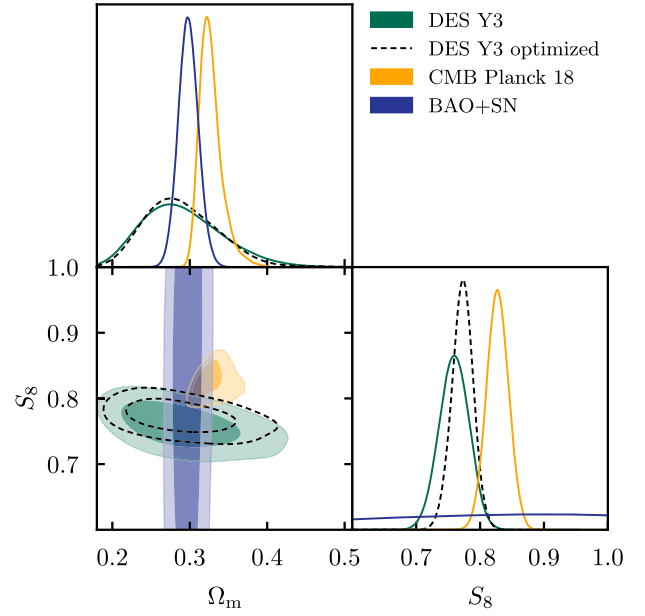
FIG. 12. DES Y3 and external data constraints from low and high redshift probes in ΛCDM. We present our fiducial and ΛCDM optimized constraints (green and black-dashed) in comparison with Planck 2018 (TT + EE + TE + lowE, no lensing; yellow) and the combination of BAO and type Ia SNe (SDSS BOSS and Pantheon respectively; blue). In all cases we show both the 68% and 95% confidence limits. We find no evidence for statistical inconsistency between DES Y3 cosmic shear and either external dataset.

optimized analysis, there is also a small shift toward Planck.

2. Comparing weak lensing surveys

We show our fiducial DES Y3 ΛCDM results (green shaded), alongside those of a number of contemporary weak lensing surveys in Fig. 13. Also shown (yellow) are the equivalent constraints from most recent Planck CMB data release (without lensing). Most notably, all the published cosmic shear analyses (including earlier, less constraining, results that are not shown here) favor lower S_8 than Planck, to varying degrees of significance. Although the cosmic shear surveys are independent, both in the sense that there is limited overlap between the catalogues (see Fig. 1), and that the measurement and analysis pipelines are largely separate, it is remarkable that their $S_8 \times \Omega_m$ posteriors overlap significantly, especially given that these weak lensing analyses are carried out blind.

That said, the naive comparison of the surveys is complicated by the fact that there are significant differences in the analysis choices underlying the published results, and unifying them becomes a crucial task [184]. Though it is quite possible to compute the metrics discussed in the previous section, interpreting them would be complicated, as it would be difficult to determine if any apparent tension
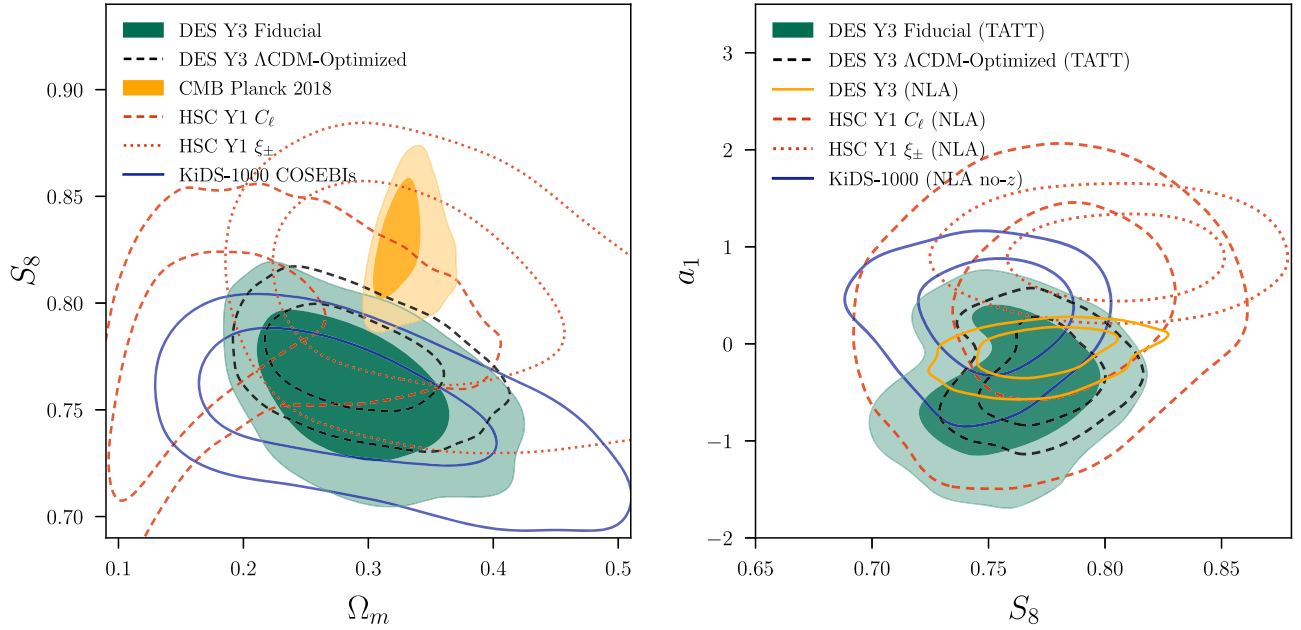
FIG. 13.   Posterior constraints on cosmology (left panel) and intrinsic alignment parameters (right panel) from contemporary weak lensing surveys. With the exception of Planck 2018, which is reanalyzed with DES Y3 priors, the weak lensing posterior data above are plotted as published by each collaboration, therefore a direct, quantitative comparison is complicated due to differing parameter priors, modeling and calibration choices. An overall qualitative agreement is seen in both panels, within approximately 1σ, with lensing surveys predicting similarly low S_8, and consistent a_1 amplitude.

were real, or due to differences in priors (see the discussion in [86]). A proper quantitative comparison would require matching priors and other analysis choices, and would ideally involve input from the different collaborations; such an exercise would be in line with the recommendations of [184] and is left for future work.

We can, however, compare our findings with the tension analyses that the various collaborations choose to present. For example, in DES Y1 cosmic shear the discrepancy relative to Planck 2018 was assessed to be at the level of 1.0σ and $0.5 \pm 0.3\sigma$ using the parameter shift and Suspiciousness metrics respectively [86]. These numbers can be compared directly with our findings in Sec. VIII B 1. We see that the discrepancy between cosmic shear and Planck 2018 has increased substantially in DES Y3 in comparison with DES Y1, from 1.0σ to 2.3σ. The latter number is, coincidentally, the same difference found in the comparison between Planck and the 3×2pt analysis of DES Y1 (including galaxy clustering and galaxy-galaxy lensing).

The KiDS-1000 cosmic shear analysis of Asgari *et al.* [5] opted to quantify their agreement with Planck using the Bayes ratio. They find "substantial" evidence for disagreement, with the caveat that the performance of this metric is known to be prior dependent. Though they also compute a Suspiciousness, they do not quote an interpretable value in terms of σ, due to difficulties in computing effective dimensionalities (see their Appendix B3). The approach of HSC differs slightly between their two published

analyses. [28] (their Sec. 6.6) rely on a comparison of projected contours, reporting no tension due to the apparent overlap in the $\sigma_8 \times \Omega_m$ plane. On the other hand, Hikage *et al.* [6] employ both the Bayes ratio and also differences in the log-likelihood at the MAP point in parameter space (see their Sec. 6.3 and [185]). They report no evidence for inconsistency based on these metrics.

In the right-hand panel of Fig. 13 we also show the IA model constraints from the various surveys. Although they are roughly consistent (to within $\sim 1\sigma$), it is worth being careful here. In all cases but KiDS-1000, the IA model has more flexibility than the one amplitude (an additional redshift scaling in HSC and DES Y1, and the extra TATT parameters in Y3), which means, for a given a_1, the predicted IA signal is not necessarily identical between the surveys. It is also true that, unlike cosmological parameters, IAs are *expected* to be dependent on both the galaxy selection and the shape measurement method. Differences, while interesting from the modeling perspective, are not necessarily a cause for concern.

IX. CONCLUSIONS

This paper and its companion, Amon *et al.* [72], present together the cosmological constraints from cosmic shear with over ~ 100 million galaxies from Dark Energy Survey Year 3 (DES Y3) shape catalogs, which cover 4143 square degrees. We model the cosmic shear signal in ΛCDM and constrain the lensing amplitude with 3% precision, finding

$S_8 = 0.759^{+0.023}_{-0.025}$. Our best constraint on ΛCDM is of $S_8 = 0.772^{+0.018}_{-0.017}$, at 2% precision, when optimizing the angular scales while still maintaining biases under control. Our results qualitatively agree well with previous lensing analyses based on the KiDS-1000, DES Y1 and HSC datasets, all of which favor lower S_8 than the most recent CMB measurements. Using quantitative tension metrics based on the full parameter space, we report a 2.3σ difference between our DES Y3 results and Planck 2018 (a *p*-value of 0.02), and we consider these datasets to be statistically consistent. At our present constraining power, we do not report a meaningful constraint on the equation-of-state parameter of dark energy in *w*CDM. That is, the cosmic shear likelihood does not significantly add information about the parameter *w* beyond its prior.

Throughout this paper, we have focused on the aspects of the DES Y3 cosmic shear analysis relating to astrophysical modeling. The overarching philosophy that guided this work and its conclusions can be summarized as follows. First, in a blinded fashion, we test our modeling assumptions on synthetic data obtained from theory pipelines and *N*-body mocks, in order to validate our fiducial analysis choices. We then obtain cosmology constraints from shear data that are verified to be internally consistent and calibrated to high confidence by our companion paper [72]. Finally, we proceed to relax our fiducial theory assumptions and vary model parametrizations, finding that the results to be robust to these variations, and then compare our constraints with those of external probes. The main conclusions of this paper are

(i) Informed by previous IA studies in DES Y1 data, we account for IAs with a 5-parameter model that includes tidal alignments and tidal torquing (TATT). We present tests of this modeling assumption on analytically generated data as well as realistic MICE (N-body) simulations, and find that TATT is able to capture complex IA signals, as well as that of simpler models such as NLA (Fig. 6);

(ii) We select angular scales conservatively to mitigate the effect of baryonic physics, the dominant small-scale systematic for this analysis. We show that our scale cuts suppress baryonic contamination as inferred from hydrodynamic simulations with varying levels of feedback strength, and utilize a gravity-only model for the matter power spectrum. We verify in synthetic data that residual biases due to baryons are well below 0.3σ in the $\Omega_m \times S_8$ plane, and that our selected scales are insensitive to uncertainties in the nonlinear power spectrum and in higher order shear contributions (Fig. 5);

(iii) The tension metrics we use in the full parameter space yield a 2.3σ discrepancy with respect to Planck (2018), with the leading contribution to the tension being our lower S_8. External probes at low-z (BAO + SNe), which are sensitive to Ω_m, are

within 0.5σ under the same metrics. We regard both these probes as statistically consistent with DES cosmic shear. We also find qualitative agreement between our data and external lensing results from HSC Y1 and KiDS-1000, all of which yield lower nominal S_8 values in comparison with Planck 2018 (Figs. 7, 12, and left panel of 13);

(iv) We demonstrate that our posteriors on IA and cosmological parameters are consistent within 1σ as we vary the parametrization of intrinsic alignments by simplifying our fiducial model from TATT to NLA with free/fixed redshift dependence. This is also true when we allow for free a_1^i amplitudes on each redshift bin *i*. We demonstrate that our posteriors on cosmological parameters are stable when inference is carried out at fixed neutrino mass and with free baryonic feedback parameters (Figs. 9, 10, and 11);

(v) We perform a detailed Bayesian evidence-based model selection for intrinsic alignments, finding that our data shows a weak preference for simpler (and better constrained) parametrizations. We additionally find that the best-fit IA amplitudes in DES Y3 are smaller than those in Y1. However, the two are consistent with each other, and also with other lensing surveys, although quantitative statements are challenging without further studies of e.g. sample selections and model differences. In combination with the fact that posteriors on $S_8 \times \Omega_m$ from simpler IA models are consistent with our fiducial choice (TATT), these findings point to less complex parametrizations, such as NLA, being a sufficient and unbiased description of our data (Fig. 8, Table III, and right panel of Fig. 13).

Additionally, we share a summary of the main conclusions of our companion paper [72], demonstrated with the same Y3 cosmic shear analysis, and point the reader to that paper for details:

(i) The analysis is shown to be robust to the choice of redshift calibration sample, either photometric of spectroscopic, methodology and the modeling of redshift uncertainty, within $\sim 0.5\sigma$.

(ii) We model the impact of blending using state-of-the-art image simulations and show that our posteriors are stable to this correction, within 0.5σ.

(iii) The analysis passes all internal consistency tests, finding that the cosmology is stable across redshifts, angular scales and measurement statistics.

(iv) The impact of additive shear systematics, such as PSF contamination and B-modes is assessed and found to be negligible for the analysis.

(v) We investigate the limiting factors of the cosmic shear constraints and find observational systematics are subdominant compared to systematics due to modeling astrophysical effects.

The results presented in this study show that cosmic shear has reached the requirements of percent level precision: every source of systematic uncertainty must be controlled to better than a percent of the signal, since our statistical uncertainty on the amplitude parameter S_8 is three percent. When the first detections of cosmic shear were published in 2000, it was far from a given that this level of precision was achievable. With the full DES survey awaiting analysis, and the much larger surveys from Euclid and the Rubin Observatory's LSST starting in a few years, it is interesting to consider prospects for further qualitative advances.

On the theoretical side, we are limited by our ability to describe the astrophysics of small scales, in particular baryons and IA. Baryonic physics is the driver of our scale cuts, and we will need to rely on advances in hydrodynamic simulations, constrained by complementary observations such as Sunyaev-Zel'dovich (SZ) maps, otherwise the necessary cuts and/or marginalization will cause more information to be discarded. Conversely, we have found that intrinsic alignments are likely to contribute less than the most conservative forecasts, but more studies are required to extended our findings to arbitrary galaxy samples. Parallel advances in shear estimation and calibration and the photo–zs of source galaxies are required to keep pace with statistical errors. Beyond cosmic shear, a suite of statistical measures that capture the non-Gaussian information in the shear field have been developed, such as peak statistics and three-point correlations. These will add complementary information and also serve as cross-checks on the robustness of the signal. We can look forward to new cosmological tests with the application of these approaches to DES and future surveys.

Finally, we reiterate that, while the assumption of ΛCDM as the ultimate end-to-end model connecting the early- and late- Universe has withstood another test, our result should be understood within a broader context. It is still an open puzzle that modern weak lensing surveys, independently and in blind analyses, find a lower lensing amplitude than predicted by the CMB, and the difference between DES cosmic shear itself with respect to Planck has increased from 1.0σ in DES Y1 to 2.3σ in Y3. More effort is required to quantify the agreement between lensing studies, especially toward unifying and homogenizing their analyses and exploiting their complementarities.

ACKNOWLEDGMENTS

APPENDIX A: CONSTRUCTION OF THE MICE SOURCE CATALOG AND RESULTS

In this section, we discuss the construction of a mock weak lensing source catalog with the MICE N-body simulation. Significantly, in addition to cosmological shear, these mock catalogs contain a realistic IA component, making them a good testing ground for our modeling; this is the primary motivation for using them here, as discussed in Sec. V B. The implementation of the IA signal into MICE is described in far more detail in Hoffmann *et al.* [175], and is summarized below.

Each MICE galaxy has a (projected) shape assigned to it:

$$\gamma = \gamma_{\mathrm{G}} + \gamma_I + \epsilon. \qquad (A1)$$

The cosmological part of this is obtained via ray tracing (see [166]); γ_I is the coherent intrinsic component, which is generated via semi-analytic modeling (see below and [175]), and ϵ is random Gaussian shape noise.

For the purposes of our test, it is desirable that the overall constraining power of the mock catalog (in terms of the figure-of-merit in the $S_8 \times \Omega_{\mathrm{m}}$ plane) resembles that of the fiducial source catalog; to that end, we match the constraining power of Y3 cosmic shear by adding a shape noise component to the covariance matrix of the hypothetical MICE survey, generated with CosmoLike. This scatter is chosen such that the uncertainty in the shape noise dominated regime is equivalent between MICE and METACAL: $\Delta C^{\kappa\kappa}_{\mathrm{METACAL}}(\ell) = \Delta C^{\kappa\kappa}_{\mathrm{MICE}}(\ell)$, with

$$\Delta C^{\kappa\kappa}(\ell) \sim \frac{1}{\sqrt{f_{\mathrm{sky}}}} \left(\frac{\sigma_e^2}{\bar{n}} \right), \qquad (A2)$$

where f_{sky} is the observed fraction of the total sky area, $\bar{n}$ is the (effective) galaxy number density and σ_e^2 is the variance of the ellipticities. With $\bar{n}$ and f_{sky} fixed in both catalogs (our MICE catalog has approximately 130M galaxies over an area of 5191 deg^2 while METACAL has 100 M galaxies spanning an area of 4143 deg^2), and $\sigma_e = 0.261$ fixed in METACAL, we adjust $\sigma_{e,\mathrm{MICE}}$ so that the equality is reached,

and verify that we achieve a comparable constraining power as DES Y3 in the 2D $S_8 \times \Omega_{\mathrm{m}}$. The IA contribution to the MICE shears (γ_I) has, additionally, an irreducible noise coming from a randomization of galaxy orientations. This randomization is a component of the IA modeling and has been tuned to match observed IA correlations from the BOSS LOWZ sample [181].

It is also desirable that the source galaxy photometric properties in the mock also resemble those of galaxies in the fiducial DES Y3 catalog, since IAs can depend on galaxy color and luminosity. In summary, we verify that the distribution of riz magnitudes and color-magnitude distributions are similar between MICE and METACALIBRATION. It would also be beneficial if the redshift distributions $n(z)$ on the mock catalog were closely matched to what is found in real data (Fig. 3). Since the implementation in MICE of the SOMPZ framework utilized in DES Y3 [55,79] is beyond the scope of this work, and since the goal of this model test should be agnostic to the exact shape of the redshift distributions, we utilize directional neighborhood fitting (DNF) photo-zs [202] for our mock $n(z)$ s, as these are made available by default with the MICE data releases. In general, we find that DNF redshift distributions are narrower and less overlapping across bins than the fiducial DES Y3 $n(z)$s.

With the mock catalog constructed, we then apply the same pipelines that were used for measuring the tomographic cosmic shear data vector $\xi_\pm^{ij}(\theta)$ and inferring cosmological parameters. Where possible we mirror the model choices and nuisance parameter marginalization used in the analysis of the real data.

We measure 2 sets of shear correlation functions from the mock: a "MICE Baseline" data vector estimated from the IA-free GG signal (i.e. using only the γ^G component of Eq. (A1), and a "MICE IA" data vector which includes the full GG + GI + II signal, as well shape noise added at the catalog level. Since the former captures the cosmological signal (plus cosmic variance), it provides a useful fiducial case, relative to which we can gauge biases. The input cosmology is known for MICE, however the IA signal is, by construction, not exactly mapped into a set of NLA or TATT parameters. Thus, for a single realization of the mock, our expectations are (1) that the constraints on the MICE Baseline GG-only vector are consistent with the input cosmology while at the same time the IA parameter constraints are consistent with zero; (2) that cosmology constraints on the full MICE IA data vector are not excessively biased with respect to the baseline constraints.

Both our expectations are fulfilled, with MICE IA offset by $\sim 0.6\sigma$ from the peak of baseline. Our results are shown in Fig. 14. Although this shift is larger than the 0.3σ tolerance we applied to previous tests on analytic data, it is worth bearing in mind that the nature of the test discussed here is slightly different. That is, we only have one realization of the noise in the IA vector (both cosmic
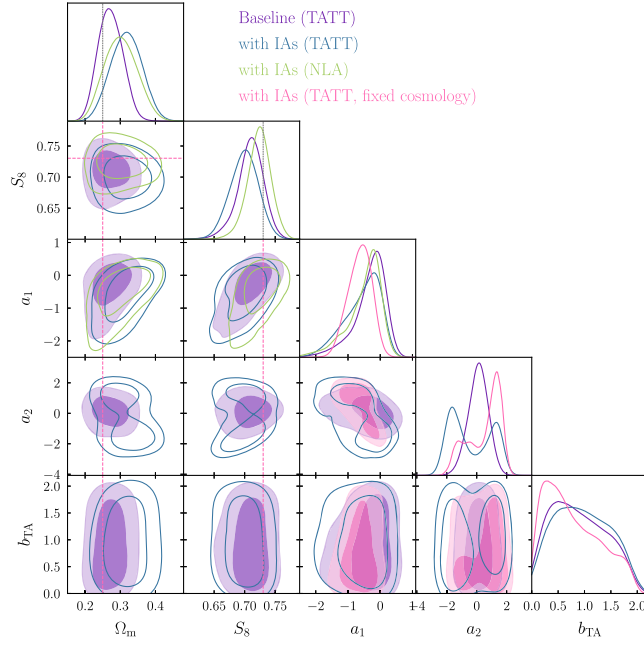
FIG. 14.   MICE posteriors: The baseline case (purple) includes only the GG part of the signal (no IAs) and IA parameters are consistent with zero. The contours labelled "with IAs" (blue, green, pink) includes GG + GI + II, with the IA model indicated in parentheses. Note that two IA redshift power law indices are included in the fits, as per the fiducial Y3 model; they are not shown here as they are only very weakly constrained, and the contours are uninformative. Dashed pink lines are the input MICE cosmology.

variance and shape noise). While this test is valuable, in the sense that large shifts would be a sign of significant problems in the fidelity of our model, offsets within ~ 1–2σ are entirely consistent with noise.

We also run the inference pipeline on the full IA data vector while fixing the cosmological parameters at the true MICE input to isolate the IA signal. Those are the "reduced" parameter space curves in Fig. 14. While constraints obtained this way are artificially tight, the exercise shows that the IA parameters measured in the reduced case are consistent within 1σ with parameters obtained while varying cosmology. Additionally, we do find a marginal preference for a negative a_1 parameter in both cases that involve nonzero IA parameters. Although this is likely not a physical effect, and nor in this case can it be the result of unmodeled photo-z error, it is quite conceivable that it is simply a result of a small but positive "true" IA signal, combined with shape noise.

This test on MICE is aimed at verifying that our fiducial model can recover unbiased cosmological constraints from a data vector that includes intrinsic alignments and that is not generated by an analytic pipeline. While we do obtain reasonable results and the present test has the rare benefit of including a realistic, simulated (N–body with semianalytic model) IA signal, it is
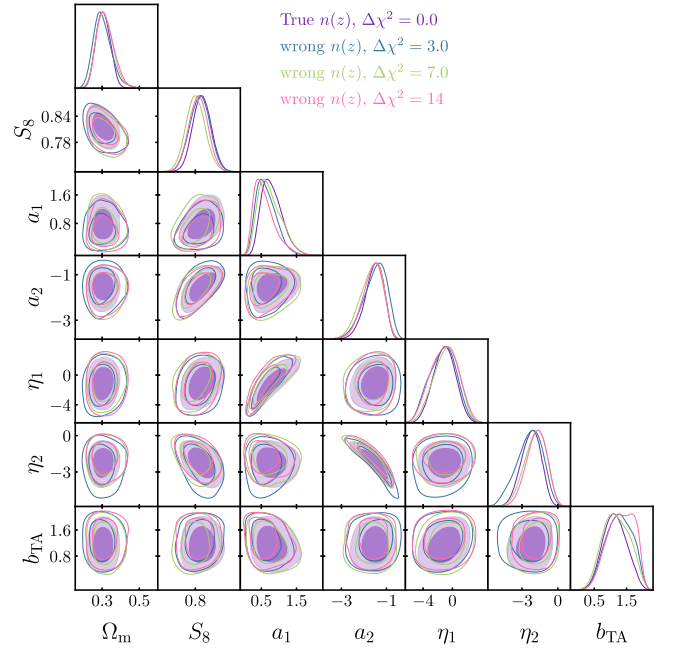

FIG. 15.   Analysis of synthetic data generated with the inclusion of unmodeled redshift errors. The purple contour shows the baseline posterior, obtained by analysing a simulated TATT data vector with the correct $n(z)$; the three other colors show redshift error scenarios of varying extremity. In each case the difference in χ^2 induced by the redshift error, at the input point in parameter space, is indicated in the legend.

statistically weaker than a more complete validation of DES pipelines on simulations [88], mainly due to the lack of independent realizations. A complete analysis on a relatively large number of MICE mocks is left for future work.

APPENDIX B: ROBUSTNESS OF IA TO UNMODELED REDSHIFT ERROR

In this Appendix we set out in more detail the tests on analytic data introduced in Sec. V A 3. These tests, which are based on noiseless analytic data, are designed to test the specific question of whether our choice of IA model behaves well in the presence of realistic errors in the redshift distributions. We focus here on synthetic data vectors which do not contain real data complexity, in which case a thorough testing of redshift calibration is more complicated and performed by our companion [72]. We use the ensemble of 6000 SOMPZ realizations of $n(z)$'s, described in Myles *et al.* [79]; for each sample of the Y3 redshift distributions, we compute a simulated cosmic shear data vector $\xi_{\pm}^{\text{sample}}(\theta)$ at a fixed set of input cosmological parameters. Using the data covariance, we can then calculate the $\Delta\chi^2$ between $\xi_{\pm}^{\text{sample}}(\theta)$ and a similarly generated cosmic shear data vector, but with the fiducial (mean) $n(z)$ as input, $\xi_{\pm}^{\text{mean}}(\theta)$. We find that the distribution of $\Delta\chi^2$ obtained for the 6000 samples peaks close to zero

($\Delta\chi^2 < 1.0$, corresponding to small perturbations of the data vector) and has a long tail out to more extreme cases ($\Delta\chi^2 \sim 50.0$). Given our finite computing resources, we do not run nested sampling chains on all of the 6000 scenarios, but rather choose three of increasing severity,

corresponding to the 60th, 95th, and 99th percentiles of the $p(\Delta\chi^2)$ distribution.

We next translate these $\Delta\chi^2$ errors into cosmological biases by analysing the three $\xi_\pm^{\rm sample}(\theta)$ vectors with our fiducial setup. Although that setup includes redshift
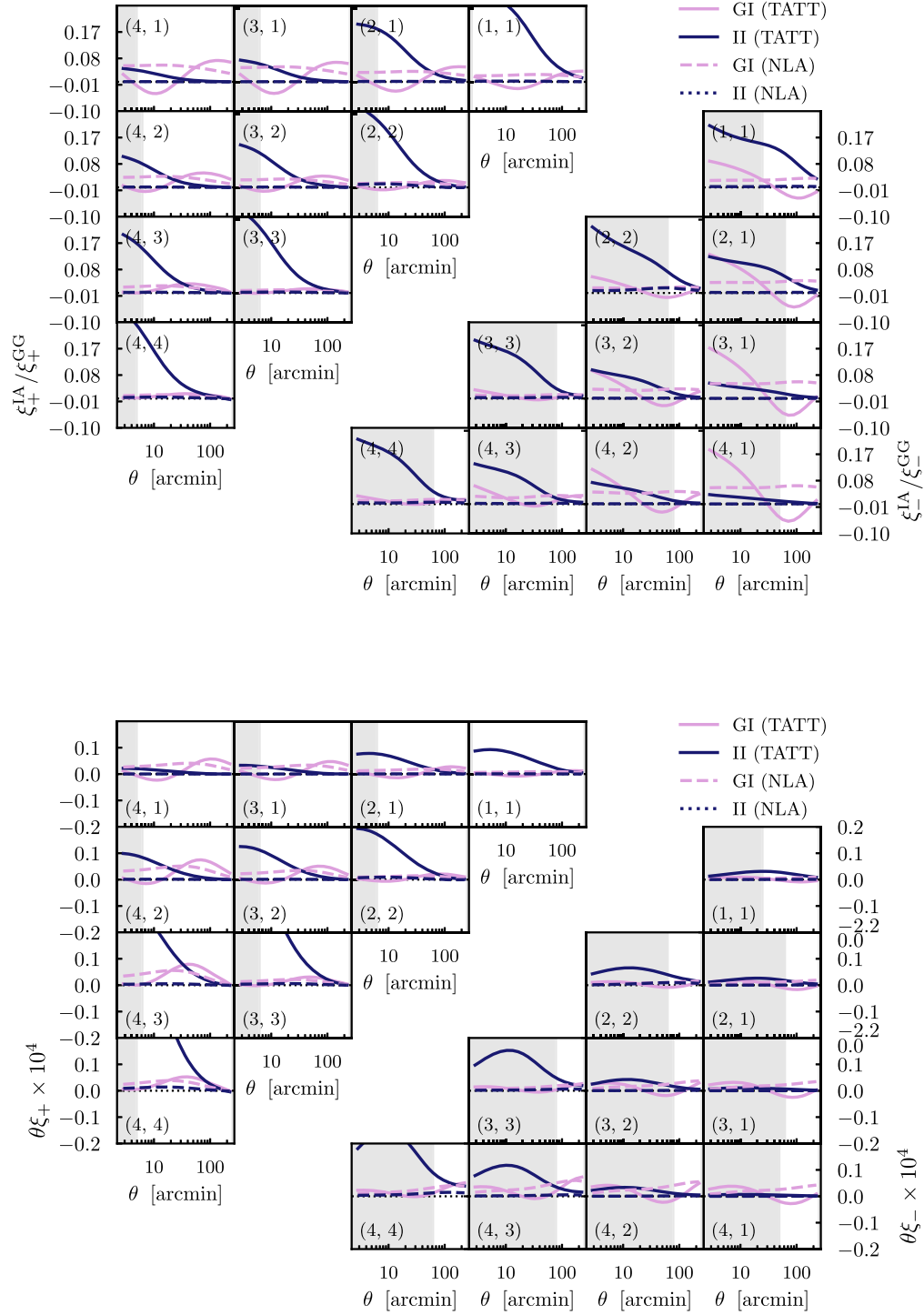

FIG. 16. The best fitting IA predictions, based on NLA and TATT analyses. In the two panels we show the fractional IA contributions relative to the cosmological signal (top), and the absolute contributions (bottom). Both IA components, GI and II, are plotted separately (blue and light purple). As before, shaded regions indicate scales discarded from the analyses.

nuisance parameters Δz^i, it cannot explicitly account for perturbations in the $n(z)$ shape that do not map well into the first moment of the $n(z)$ distribution. More extensive testing of this is presented in Amon *et al.* [72]; Cordero *et al.* [82].

The results of this exercise are shown in Fig. 15. Each of the unfilled contours represents a different scenario of redshift error, and can be compared with the solid purple (which has no redshift error). In this limited testing scenario

with synthetic data we see no large biases in the IA model parameters or S_8, which are recovered correctly, and no hints that the TATT model parameters are absorbing the unmodeled error.

APPENDIX C: COMPARING NLA AND TATT IN DES Y3

In this appendix we explore in more detail the differences between our fiducial IA model for Y3 (TATT), and the
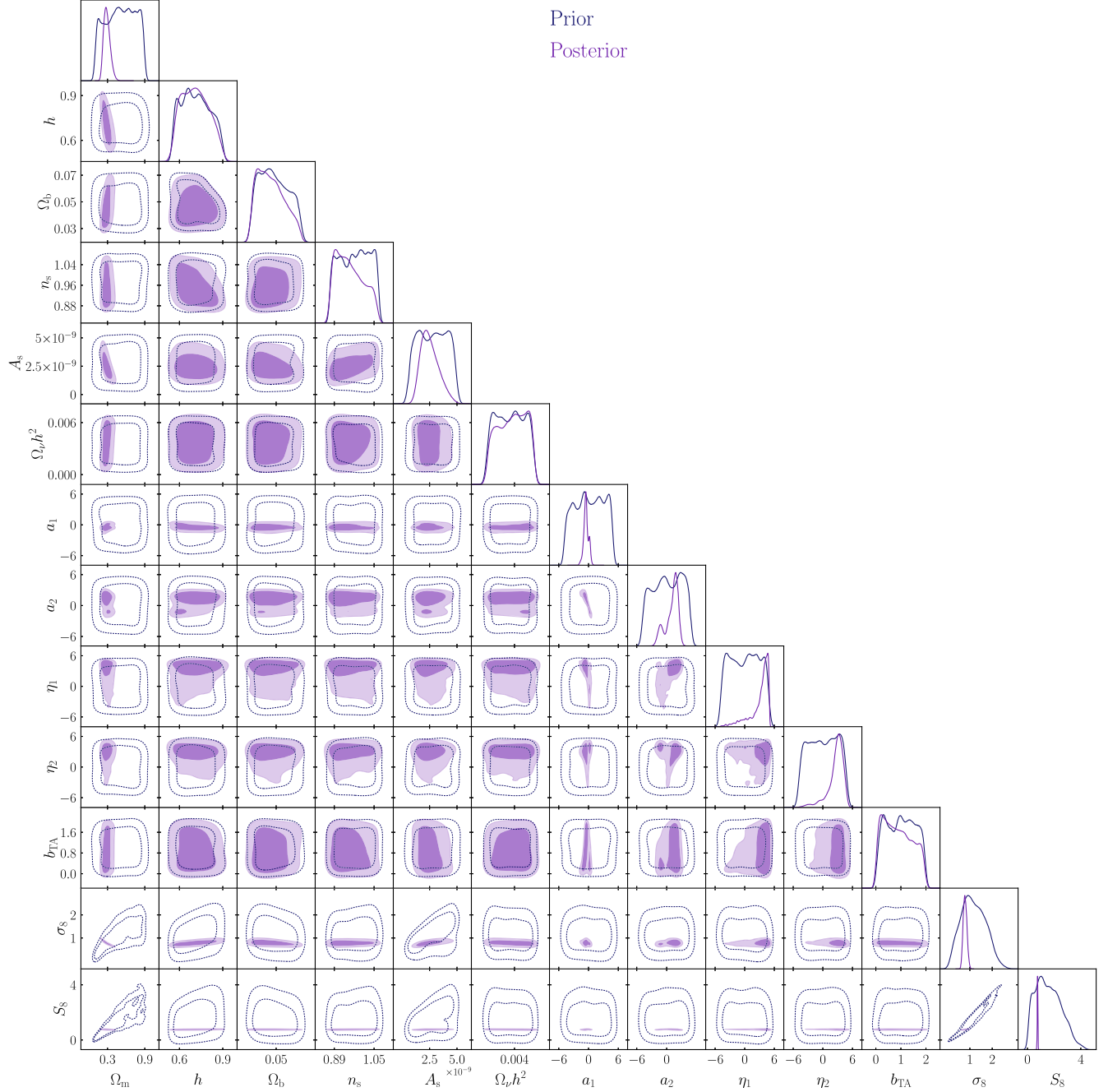

FIG. 17. Posterior distributions (purple solid) and priors (blue dashed) of our analysis. We intentionally leave out hard-boundary corrections on the distributions above for ease of visualization. Our 1D marginalized priors are flat in the cosmological parameters described in Table I, but sampling and 1-dimensional marginalization can make them look noisy and nonuniform.

more commonly used NLA model. As discussed in Sec. IV D 2, TATT is a physically motivated model containing NLA, such that in some limit (a_2, $b_{TA} \to 0$), the two are the same. Among various other permutations, we fit both the two-parameter NLA model and the five-parameter TATT model to the Y3 cosmic shear data. Using the more complex IA model results in a slight widening of the contours, as can be seen in Fig. 8, and also a rotation in the direction of the σ_8–Ω_m degeneracy. These two effects combine to produce a $\sim$17% difference in the projected error bar on S_8 between the two models. When considering the 2D figure of merit in the S_8–Ω_m plane, the difference is $\sim$25%.

In addition to the difference in constraining power, NLA and TATT result in qualitatively different predictions for the IA signal. We illustrate this in Fig. 16, which shows the theory IA contributions, generated using the respective best fitting IA parameters from the two chains. Both the absolute signal, and the contribution relative to the cosmological shear (GG) are included in the two panels. Although the choice of model does not change the conclusion that IAs are subdominant in all bins (at the level of a few percent), the shape and sign of the IA correlations do differ somewhat. Strikingly, TATT predicts a much stronger II signal than NLA, which is largely driven by the tidal torque (a_2) part of the model. It is also worth remarking here that although they look different, neither of these IA scenarios has been convincingly ruled out by direct measurements. That is, if one generates projected intrinsic alignment correlations (see e.g. [203], Sec. III.2 for the full definition) w_{g+} and w_{++} predictions, using the IA power spectra from these fits, the results are within the range allowed by measurements on faint blue and red galaxies at low redshift from SDSS [203,204].

APPENDIX D: FULL POSTERIOR CONSTRAINTS

We show a set of 2D projections of our cosmological and IA parameter posteriors in Fig. 17, along with their priors. We note that σ_8 and S_8 are derived parameters which we do not sample over, so projections make their apparent priors nonuniform. Many of the parameters in our analysis are either prior dominated, or not of physical interest, and so are not shown in the main part of the paper. They are included here for completeness.

APPENDIX E: CHANGES AFTER UNBLINDING

Three changes to our analysis happened after unblinding, neither of them affecting significantly the DES Y3 cosmic shear cosmological constraints, particularly S_8. The first is a planned modification to the covariance matrix: after the tests described in Sec. V succeed and cosmology constraints are obtained, the analytic covariance matrix is recomputed at the best-fit (maximum posterior) parameters of the full 3×2pt data, and our cosmological constraints are updated with new nested sampling chains.

The second change involves the DES Y3 lens sample, which only enters the cosmic shear data via lensing ratios (Sec. IV F). We substitute the original redMaGiC sample by the magnitude-limited MagLim sample. We point the reader to Dark Energy Survey Collaboration [73] for further details and motivation for this change.

The third change is decision for presenting the ΛCDM -optimized scale cuts in cosmic shear as one of the main DES Y3 results. While fundamentally the optimized scale cuts also lead to robust $<0.3\sigma$ shifts in our simulated analysis and therefore could have been a reasonable pre-unblinding choice on a $\xi_\pm$-only analysis, this was only decided after unblinding. We report that here for transparency.

[1] Planck Collaboration, Astron. Astrophys. **641,** A6 (2020).
[2] A. G. Riess, S. Casertano, W. Yuan, J. B.Bowers, L. Macri, J. C. Zinn, and D. Scolnic, Astrophys. J. Lett. **908,** L6 (2021).
[3] S. Alam *et al.*, Phys. Rev. D **103,** 083533 (2021).
[4] W. L. Freedman *et al.*, Astrophys. J. **882,** 34 (2019).
[5] M. Asgari *et al.*, Astron. Astrophys. **645,** A104 (2021).
[6] C. Hikage *et al.*, Publ. Astron. Soc. Jpn. **71,** 43 (2019).
[7] M. A. Troxel *et al.*, Phys. Rev. D **98,** 043528 (2018).
[8] T. Tröster *et al.*, Astron. Astrophys. **633,** L10 (2020).
[9] Dark Energy Survey Collaboration, Phys. Rev. D **102,** 023509 (2020).
[10] A. B. Mantz *et al.*, Mon. Not. R. Astron. Soc. **446,** 2205 (2015).
[11] M. Bartelmann and P. Schneider, Phys. Rep. **340,** 291 (2001).

[12] J. A. Frieman, M. S. Turner, and D. Huterer, Annu. Rev. Astron. Astrophys. **46,** 385 (2008).
[13] W. Hu and B. Jain, Phys. Rev. D **70,** 043009 (2004).
[14] D. Huterer, Phys. Rev. D **65,** 063001 (2002).
[15] D. J. Bacon, A. R. Refregier, and R. S. Ellis, Mon. Not. R. Astron. Soc. **318,** 625 (2000).
[16] N. Kaiser, G. Wilson, and G. A. Luppino, arXiv:astro-ph/0003338.
[17] L. Van Waerbeke *et al.*, Astron. Astrophys. **358,** 30 (2000).
[18] D. M. Wittman, J. A. Tyson, D. Kirkman, I. Dell'Antonio, and G. Bernstein, Nature (London) **405,** 143 (2000).
[19] W. Hu, Astrophys. J. **522,** L21 (1999).
[20] B. Jain and U. Seljak, Astrophys. J. **484,** 560 (1997).
[21] J. Miralda-Escude, Astrophys. J. **380,** 1 (1991).

[22] M. Asgari, C. Heymans, C. Blake, J. Harnois-Deraps, P. Schneider, and L. V. Waerbeke, Mon. Not. R. Astron. Soc. **464,** 1676 (2017).

[23] J. Benjamin, C. Heymans, E. Semboloni, L. V. Waerbeke, H. Hoekstra, T. Erben, M. D. Gladders, M. Hetterscheidt, Y. Mellier, and H. K. C. Yee, Mon. Not. R. Astron. Soc. **381,** 702 (2007).

[24] M. L. Brown, A. N. Taylor, D. J. Bacon, M. E. Gray, S. Dye, K. Meisenheimer, and C. Wolf, Mon. Not. R. Astron. Soc. **341,** 100 (2003).

[25] T. Erben *et al.*, Mon. Not. R. Astron. Soc. **433,** 2545 (2013).

[26] L. Fu *et al.*, Astron. Astrophys. **479,** 9 (2008).

[27] T. Hamana *et al.*, Astrophys. J. **597,** 98 (2003).

[28] T. Hamana *et al.*, Publ. Astron. Soc. Jpn. **72,** 16 (2020).

[29] M. Hetterscheidt, P. Simon, M. Schirmer, H. Hildebrandt, T. Schrabback, T. Erben, and P. Schneider, Astron. Astrophys. **468,** 859 (2007).

[30] C. Heymans *et al.*, Mon. Not. R. Astron. Soc. **361,** 160 (2005).

[31] H. Hoekstra H. K. C. Yee, M. D. Gladders, L. F. Barrientos, P. B. Hall, and L. Infante, Astrophys. J. **572,** 55 (2002).

[32] E. M. Huff, C. M. Hirata, R. Mandelbaum, D. Schlegel, U. Seljak, and R. H. Lupton, Mon. Not. R. Astron. Soc. **440,** 1296 (2014).

[33] E. M. Huff, T. Eifler, C. M. Hirata, R. Mandelbaum, D. Schlegel, and U. Seljak, Mon. Not. R. Astron. Soc. **440,** 1322 (2014).

[34] M. Jarvis, G. M. Bernstein, P. Fischer, D. Smith, B. Jain, J. A. Tyson, and D. Wittman, Astron. J. **125,** 1014 (2003).

[35] M. Jarvis, B. Jain, G. Bernstein, and D. Dolney, Astrophys. J. **644,** 71 (2006).

[36] M. J. Jee, J. A. Tyson, M. D. Schneider, D. Wittman, S. Schmidt, and S. Hilbert, Astrophys. J. **765,** 74 (2013).

[37] M. J. Jee, J. A. Tyson, S. Hilbert, M. D. Schneider, S. Schmidt, and D. Wittman, Astrophys. J. **824,** 77 (2016).

[38] M. Kilbinger *et al.*, Mon. Not. R. Astron. Soc. **430,** 2200 (2013).

[39] T. D. Kitching *et al.*, Mon. Not. R. Astron. Soc. **442,** 1326 (2014).

[40] A. Leauthaud *et al.*, Astrophys. J. Suppl. Ser. **172,** 219 (2007).

[41] H. Lin, S. Dodelson, H.-J. Seo, M. Soares-Santos, J. Annis, J. Hao, D. Johnston, J. M. Kubo, R. R. R. Reis, and M. Simet, Astrophys. J. **761,** 15 (2012).

[42] R. Massey *et al.*, Astrophys. J. Suppl. Ser. **172,** 239 (2007).

[43] L. Miller *et al.*, Mon. Not. R. Astron. Soc. **429,** 2858 (2013).

[44] A. Refregier, J. Rhodes, and E. J. Groth, Astrophys. J. Lett. **572,** L131 (2002).

[45] J. Rhodes, A. Refregier, N. R. Collins, J. P. Gardner, E. J. Groth, and R. S. Hill, Astrophys. J. **605,** 29 (2004).

[46] T. Schrabback *et al.*, Astron. Astrophys. **516,** A63 (2010).

[47] M. Yoon, M. J. Jee, J. A. Tyson, S. Schmidt, D. Wittman, and A. Choi, Astrophys. J. **870,** 111 (2019).

[48] S. Bridle *et al.*, Mon. Not. R. Astron. Soc. **405,** 2044 (2010).

[49] C. Heymans *et al.*, Mon. Not. R. Astron. Soc. **368,** 1323 (2006).

[50] T. D. Kitching *et al.*, Mon. Not. R. Astron. Soc. **423,** 3163 (2012).

[51] R. Mandelbaum *et al.*, Astrophys. J. Suppl. Ser. **212,** 5 (2014).

[52] R. Massey *et al.*, Mon. Not. R. Astron. Soc. **376,** 13 (2007).

[53] M. Gatti *et al.*, Mon. Not. R. Astron. Soc. **477,** 1664 (2018).

[54] J. Prat *et al.*, Mon. Not. R. Astron. Soc. **487,** 1363 (2019).

[55] R. Buchs, C. Davis *et al.*, Mon. Not. R. Astron. Soc. **489,** 820 (2019).

[56] A. Alarcon , C. Sánchez, G. M. Bernstein, and E. Gaztañaga, Mon. Not. R. Astron. Soc. **498,** 2614 (2020).

[57] C. Sánchez and G. M. Bernstein, Mon. Not. R. Astron. Soc. **483,** 2801 (2019).

[58] A. H. Wright, H. Hildebrandt, J. L. van den Busch, C. Heymans, B. Joachimi, A. Kannawadi, and K. Kuijken, Astron. Astrophys. **640,** L14 (2020).

[59] J. T. A. de Jong *et al.*, Messenger **154,** 44 (2013).

[60] H. Aihara *et al.*, Publ. Astron. Soc. Jpn. **70,** S4 (2018).

[61] R. Mandelbaum *et al.*, Publ. Astron. Soc. Jpn. **70,** S25 (2018).

[62] B. Giblin *et al.*, Astron. Astrophys. **645,** A105 (2021).

[63] S. Alam *et al.*, Astrophys. J. Suppl. Ser. **219,** 12 (2015).

[64] C. Heymans *et al.*, Astron. Astrophys. **646,** A140 (2021).

[65] J. A. Blazek, N. MacCrann, M. A. Troxel, and X. Fang, Phys. Rev. D **100,** 103506 (2019).

[66] E. Krause, T. Eifler, and J. Blazek, Mon. Not. R. Astron. Soc. **456,** 207 (2016).

[67] J. DeRose, R. H. Wechsler, J. L. Tinker, M. R. Becker, Y.-Y. Mao, T. McClintock, S. McLaughlin, E. Rozo, and Z. Zhai, Astrophys. J. **875,** 69 (2019).

[68] H.-J. Huang *et al.*, Mon. Not. R. Astron. Soc. **502,** 6010 (2021).

[69] M. Martinelli *et al.*, Astron. Astrophys. **649,** A100 (2021).

[70] A. Schneider, R. Teyssier, J. Stadel, N. E. Chisari, A. M. C. Le Brun, A. Amara, and A. Refregier, J. Cosmol. Astropart. Phys. 03 (2019) 020.

[71] M. Yoon and M. J. Jee, Astrophys. J. **908,** 13 (2021).

[72] A. Amon *et al.*, Phys. Rev. D **105,** 023514 (2022).

[73] Dark Energy Survey Collaboration, arXiv:2105.13549 [Phys. Rev. D (to be published)].

[74] Dark Energy Survey Collaboration, Phys. Rev. D (to be published).

[75] I. Sevilla-Noarbe *et al.*, Astrophys. J. Suppl. Ser. **254,** 24 (2021).

[76] M. Jarvis *et al.*, Mon. Not. R. Astron. Soc. **501,** 1282 (2020).

[77] N. MacCrann *et al.*, Mon. Not. R. Astron. Soc. **509,** 3371 (2022).

[78] M. Gatti, E. Sheldon *et al.*, Mon. Not. R. Astron. Soc. **504,** 4312 (2021).

[79] J. Myles, A. Alarcon *et al.*, Mon. Not. R. Astron. Soc. **505,** 4249 (2021).

[80] M. Gatti, G. Giannini *et al.*, Mon. Not. R. Astron. Soc. (to be published).

[81] C. Sánchez, J. Prat *et al.*, Phys. Rev. D (to be published).

[82] J. P. Cordero, I. Harrison *et al.*, arXiv:2109.09636.

[83] W. G. Hartley, A. Choi *et al.*, Mon. Not. R. Astron. Soc. **509,** 3547 (2022).

[84] S. Everett *et al.*, Astrophys. J. Suppl. Ser. (to be published).

[85] O. Friedrich *et al.*, Mon. Not. R. Astron. Soc. (to be published).

[86] P. Lemos and M. Raveri *et al.*, Mon. Not. R. Astron. Soc. **505**, 6179 (2021).

[87] J. Muir *et al.*, Mon. Not. R. Astron. Soc. **494**, 4454 (2020).

[88] J. DeRose *et al.*, Mon. Not. R. Astron. Soc. (to be published).

[89] E. Krause *et al.*, Phys. Rev. D (to be published).

[90] B. Flaugher *et al.*, Astron. J. **150**, 150 (2015).

[91] G. M. Bernstein *et al.*, Publ. Astron. Soc. Pac. **130**, 054501 (2018).

[92] K. Eckert *et al.*, Mon. Not. R. Astron. Soc. **497**, 2529 (2020).

[93] E. Morganson *et al.*, Publ. Astron. Soc. Pac. **130**, 074501 (2018).

[94] E. Bertin and S. Arnouts, Astron. Astrophys. Suppl. Ser. **117**, 393 (1996).

[95] A. Drlica-Wagner *et al.*, Astrophys. J. Suppl. Ser. **235**, 33 (2018).

[96] E. Huff and R. Mandelbaum, arXiv:1702.02600.

[97] E. S. Sheldon and E. M. Huff, Astrophys. J. **841**, 24 (2017).

[98] C. Heymans *et al.*, Mon. Not. R. Astron. Soc. **427**, 146 (2012).

[99] C. Chang, M. Jarvis, B. Jain, S. M. Kahn, D. Kirkby, A. Connolly, S. Krughoff, E.-H. Peng, and J. R. Peterson, Mon. Not. R. Astron. Soc. **434**, 2121 (2013).

[100] P. Schneider, T. Eifler, and E. Krause, Astron. Astrophys. **520**, A116 (2010).

[101] P. Schneider and M. Lombardi, Astron. Astrophys. **397**, 809 (2003).

[102] G. M. Bernstein, R. Armstrong, C. Krawiec, and M. C. March, Mon. Not. R. Astron. Soc. **459**, 4467 (2016).

[103] M. Jarvis, G. Bernstein, and B. Jain, Mon. Not. R. Astron. Soc. **352**, 338 (2004).

[104] X. Fang, T. Eifler, and E. Krause, Mon. Not. R. Astron. Soc. **497**, 2699 (2020).

[105] E. Krause and T. Eifler, Mon. Not. R. Astron. Soc. **470**, 2100 (2017).

[106] Dark Energy Survey Collaboration, Phys. Rev. D **94**, 022001 (2016).

[107] H. Hildebrandt *et al.*, Astron. Astrophys. **633**, A69 (2020).

[108] J. Zuntz *et al.*, Mon. Not. R. Astron. Soc. **481**, 1149 (2018).

[109] J. Zuntz *et al.*, Astron. Comput. **12**, 45 (2015).

[110] W. J. Handley, M. P. Hobson, and A. N. Lasenby, Mon. Not. R. Astron. Soc. **453**, 4385 (2015).

[111] H. Jeffreys, Proc. Cambridge Philos. Soc. **31**, 203 (1935).

[112] D. N. Limber, Astrophys. J. **117**, 134 (1953).

[113] M. LoVerde and N. Afshordi, Phys. Rev. D **78**, 123506 (2008).

[114] R. G. Crittenden, P. Natarajan, U.-L. Pen, and T. Theuns, Astrophys. J. **568**, 20 (2002).

[115] P. Schneider, L. van Waerbeke, and Y. Mellier, Astron. Astrophys. **389**, 729 (2002).

[116] M. Tegmark and M. Zaldarriaga, Phys. Rev. D **66**, 103508 (2002).

[117] A. Lewis, A. Challinor, and A. Lasenby, Astrophys. J. **538**, 473 (2000).

[118] R. E. Smith, J. A. Peacock, A. Jenkins, S. D. M. White, C. S. Frenk, F. R. Pearce, P. A. Thomas, G. Efstathiou, and H. M. P. Couchman, Mon. Not. R. Astron. Soc. **341**, 1311 (2003).

[119] R. Takahashi, M. Sato, T. Nishimichi, A. Taruya, and M. Oguri, Astrophys. J. **761**, 152 (2012).

[120] A. Mead, J. A. Peacock, C. Heymans, S. Joudaki, and A. F. Heavens, Mon. Not. R. Astron. Soc. **454**, 1958 (2015).

[121] Euclid Collaboration, Mon. Not. R. Astron. Soc. **484**, 5509 (2019).

[122] E. Lawrence, K. Heitmann, J. Kwan, A. Upadhye, D. Bingham, S. Habib, D. Higdon, A. Pope, H. Finkel, and N. Frontiere, Astrophys. J. **847**, 50 (2017).

[123] P. Catelan, M. Kamionkowski, and R. D. Blandford, Mon. Not. R. Astron. Soc. **320**, L7 (2001).

[124] C. M. Hirata and U. Seljak, Phys. Rev. D **70**, 063526 (2004).

[125] J. Blazek, Z. Vlah, and U. Seljak, J. Cosmol. Astropart. Phys. 08 (2015) 015.

[126] P. Catelan and C. Porciani, Mon. Not. R. Astron. Soc. **323**, 713 (2001).

[127] D. M. Schmitz, C. M. Hirata, J. Blazek, and E. Krause, J. Cosmol. Astropart. Phys. 07 (**2018**) 030.

[128] T. M. Tugendhat and B. M. Schäfer, Mon. Not. R. Astron. Soc. **476**, 3460 (2018).

[129] Z. Vlah, N. E. Chisari, and F. Schmidt, J. Cosmol. Astropart. Phys. 01 (2020) 025.

[130] M. C. Fortuna, H. Hoekstra, B. Joachimi, H. Johnston, N. E. Chisari, C. Georgiou, and C. Mahony, Mon. Not. R. Astron. Soc. **501**, 2983 (2021).

[131] S. Bridle and L. King, New J. Phys. **9**, 444 (2007).

[132] C. M. Hirata, R. Mandelbaum, M. Ishak, U. Seljak, R. Nichol, K. A. Pimbblet, N. P. Ross, and D. Wake, Mon. Not. R. Astron. Soc. **381**, 1197 (2007).

[133] X. Fang, J. A. Blazek, J. E. McEwen, and C. M. Hirata, J. Cosmol. Astropart. Phys. 02 (**2017**) 030.

[134] J. E. McEwen, X. Fang, C. M. Hirata, and J. A. Blazek, J. Cosmol. Astropart. Phys. 09 (**2016**) 015.

[135] M. L. Brown, A. N. Taylor, N. C. Hambly, and S. Dye, Mon. Not. R. Astron. Soc. **333**, 501 (2002).

[136] S. Samuroff *et al.*, Mon. Not. R. Astron. Soc. **489**, 5453 (2019).

[137] D. Huterer, M. Takada, G. Bernstein, and B. Jain, Mon. Not. R. Astron. Soc. **366**, 101 (2006).

[138] A. Porredon *et al.*, Phys. Rev. D **103**, 043503 (2021).

[139] A. Porredon *et al.*, Phys. Rev. D (to be published).

[140] R. Cawthon *et al.*, Mon. Not. R. Astron. Soc. (to be published).

[141] S. Pandey *et al.*, Mon. Not. R. Astron. Soc. (to be published).

[142] E. Rozo *et al.*, Mon. Not. R. Astron. Soc. **461**, 1431 (2016).

[143] M. P. van Daalen, J. Schaye, I. G. McCarthy, C. M. Booth, and C. D. Vecchia, Mon. Not. R. Astron. Soc. **440**, 2997 (2014).

[144] J. Harnois-Déraps, L. van Waerbeke, M. Viola, and C. Heymans, Mon. Not. R. Astron. Soc. **450**, 1212 (2015).

[145] E. Semboloni, H. Hoekstra, and J. Schaye, Mon. Not. R. Astron. Soc. **434**, 148 (2013).

[146] E. Semboloni, H. Hoekstra, J. Schaye, M. P. van Daalen, and I. G. McCarthy, Mon. Not. R. Astron. Soc. **417**, 2020 (2011).

[147] M. P. van Daalen, J. Schaye, C. M. Booth, and C. D. Vecchia, Mon. Not. R. Astron. Soc. **415**, 3649 (2011).

[148] J. Schaye, C. D. Vecchia, C. M. Booth, R. P. C. Wiersma, T. Theuns, M. R. Haas, S. Bertone, A. R. Duffy, I. G. McCarthy, and F. van de Voort, Mon. Not. R. Astron. Soc. **402**, 1536 (2010).

[149] Y. Dubois et al., Mon. Not. R. Astron. Soc. **444**, 1453 (2014).

[150] N. Khandai, T. Di Matteo, R. Croft, S. Wilkins, Y. Feng, E. Tucker, C. DeGraf, and M.-S. Liu, Mon. Not. R. Astron. Soc. **450**, 1349 (2015).

[151] J. Schaye et al., Mon. Not. R. Astron. Soc. **446**, 521 (2015).

[152] M. Vogelsberger, S. Genel, V. Springel, P. Torrey, D. Sijacki, D. Xu, G. Snyder, D. Nelson, and L. Hernquist, Mon. Not. R. Astron. Soc. **444**, 1518 (2014).

[153] S. Samuroff, M. A. Troxel, S. L. Bridle, J. Zuntz, N. MacCrann, E. Krause, T. Eifler, and D. Kirk, Mon. Not. R. Astron. Soc. **465**, L20 (2017).

[154] Y. Dubois, S. Peirani, C. Pichon, J. Devriendt, R. Gavazzi, C. Welker, and M. Volonteri, Mon. Not. R. Astron. Soc. **463**, 3948 (2016).

[155] J. Schaye et al., Mon. Not. R. Astron. Soc. **446**, 521 (2015).

[156] S. Dodelson, C. Shapiro, and M. White, Phys. Rev. D **73**, 023009 (2006).

[157] F. Schmidt, E. Rozo, S. Dodelson, L. Hui, and E. Sheldon, Astrophys. J. **702**, 593 (2009).

[158] C. Shapiro, Astrophys. J. **696**, 775 (2009).

[159] J. Elvin-Poole, N. MacCrann et al., Mon. Not. R. Astron. Soc. (to be published).

[160] A. Lazanu, T. Giannantonio, M. Schmittfull, and E. P. S. Shellard, Phys. Rev. D **93**, 083517 (2016).

[161] R. Takahashi, T. Nishimichi, T. Namikawa, A. Taruya, I. Kayo, K. Osato, Y. Kobayashi, and M. Shirasaki, Astrophys. J. **895**, 113 (2020).

[162] J. Prat et al., Phys. Rev. D (to be published).

[163] S. M. Faber et al., Astrophys. J. **665**, 265 (2007).

[164] B. Joachimi, R. Mandelbaum, F. B. Abdalla, and S. L. Bridle, Astron. Astrophys. **527**, A26 (2011).

[165] J. DeRose et al., arXiv:1901.02401.

[166] P. Fosalba, M. Crocce, E. Gaztañaga, and F. J. Castander, Mon. Not. R. Astron. Soc. **448**, 2987 (2015).

[167] J. DeRose, M. R. Becker, and R. H. Wechsler, arXiv:2105.12104.

[168] R. H. Wechsler et al., arXiv:2105.12105.

[169] V. Springel, Mon. Not. R. Astron. Soc. **364**, 1105 (2005).

[170] M. R. Becker, Mon. Not. R. Astron. Soc. **435**, 115 (2013).

[171] J. Carretero, F. J. Castander, E. Gaztañaga, M. Crocce, and P. Fosalba, Mon. Not. R. Astron. Soc. **447**, 646 (2015).

[172] M. Crocce, F. J. Castander, E. Gaztañaga, P. Fosalba, and J. Carretero, Mon. Not. R. Astron. Soc. **453**, 1513 (2015).

[173] P. Fosalba, E. Gaztañaga, F. J. Castander, and M. Crocce, Mon. Not. R. Astron. Soc. **447**, 1319 (2015).

[174] K. Hoffmann, J. Bel, E. Gaztañaga, M. Crocce, P. Fosalba, and F. J. Castander, Mon. Not. R. Astron. Soc. **447**, 1724 (2015).

[175] K. Hoffmann et al. (to be published).

[176] T. Okumura, Y. P. Jing, and C. Li, Astrophys. J. **694**, 214 (2009).

[177] B. Joachimi, E. Semboloni, P. E. Bett, J. Hartlap, S. Hilbert, H. Hoekstra, P. Schneider, and T. Schrabback, Mon. Not. R. Astron. Soc. **431**, 477 (2013).

[178] B. Joachimi, E. Semboloni, S. Hilbert, P. E. Bett, J. Hartlap, H. Hoekstra, and P. Schneider, Mon. Not. R. Astron. Soc. **436**, 819 (2013).

[179] C. Laigle et al., Astrophys. J. Suppl. Ser. **224**, 24 (2016).

[180] C. Scarlata et al., Astrophys. J. Suppl. Ser. **172**, 406 (2007).

[181] S. Singh and R. Mandelbaum, Mon. Not. R. Astron. Soc. **457**, 2301 (2016).

[182] C. Seitz and P. Schneider, Astron. Astrophys. **318**, 687 (1997).

[183] Planck Collaboration, Astron. Astrophys. **641**, A5 (2020).

[184] C. Chang et al., Mon. Not. R. Astron. Soc. **482**, 3696 (2019).

[185] M. Raveri and W. Hu, Phys. Rev. D **99**, 043506 (2019).

[186] Dark Energy Survey Collaboration, Phys. Rev. D **98**, 043526 (2018).

[187] F. Capozzi, G. L. Fogli, E. Lisi, A. Marrone, D. Montanino, and A. Palazzo, Phys. Rev. D **89**, 093018 (2014).

[188] I. Esteban, M. C. Gonzalez-Garcia, A. Hernandez-Cabezudo, M. Maltoni, and T. Schwetz, J. High Energy Phys. 01 (2019) 106.

[189] Dark Energy Survey Collaboration, Phys. Rev. D **99**, 123505 (2019).

[190] R. Mandelbaum et al., Mon. Not. R. Astron. Soc. **481**, 3170 (2018).

[191] D. M. Scolnic et al., Astrophys. J. **859**, 101 (2018).

[192] Planck Collaboration, Astron. Astrophys. **641**, A8 (2020).

[193] W. Handley and P. Lemos, Phys. Rev. D **100**, 043504 (2019).

[194] W. Handley and P. Lemos, Phys. Rev. D **100**, 023512 (2019).

[195] S. Kullback and R. A. Leibler, Ann. Math. Stat. **22**, 79 (1951).

[196] W. Handley, J. Open Source Softw. **4**, 1414 (2019).

[197] M. Raveri, G. Zacharegkas, and W. Hu, Phys. Rev. D **101**, 103527 (2020).

[198] Astropy Collaboration, Astron. Astrophys. **558**, A33 (2013).

[199] Astropy Collaboration, Astron. J. **156**, 123 (2018).

[200] A. Lewis, arXiv:1910.13970.

[201] J. D. Hunter, Comput. Sci. Eng. **9**, 90 (2007).

[202] J. De Vicente, E. Sánchez, and I. Sevilla-Noarbe, Mon. Not. R. Astron. Soc. **459**, 3078 (2016).

[203] R. Mandelbaum, C. M. Hirata, M. Ishak, U. Seljak, and J. Brinkmann, Mon. Not. R. Astron. Soc. **367**, 611 (2006).

[204] S. Singh, R. Mandelbaum, and S. More, Mon. Not. R. Astron. Soc. **450**, 2195 (2015).

Correction: The omission of the 82nd author from the author list has been fixed.